EFFICIENT NUMERICAL METHODS FOR NONLINEAR SCHRÖDINGER EQUATIONS

by

Xiao Liang

A Dissertation Submitted in Partial Fulfillment

of the Requirements for the Degree of

Doctor of Philosophy in Computational Sciences

Middle Tennessee State University

December 2015

Dissertation Committee:

Dr. Abdul Khaliq, Chair

Dr. Yuri Melnikov

Dr. William Robertson

Dr. Dong Ye

To my beautiful wife, Shijun, who has been supporting me and encouraging me and made me believe that life is sweet.

ACKNOWLEDGMENTS

I want to express my deepest gratitude to my advisor, Dr. Abdul Q. M. Khaliq, without whose guidance and great support this dissertation would never have been possible. I would like to thank the co-authors of my research papers, Dr. Qin Sheng (Baylor University), Dr. Yulong Xing (Oak Ridge National Laboratory) and Dr. Khaled M. Furati (King Fahd University of Petroleum and Minerals), who gave me tremendous help with my research. I want to thank the director of the Computational Science Program, Dr. John Wallin and my committee members, Dr. Yuri Melnikov, Dr. William Robertson and Dr. Dong Ye, whose fruitful suggestions greatly improved the quality of this dissertation. I am grateful to the chair of Department of Mathematical Sciences, Dr. Don Nelson for facilitating teaching assignments during the academic years. I also want to thank my colleagues, Harish Bhatt, Viktor Reshniak and Zane Colgin, who shared with me valuable ideas for my research. Last but not least, I would like to express my sincere thanks to Middle Tennessee State University for providing the financial support during my Ph.D. study.

ABSTRACT

The nonlinear Schrödinger equations are widely used to model a number of important physical phenomena, including solitary wave propagations in optical fibers, deep water turbulence, laser beam transmissions, and the Bose-Einstein condensation, just to mention a few. In the field of optics and photonics, the systems of nonlinear Schrödinger equations can be used to model multi-component solitons and the interaction of self-focusing laser beams. In three spatial dimensions, the nonlinear Schrödinger equation is known as the Gross-Pitaevskii equation, which models the soliton in a low-cost graded-index fiber. Recently, research on nonlinear space fractional Schrödinger equations, which capture the self-similarity in the fractional environment, has become prevalent. Our study includes the systems of multi-dimensional nonlinear space fractional Schrödinger equations.

To solve the systems of multi-dimensional nonlinear Schrödinger equations efficiently, several novel numerical methods are presented. The central difference and quartic spline approximation based exponential time differencing Crank-Nicolson method is introduced for solving systems of one- and two-dimensional nonlinear Schrödinger equations. A local extrapolation is employed to achieve fourth-order accuracy in time. The numerical examples include the transmission of a self-focusing laser beam. The local discontinuous Galerkin methods combined with the fourth-order exponential time differencing Runge-Kutta time discretization are studied for solving the systems of nonlinear Schrödinger equations with hyperbolic terms, which are critical in modeling optical solitons in the birefringent fibers. The local discontinuous Galerkin method is able to achieve any order of accuracy in space, thanks to the usage of piecewise polynomial spaces. The exponential time differencing methods are employed to deal with the coupled nonlinearities for the reason that there is no need to solve nonlinear

systems at every time step, while the approach achieves expected accuracy.

The fourth-order exponential time differencing Runge-Kutta method is combined with the fourth-order compact scheme in space to solve the space fractional coupled nonlinear Schrödinger equations, involving Riesz derivatives. The system of four space fractional equations models the interaction of four water waves moving in the Lévy motion. A locally extrapolated exponential operator splitting scheme is applied to multi-dimensional nonlinear space fractional Schrödinger equations The scheme achieves second-order accuracy in time for both two-dimensional and three-dimensional problems, compared to the second-order ADI method, whose application is constrained to two-dimensional problems. The Gross-Pitaevskii equation containing space fractional derivatives is demonstrated to indicate the usage of the scheme.

Theoretical and numerical study of stability and convergence of the numerical methods have been discussed. Extensive numerical examples are provided to illustrate the accuracy, efficiency, and reliability of the proposed methods.

TABLE OF CONTENTS

LIST OF TABLES

LIST OF FIGURES

CHAPTER 1

INTRODUCTION

The nonlinear Schrödinger equation (NLSE) is an important model for the wave envelope in the dispersive, conservative, and mildly nonlinear physical environment [66]. In one spatial dimension, the NLSE is a key model describing the propagation of solitary waves in optical fibers [1]. In two spatial dimensions, the NLSE models the deep water turbulence. In the area of plasma physics, the two-dimensional NLSE is used to model the collapse of Langmuir waves [71] and self-focusing laser beams [56]. In three spatial dimensions, the NLSE is also known as the Gross-Pitaevskii equation, which can be used to model Bose-Einstein condensation [2, 5, 51]. Recently, the three-dimensional NLSE has been used in modeling spatial solitons, such as solitons in a graded-index multi-mode fiber [16]. The multi-dimensional NLSE system has a general form:

$$i\,u_{n\,t} + \beta_n\,\nabla u_n + \delta_n\,\Delta u_n + \left(\sum_{m=1}^{\mathcal{N}} f_{nm}(|u_m|^2)\right) u_n = 0, \tag{1}$$

where $i = \sqrt{-1},\ u_n \equiv u_n(r,\ t),\ n = 1, 2, ..., \mathcal{N},\ t \geq 0$, β_n and δ_n are real constants, f_{nm} are real functions, $r \in \Omega = \mathbb{R}^d$ and $d = 1, 2, 3$.

A number of studies have been done on numerical methods for the multi-dimensional NLSEs, including the alternating direction implicit method [72], the finite difference method [21, 34], the linearly implicit method [33], the exponential time differencing method [29], the discontinuous Galerkin method [3, 66], and the spectral method [17].

Exponential integrators have also been proposed by Berland et al. [8]. In the context of exponential integrators in general, the reader is referred to Hochbruck and Ostermann [27], and references therein. In Chapter 2, an exponential time differenc-

ing Crank-Nicolson (ETD-CN) strategy is employed to deal with coupled nonlinearities in the NLSEs. While our approach achieves expected accuracy and stability in computations, there is no need to solve nonlinear systems at every time step. This procedure ensures high efficiency.

In Chapter 3, we use the local discontinuous Galerkin (LDG) method as a spatial discretization to solve the NLSEs. The LDG method was introduced by Cockburn and Shu for solving the convection-diffusion equations [13]. It was derived from the Runge-Kutta discontinuous Galerkin (RKDG) method, which utilizes discontinuous basis functions [14]. The LDG method can be easily modified to achieve any order of accuracy in space, thanks to the usage of piecewise polynomial spaces [12, 15]. The LDG method degenerates the equations with high-order spatial derivatives into systems of equations with first-order spatial derivatives. Thus, for the LDG method, we only need to construct matrices for the first derivatives according to different numerical fluxes. The higher-order derivatives can be approximated by multiplications of the first-order matrices. Therefore, the LDG method is extremely convenient for an equation with both first-order and higher-order derivatives, such as a higher-order NLSE.

The fourth-order exponential time differencing Runge-Kutta (ETDRK4) temporal discretization we use in this research is based on the exponential time-differencing fourth-order Runge-Kutta (ETD4RK) method introduced by Cox and Matthews [11]. The ETD4RK method was modified by Khaliq et al. in [39]. Hederi et al. applied the ETDRK4 scheme to a single higher-order nonlinear Schrödinger (HONLS) equation [24]. As shown in their numerical results, the ETDRK4 is approximately four times faster than the fourth order split step Fourier method in simulating solutions of the HONLS equation. In [8, 27], the Krylov subspace methods and the Chebyshev

approximations of the matrix exponential operator are introduced. The ETDRK4 method uses the same idea as these methods.

1.1 One-dimensional NLSEs and optical solitons

In fiber optics, a soliton refers to an optical wave envelope that remains unchanged during propagation due to an exact balance of the linear and nonlinear effects [25]. There are two categories of solitons: *spatial* solitons and *temporal* solitons. For *spatial* solitons, the change of the electromagnetic field in the medium affects the refractive index, which makes the nonlinear effect and the diffraction effect balance each other. For *temporal* solitons, the nonlinear effect balances the dispersion effect in the medium [25].

The NLSEs can model both spatial and temporal solitons. One-dimensional NLSEs such as Eq. (2) are used to model temporal solitons:

$$iu_t + \epsilon u_{xx} + \beta|u|^2 u = 0. \tag{2}$$

In Eq. (2), u models the wave envelope. The linear term ϵu_{xx} represents the Group-velocity dispersion (GVD), which means the group velocity depends on the frequency. The nonlinear term $\beta|u|^2 u$ represents the Kerr effect, which means a change in the refractive index of the medium because of the change of the electric field. The GVD and Kerr effect balance each other under a proper combination as shown in the figure on the web page [65].

1.2 Two-dimensional NLSEs and self-focusing laser beams

It is shown in [56] that in a plasma channel, when the self-focusing effect overcomes the diffraction, a self-focusing laser beam will be generated. As indicated by Fig. 5 in [56], where z represents the normalized time, the beam self-focuses to reach a peak at $z = 87$. Then the beam defocuses at $z = 144$. At $z = 150$, the beam refocuses to reach another peak. This kind of self-focusing beam can be described by the NLSE [56]:

$$iu_z + \frac{1}{2k_0}\nabla_\perp^2 u + \frac{k_0\Delta(|u|^2)}{n_0}u = 0, \tag{3}$$

where u is the electric field envelope, k_0 is the wave number in the medium, n_0 represents the base index, $\Delta(|u|^2)$ is the change in nonlinear index. In Chapter 2, we will demonstrate the numerical result for a specific initial-boundary value problem generated by Eq. (3). In Chapter 3, we propose a system of two NLSEs to demonstrate the interaction of two co-propagating self-focusing laser beams.

1.3 NLSEs and vector solitons

As shown in [1], in a fiber communication system, the input pulse may be orthogonally polarized in a birefringent fiber. The polarized components can form solitary waves, which are named vector solitons. Because of the nonlinear coupling effect, the vector solitons can propagate undistorted even when the components have different widths and peak powers. The 2-coupled NLSE is in the following form:

$$\begin{aligned} i\,u_{1t} + \beta\,\nabla u_1 + \frac{1}{2}\Delta u_1 + \varepsilon\left(|u_1|^2 + \alpha|u_2|^2\right)u_1 = 0, \\ i\,u_{2t} + \beta\,\nabla u_2 + \frac{1}{2}\Delta u_2 + \varepsilon\left(\alpha|u_1|^2 + |u_2|^2\right)u_2 = 0, \end{aligned} \tag{4}$$

where u_1 and u_2 are amplitudes of waves through the orthogonal polarizations, $(X,t) \in \Omega_T = \Omega \times [0,t^n]$, $\Omega \subset \mathbb{R}^d$, $d = 1,2,3$. α is the coefficient of cross-phase modulation, $\varepsilon \geq 0$ is the nonlinear damping factor, which is a small real number. β is the linear coefficient and X represents the convection velocities in different directions.

Most articles do not consider the group velocity for polarization components, except for [35, 66]. In this research, we consider (4) with $\beta \neq 0$, since in high-birefringent fibers, the polarization components β representing the mismatch of group velocities between the fast and slow modes cannot be ignored [1]. Fig. 1.9 in [1] shows an example of vector soliton propagation. The slow mode and fast mode propagate together due to the nonlinear coupling effect.

1.4 NLSEs and solitons in a graded-index fiber

In fiber optics, the core size of a multi-mode fiber is larger than a single-mode fiber. A graded-index fiber is a multi-mode fiber with the property that its refractive index decreases while the core size increases. Solitons in graded-index fibres can improve data rates to ensure a low cost in telecommunications [53].

There are examples of optical solitons in a graded-index fiber in [53]. As described in Fig. 1 in [53], if there is only linear effects, the pulse will propagate inconsistently because of the diffraction. If the nonlinear effects balance the diffraction, the pulse will propagate in a pattern. This is how the soliton in a graded-index fiber delivers information in a telecommunication system. Solitons in a graded-index fiber can be modeled by a three-dimensional Gross-Pitaevskii equation [51]:

$$u_z = \frac{i}{2k_0}(u_{xx} + u_{yy}) - i\frac{\beta}{2}u_{tt} - i\frac{k_0\Delta}{R^2}(x^2+y^2)u + i\gamma|u|^2u, \tag{5}$$

where u models the slowly-varying wave envelope in a graded-index fiber, β represents

the material group-velocity dispersion, γ is the nonlinear coefficient, Δ is the difference of index between the center and the cladding of the fiber, R is the fiber core radius and k_0 is the wave number in the medium.

1.5 FNLSEs and fractional quantum mechanics

Recently, fractional partial differential equations have been considered and utilized to describe quantum phenomena in a fractal environment [26, 61]. For instance, in [19], sound wave propagations in rigid porous materials are modeled by fractional partial differential equations. The hereditary properties and memory of different materials are better described by the fractional-order derivatives [68]. It is shown in [49, 68] that space fractional derivatives are used to model anomalous diffusion or dispersion effects caused by the movement of particles, as opposed to the Brownian model, which describes the classical random motion of particles.

The nonlinear space fractional Schrödinger equations (FNLSEs), which include a space fractional derivative of order α ($1 < \alpha \leq 2$), are derived with the path integral over Lévy trajectories [43, 72]. Self-similarity of the quantum mechanical path, as an important physical property, can be captured by the space fractional derivatives [43]. When $\alpha = 2$, the Brownian motion takes the place of the Lévy motion, which leads to standard nonlinear Schrödinger equations.

The FNLSE in one dimension is used to model the evolution of an inviscid perfect fluid with nonlinear dynamics. It comes from the modification of water wave equations in two spatial dimensions. The fractional Laplacian represents the dispersion effect of the linearized gravity water waves equation for one dimensional surfaces [31]. The cubic nonlinear term in the FNLSE governs the nonlinear dynamics of water waves. The systems of FNLSEs can be used to describe the interaction of multiple water

waves. The FNLSEs have been shown to have smooth solutions in [23].

In Chapter 4, the one-dimensional space fractional coupled nonlinear Schrödinger equation (FCNLSE) containing the fractional Laplacian $(-\Delta)^{\alpha/2}$ $(1 < \alpha \leq 2)$ is considered:

$$\begin{aligned} i\,u_t - \gamma\,(-\Delta)^{\alpha/2}u + \rho(|u|^2 + \beta|v|^2)u = 0, \quad x \in \mathbb{R}, \quad 0 < t \leq T, \\ i\,v_t - \gamma\,(-\Delta)^{\alpha/2}v + \rho(|v|^2 + \beta|u|^2)v = 0, \quad x \in \mathbb{R}, \quad 0 < t \leq T. \end{aligned} \tag{6}$$

In a multi-dimensional space, the FNLSE can be used to model the optical solitons, whose propagation is governed by fractional quantum mechanics. The three-dimensional Gross-Pitaevskii equation introduced in Section 1.4 can be modified to a FNLSE for the case of fractional quantum mechanics.

In Chapter 5, we will consider the three-dimensional FNLSE with Riesz derivatives in the following form:

$$iu_t + \gamma(\frac{\partial^{\alpha_1}}{\partial|x|^{\alpha_1}} + \frac{\partial^{\alpha_2}}{\partial|y|^{\alpha_2}})u + \eta\frac{\partial^{\alpha_3}}{\partial|z|^{\alpha_3}}u + f(u) = 0, \quad (x, y, z) \in \mathbb{R}^3, \quad t \in (0,\ T], \tag{7}$$

where the spatial partial derivatives of the Gross-Pitaevskii equation have been changed to spatial fractional partial derivatives. Notice that when $\alpha_1 = \alpha_2 = \alpha_3 = 2$, Eq. (7) becomes the general Gross-Pitaevskii equation.

CHAPTER 2

ETD-CN WITH QUARTIC SPLINE APPROXIMATION AND FINITE DIFFERENCE METHODS

2.1 Introduction

In this chapter, we study a central difference and quartic spline approximation based exponential time differencing Crank-Nicolson (ETD-CN) method for solving systems of one- and two-dimensional NLSEs. A local extrapolation is employed to achieve fourth order accuracy in time. The stability properties of the spatial and temporal discretizations are proved and discussed. Numerical examples associated with Dirichlet, Neumann, and periodic boundary conditions are provided to illustrate the accuracy, efficiency and stability of the method proposed.

We consider the ETD-CN method together with central difference and quartic spline approximations for the numerical solution of following three sets of equations:

$$i\,\psi_t + \psi_{xx} + \lambda|\psi|^2\psi = 0, \tag{8}$$

and

$$\begin{aligned} i\,\psi_{1t} + \alpha\psi_{1xx} + \left(|\psi_1|^2 + \varrho|\psi_2|^2\right)\psi_1 = 0,\\ i\,\psi_{2t} + \alpha\psi_{2xx} + \left(\varrho|\psi_1|^2 + |\psi_2|^2\right)\psi_2 = 0. \end{aligned} \tag{9}$$

and

$$i\,\psi_t + \psi_{xx} + \psi_{yy} + |\psi|^2\psi = 0. \tag{10}$$

The numerical results by the ETD-CN method are compared with the results by a linearly implicit method and the energy conservative Crank-Nicolson method,

which illustrates the efficiency and accuracy of the ETD-CN method. To solve the two-dimensional problem (10), we utilize a combination of the ETD-CN method and an alternating direction implicit (ADI) method.

2.2 The ETD-CN method

Consider the following nonlinear initial-boundary value problem:

$$\begin{aligned} u_t + Au &= F(u,t), \quad (x,t) \in \Omega \times (0,\infty); \\ u(x,t) &= u_b, \quad (x,t) \in \partial\Omega \times (0,\infty), \\ u(x,0) &= u^0, \quad x \in \Omega, \end{aligned} \tag{11}$$

where $\Omega \subset \mathbb{R}$ is bounded by $\partial\Omega$, A is a linear operator in a Banach space, and the function F is bounded. See also [70]. Let $\tau = t^{n+1} - t^n$ be the temporal step size to be used on the mesh $\{t^n\}$ such that the approximate solution $u(t^n)$ is denoted by u^n. Then the formal solution [38, 58] of (11) is

$$u(t^{n+1}) = e^{-\tau A}u(t^n) + e^{-\tau A}\int_0^\tau e^{sA}F(u(t^n+s), t^n+s)ds. \tag{12}$$

While (12) serves as a foundation for the general ETD-CN method [38, 70], a different class of ETD schemes for problems with the mildly nonlinear operator A has also been studied [37, 67]. Herewith we employ a second order [1/1] Padé approximant $R_{1,1}$ to the matrix exponential in (12). This yields a standard ETD-CN scheme [38]:

$$\begin{aligned} u^{n+1} &= b^n + \tau(2I + \tau A)^{-1}[F(b^n, t^{n+1}) - F(u^n, t^n)], \\ b^n &= R_{1,1}(\tau A)u^n + 2\tau(2I + \tau A)^{-1}F(u^n, t^n), \end{aligned} \tag{13}$$

in which

$$R_{1,1}(\tau A) = 4(2I + \tau A)^{-1} - I,$$

where I is the identity operator.

Scheme (13) can be realized in two steps:

1. To acquire b^n, we solve

$$(2I + \tau A)N_b = 4u^n + 2\tau F(u^n, t^n)$$

for N_b first and then set

$$b^n = N_b - u^n.$$

2. We solve

$$(2I + \tau A)N_u = \tau[F(b^n, t^{n+1}) - F(u^n, t^n)]$$

for N_u and subsequently,

$$u^{n+1} = b^n + N_u.$$

Kleefield et al. [38] proved the above-mentioned ETD-CN method converges quadratically. We are able to confirm computationally that its convergence is second order in time.

2.3 The ETD-CN method with central difference approximation

Let re and im represent the real and imaginary parts of a complex number z, respectively. Therefore, we may express z in the form of a real vector, that is,

$$z \Rightarrow \begin{bmatrix} re \\ im \end{bmatrix}$$

and consequently,

$$i \cdot z \Rightarrow \begin{bmatrix} 0 & -1 \\ 1 & 0 \end{bmatrix} z.$$

Now, to solve (8) numerically, we let $0 < h \ll 1$ be a uniform spatial step size, n be the total number of mesh points in space, u be the vector $(u_1, u_2, \ldots, u_j, \ldots u_n)^\top$, where u_j's are approximations of ψ at mesh points along x and $\tilde{u}_j$ be the vector form of $\{u_j\}_1^n$, that is, $\omega_j = \begin{bmatrix} v_j \\ w_j \end{bmatrix}$, in which v_j and w_j are real and imaginary parts of an approximation of that of u_j, respectively. Then (8) under homogenuous Dirichlet boundary conditions can be solved readily through the following semi-discretized system,

$$\omega_t + A_1\omega = i\, f(|\omega|^2)\omega, \tag{14}$$

where $A_1 \in \mathbb{R}^{2n\times 2n}$,

$$A_1 = -\frac{1}{h^2}\begin{bmatrix} -2P & P & 0 & 0 & \cdots \\ P & -2P & P & 0 & \cdots \\ 0 & P & -2P & P & \cdots \\ & \ddots & \ddots & \ddots & \ddots \\ \cdots & 0 & 0 & P & -2P \end{bmatrix}, \quad P = \begin{bmatrix} 0 & -1 \\ 1 & 0 \end{bmatrix}, \tag{15}$$

and

$$\omega = \left(\omega_1^\top, \omega_2^\top, \ldots, \omega_j^\top, \ldots \omega_n^\top\right)^\top,$$

based on a second order central finite difference approximation.

2.4 ETD-CN method with quartic spline approximation

For any sufficiently smooth function $r(x_j) = r_j$, we define

$$\delta_x^2 r_j = r_{j-1} - 2r_j + r_{j+1}, \quad j = 1, 2, \ldots, n. \tag{16}$$

Let $\tilde{u}(\xi_j, t)$ be a vector solution of (8) which is sufficiently smooth, and $s(x, t)$ be its quartic spline approximation. Then, according to the Numerov condition [57], we

have the following collocation relation,

$$m_{j-1} + 10m_j + m_{j+1} = \frac{12}{h^2}\delta_x^2\omega_j + e_j, \quad j = 1, 2, \ldots, n,$$

where $\omega_j = \omega(x_j, t)$ are at least fourth order approximations of $\tilde{u}(x_j, t)$, $m_j = s_{xx}(x_j, t)$, $x_j \in \Omega$, and e_j are local truncation errors given by

$$e_j = -\frac{h^4}{240}\,\tilde{u}_{x^6}(\xi_j, t),$$

and ξ_j reside in neighborhoods of x_j, $j = 1, 2, \ldots, n$, respectively. Consequently, equation (8) together with homogeneous boundary conditions can be approximated by

$$\left(I_{2n} + \frac{1}{12}A_q\right)\omega_t + A_1\omega = i\left(I_{2n} + \frac{1}{12}A_q\right) f(|\omega|^2)\omega, \tag{17}$$

where $I_{2n} \in \mathbb{R}^{2n\times 2n}$ is the identity matrix and $A_q \in \mathbb{R}^{2n\times 2n}$, that is,

$$A_q = \begin{bmatrix} -2I_2 & I_2 & 0 & 0 & \cdots \\ I_2 & -2I_2 & I_2 & 0 & \cdots \\ 0 & I_2 & -2I_2 & I_2 & \cdots \\ & \ddots & \ddots & \ddots & \ddots \\ \cdots & 0 & 0 & I_2 & -2I_2 \end{bmatrix}, \; I_2 = \begin{bmatrix} 1 & 0 \\ 0 & 1 \end{bmatrix}. \tag{18}$$

The equation (17) leads to

$$\omega_t + \left(I_{2n} + \frac{1}{12}A_q\right)^{-1} A_1\omega = i\, f(|\omega|^2)\omega.$$

Denote $A_2 = (I_{2n} + (1/12)A_q)^{-1}A_1$. We acquire the desired ETD-CN method to use:

$$\omega_t + A_2\omega = i\, f(|\omega|^2)\omega. \tag{19}$$

2.5 Mass conservation

Since the mass of a numerical solution can be evaluated via the spectral norm $\|u\|_2$, for given $0 \le \epsilon \ll 1$, its mass conservation can be defined by the following inequality

[57],

$$\left| \|u\|_2^2 - \ c \right| \leq \epsilon \, |t - t_0|,$$

where $c > 0$ is a constant oriented from the mass of the analytic solution.

For any $u, v \in \mathbb{R}^{2n}$, we consider the inner product

$$\langle u, v \rangle = u^\top v = \sum_{j=1}^{2n} u_j v_j.$$

Therefore,

$$\|u\|_2 = \sqrt{h \, \langle u, u \rangle} = \sqrt{h \sum_{j=1}^{2n} u_j^2}\,.$$

Let ω be an approximation of u. Since A_1 is skew symmetric, we have [57]

$$\frac{1}{2}\frac{d}{dt}\|u\|_2^2 \approx h \left\langle \frac{d\omega}{dt}, \omega \right\rangle = 0.$$

This implies that the solution of the NLSE may conserve approximately. Numerical examples agree with these predictions.

2.6 Stability analysis

We now show that the ETD-CN schemes are unconditionally linearly stable. First we present two lemmas and use $\otimes$ for the Kronecker product of matrices [9, pp.137-141].

Lemma 2.1 *Let*

$$E = \text{tridiag}(1, -2, 1) \in \mathbb{R}^{n \times n}.$$

Then its eigenvalues are

$$\mu_j = -4 \sin^2 \frac{j\pi}{2(n+1)}, \quad j = 1, 2, \ldots, n.$$

Consequently, eigenvalues of the TST matrices $T^{\pm} = I_n \pm rE$, *where* $I_n \in \mathbb{R}^{n\times n}$ *is the identity matrix, are*

$$\lambda_j^{\pm} = 1 \mp 4r \sin^2 \frac{j\pi}{2(n+1)}, \quad j = 1, 2, \ldots, n,$$

and

$$\left\|T^{\pm}\right\|_2 = \max_{1\le j\le n} |\lambda_j| .$$

Its proof is in [20, 59].

Lemma 2.2 *Let* $\lambda_i,\ 1 \le i \le n$, *and* $\mu_j,\ 1 \le j \le m$, *be eigenvalues of* $A \in \mathbb{R}^{n\times n},\ B \in \mathbb{R}^{m\times m}$, *respectively. Then the eigenvalues of* $A \otimes B$ *are*

$$\lambda_1\mu_1, \ldots, \lambda_1\mu_m, \lambda_2\mu_1, \ldots, \lambda_2\mu_m, \ldots, \lambda_n\mu_1, \ldots, \lambda_n\mu_m.$$

Its proof is in [42].

Theorem 2.3 The ETD-CN schemes (14) and (17) are unconditionally linearly stable.

Proof 2.4 *The linear stability of (14) and (17) depends on properties of*

$$M = 2I_{2n} + kA_1, \quad N = 2I_{2n} + kA_2,$$

respectively, where

$$A_1 = -\frac{1}{h^2}E \otimes P, \quad A_2 = -\frac{1}{h^2}\left(I_{2n} + \frac{1}{12}E \otimes I_2\right)^{-1}(E \otimes P),$$

and $P,\ I_2$ *are given in (15) and (18), respectively.*

We need to show that $\|M^{-1}\|_2,\ \|N^{-1}\|_2 < 1$. *To this end, we observe that* $A_1^\top = -A_1,\ A_2^\top = -A_2$ *since* $P^\top = -P$. *Recalling the symmetry of* E *and* I_2, *it follows that*

$$\begin{aligned} MM^\top &= (2I_{2n} + kA_1)\,(2I_{2n} - kA_1) = 4I_{2n} - k^2A_1^2 \\ &= 4I_{2n} - \frac{k^2}{h^4}(E \otimes P)(E \otimes P) = 4I_{2n} - \frac{k^2}{h^4}E^2 \otimes P^2. \end{aligned}$$

Thus, utilizing Lemmas 2.1 and 2.2, eigenvalues of $MM^\top$ *are*

$$\begin{aligned} eigen\left(MM^\top\right)_j &= 4 - \frac{k^2}{h^4}\ eigen\left(E^2 \otimes P^2\right)_j \\ &= 4 + \frac{16k^2}{h^4}\sin^4\frac{j\pi}{2(2n+1)} > 1, \quad j = 1, 2, \ldots, 2n, \end{aligned}$$

due to the fact that $eigen\,(P^2)_j = -1,\ j = 1, 2$. *The above inequalities imply that*

$$\|M\|_2 > 1.$$

Hence,

$$\left\|M^{-1}\right\|_2 < 1.$$

This ensures the stability of (14).

On the other hand,

$$NN^\top = 4I_{2n} - k^2A_2^2.$$

Let λ *be an eigenvalue and* x *be an eigenvector of* $NN^\top$. *We have*

$$\left(4I_{2n} - k^2A_2^2\right)x = \lambda\, x.$$

The above can be reformulated to

$$A_2^2 x = \mu^2 x,$$

where

$$\mu^2 = \frac{4 - \lambda}{k^2}. \tag{20}$$

Thus, $A_2 x = \mu x$ *and this leads to*

$$\left(I_{2n} + \frac{1}{12} E \otimes I_2\right)^{-1} (E \otimes P)x = \left[(E \otimes P)^{-1}\left(I_{2n} + \frac{1}{12} E \otimes I_2\right)\right]^{-1} x = h^2 \mu x.$$

Since $I_{2n} + \frac{1}{12} E \otimes I_2$ *and* $E \otimes P$ *are both nonsingular,* A_2 *is nonsingular and subsequently,* $\mu \neq 0$. *According to Lemmas 2.1 and 2.2, we have*

$$\begin{aligned}
(E \otimes P)^{-1}\left(I_{2n} + \frac{1}{12} E \otimes I_2\right) x &= (E^{-1} \otimes P^{-1})\left(I_{2n} + \frac{1}{12} E \otimes I_2\right) x \\
&= \left[E^{-1} \otimes P^{-1} + \frac{1}{12}\left(E^{-1} \otimes P^{-1}\right)(E \otimes I_2)\right] x \\
&= \left(E^{-1} \otimes P^{-1} + \frac{1}{12} I_n \otimes P^{-1}\right) x \\
&= \left(E^{-1} + \frac{1}{12} I_n\right) \otimes P^{-1} x = \frac{1}{h^2 \mu} x.
\end{aligned}$$

Recall that $P^{-1} = P^{\top}$. *We acquire immediately that*

$$\frac{1}{h^2 \mu} = \pm\, i\, eigen\left(E^{-1} + \frac{1}{12} I_n\right) = \pm\, i \left(-\frac{1}{4\sin^2(j\pi/(2n+2))} + \frac{1}{12}\right),$$

for $j = 1, 2, \ldots, n$. *It follows immediately that*

$$\mu^2 = -\frac{1}{h^4}\left(\frac{1}{12} - \frac{1}{4\sin^2(j\pi/(2n+2))}\right)^{-2} = -\frac{\sigma^2}{h^4}, \quad j = 1, 2, \ldots, n.$$

Thus,

$$\sigma_j^2,\ \sigma_{n+j}^2 = 2\left(\frac{1}{3} - \frac{1}{\sin^2(j\pi/(2n+2))}\right)^{-2} > 0, \quad j = 1, 2, \ldots, n.$$

Now, recall (20). We find that

$$4 - \lambda_j = -\frac{k^2}{h^4}\sigma_j^2 < 0, \quad j = 1, 2, \ldots, 2n,$$

and they imply that $\max_{1 \leq j \leq 2n} \lambda_j > 4 > 1$ *which leads to*

$$\left\|N^{-1}\right\|_2 < \frac{1}{4} < 1.$$

The proof is thus completed.

2.7 Stability regions

In the previous discussion, we studied the linear stability of the ETD-CN method. Now, let us consider stability regions of the numerical method when applied to a nonlinear equation similar to that in [11]. Given an ordinary differential equation,

$$u_t = cu + F(u), \tag{21}$$

where $F(u)$ is a nonlinear function. Assume that a fixed point u_0 exists, such that $cu_0 + F(u_0) = 0$. Suppose u is a perturbation of u_0 and $\lambda = F'(u_0)$, then Eq. (21) can be linearized as

$$u_t = cu + \lambda u. \tag{22}$$

If $\mathrm{Re}(c+\lambda) < 0$, we can tell that the fixed point u_0 is stable. Let $x = \lambda\tau$ and $y = c\tau$ and apply the ETD-CN method (14) or (17) for solving (22). Then we can compute the amplification factor $r(x, y)$ as

$$\frac{u^{n+1}}{u^n} = r(x,\ y) = \frac{2 + y + 2x}{2 - y} + \frac{2x^2 + 2yx}{(2-y)^2}. \tag{23}$$

To obtain stability regions, we assume that $r(x,\ y) < 1$. When x and y are both real, the stability region of the ETD-CN method is shown in Fig. 1. If x is complex, we fix y to some non-positive values, and the stability regions are demonstrated in Fig. 2. It can be observed that as $|c\tau|$ increases, the stability region expands.

2.8 Extrapolation of the ETD-CN method

Following the local extrapolation procedure by Lawson and Morris [44], let us consider (13) over a temporal span of 2τ, that is,

$$\begin{aligned} u^{n+2} &= b^n + 2k(2I + 2\tau A)^{-1}[F(b^n, t^{n+2}) - F(u^n, t^n)], \\ b^n &= R_{1,1}(2\tau A)u^n + 2\tau(2I + 2\tau A)^{-1}F(u^n, t^n), \end{aligned} \tag{24}$$

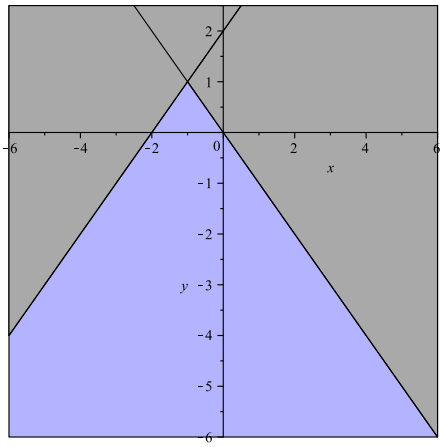

Figure 1: The stability region (light colored) of an ETD-CN method when x and y are real.

where

$$R_{1,1}(2\tau A) = 4(2I + 2\tau A)^{-1} - I.$$

Alternately, when (13) is applied twice, we have

$$\begin{aligned} u^{n+2} = \;& b^{n+1} + \tau(2I + \tau A)^{-1}[F(b^{n+1}, t^{n+2}) - F(u^{n+1}, t^{n+1})], \\ b^{n+1} = \;& R_{1,1}(\tau A)u^{n+1} + 2\tau(2I + \tau A)^{-1}F(u^{n+1}, t^{n+1}), \\ u^{n+1} = \;& b^{n} + \tau(2I + \tau A)^{-1}[F(b^{n}, t^{n+1}) - F(u^{n}, t^{n})], \\ b^{n} = \;& R_{1,1}(\tau A)u^{n} + 2\tau(2I + \tau A)^{-1}F(u^{n}, t^{n}), \end{aligned} \tag{25}$$

in which

$$R_{1,1}(\tau A) = 4(2I + \tau A)^{-1} - I.$$

Let us denote the solution procedures in (24) and (25) by $u_{(1)}^{n+2}$ and $u_{(2)}^{n+2}$, respectively. However,

$$u_{(E)}^{n+2} = \frac{4}{3}u_{(2)}^{n+2} - \frac{1}{3}u_{(1)}^{n+2} \tag{26}$$

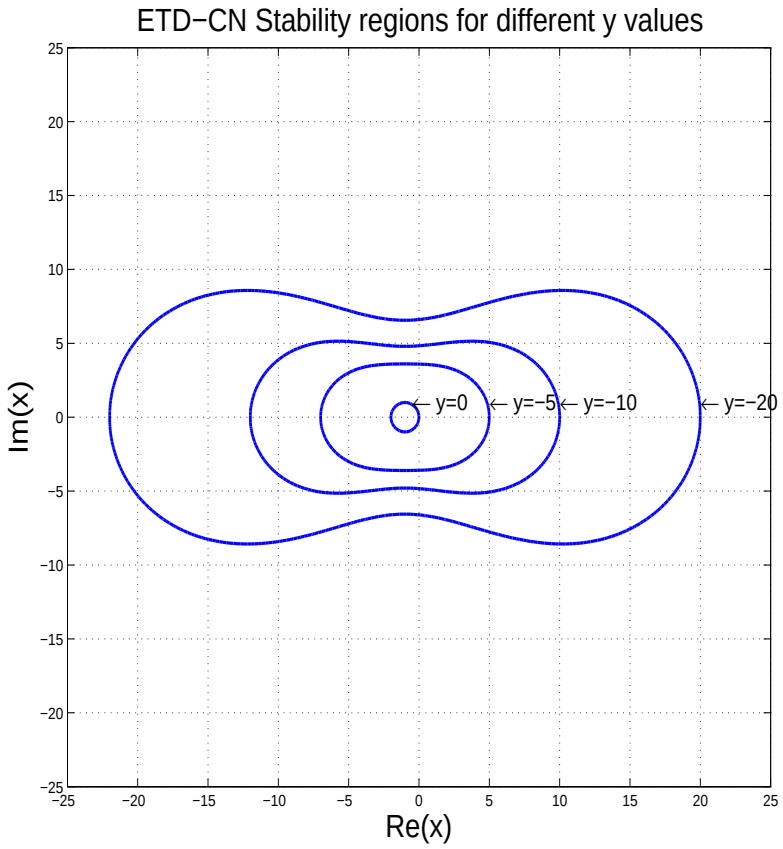

Figure 2: Stability regions of the ETD-CN method with y fixed to some non-positive values.

is a fourth order approximation to the true solution at t^{n+2} with a principal coefficient being the truncation error $E_5 = 1/10$. See also [32, 47] for the use of Richardson extrapolation to gain the same order of accuracy.

2.9 Numerical experiments

In the following numerical experiments, h represents the spatial step size and τ represents the time step size. An error vector, ER, is measured by using the ℓ_∞ and ℓ_2 norms defined by

$$\|ER\|_\infty = \max_{1<m<N} \left\{ \left| \|\psi(x_m, t_n)\| - \|\tilde{u}^n_{1,m} + i\tilde{u}^n_{2,m}\| \right| \right\},$$

and

$$\|ER\|_2 = \left[\sum_{m=1}^{N} \left| \|\psi(x_m, t_n)\| - \|\tilde{u}^n_{1,m} + i\tilde{u}^n_{2,m}\| \right|^2 \right]^{1/2},$$

where N is the dimension of $\tilde{u}$.

2.10 Systems of two NLSEs

We consider the following system [33, 69]:

$$\begin{aligned} i\,\psi_{1t} + \alpha\psi_{1xx} + \left(|\psi_1|^2 + \varrho|\psi_2|^2\right)\psi_1 = 0, \\ i\,\psi_{2t} + \alpha\psi_{2xx} + \left(\varrho|\psi_1|^2 + |\psi_2|^2\right)\psi_2 = 0. \end{aligned} \tag{27}$$

We consider two key cases. In Case One, the following initial and boundary conditions are utilized.

$$\begin{aligned} \psi_1(x,0) &= \sqrt{\frac{2\alpha}{1+\varrho}}\,\mathrm{sech}(\sqrt{\alpha}x)\exp(i\,\upsilon x), \\ \psi_2(x,0) &= \sqrt{\frac{2\alpha}{1+\varrho}}\,\mathrm{sech}(\sqrt{\alpha}x)\exp(i\,\upsilon x), \\ \psi_1(x,t)_x &= \psi_2(x,t)_x = 0 \quad \text{at} \quad x = -20,\ 60, \end{aligned} \tag{28}$$

where $\varrho = 1,\ \upsilon = 1$ and $\alpha = 1$. Corresponding analytic solutions of (27) are given in [33]:

$$\psi_{Aj}(x,t) = \sqrt{\frac{2\alpha}{1+\varrho}}\,\mathrm{sech}\left(\sqrt{\alpha}(x-\upsilon t)\right)\exp\left(i(\upsilon x - (\upsilon^2 - \alpha)t)\right), \quad j = 1, 2. \tag{29}$$

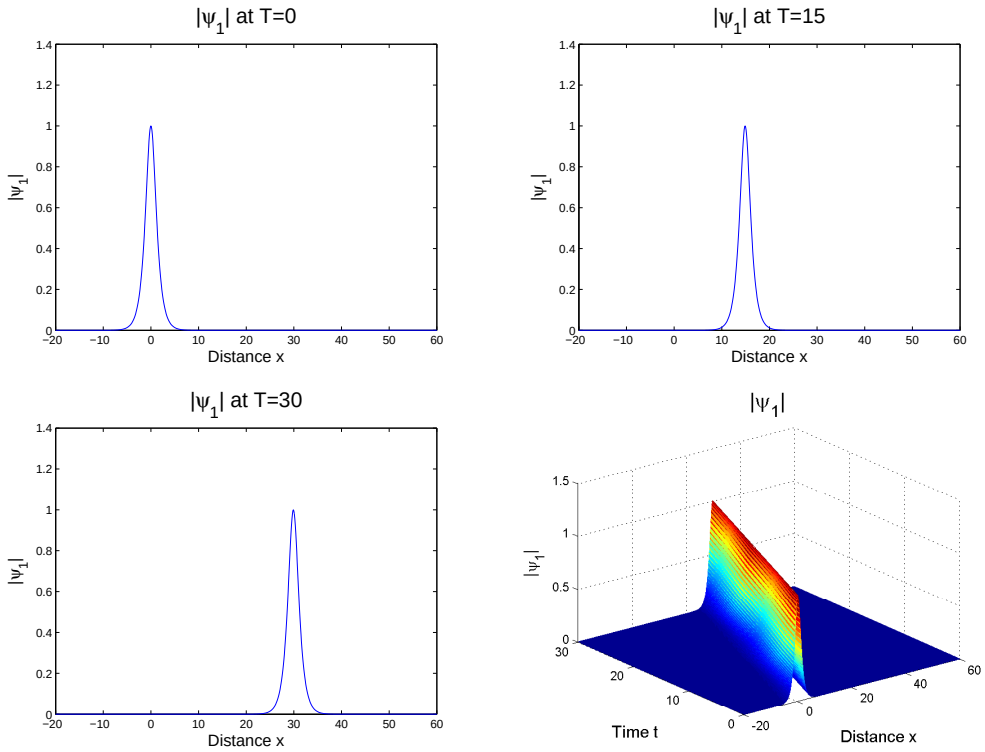

Figure 3: Numerical simulation of system (27) with initial conditions (28).

The soliton solution of (27) together with (28) obtained via the ETD-CN method with quartic spline approximation ($h = 0.1$, $\tau = 0.01$ and $T = [0,\ 30]$) is shown in Fig. 3. The modulus $|\psi_2|$ is identical to $|\psi_1|$ for the same initial values. We observe that the phase of the soliton moves to the right at a constant speed of one. The solitons indicate that, when the amplitudes of the underlying pulses are equal, the waves should propagate with the same shape. Their phase traveling directions and speeds are identical, respectively.

Eq. (27) is often called the integrable Manakov equation. It models solitons in a birefringent optical fiber possessing a refractive index depending on the polarization and propagation direction of pulses [69]. Two solitons can be formed by a decomposition of each light ray. Initial condition (28) models two solitons traveling together in the same direction.

Table 1: A comparison of L_∞ errors of solutions to system (27)-(28) ($h = 0.1$, $\tau = 0.01$ and $T = [0, 30]$).

t	linearly implicit [33]	Crank-Nicolson [33]	ETD-CN Central Difference	ETD-CN Quartic Spline
5	0.047690	0.01972	0.00595	5.60342e-5
10	0.089070	0.03777	0.01125	9.08083e-5
15	0.126621	0.05582	0.01663	2.17458e-4
20	0.188602	0.07379	0.02204	4.49535e-4
25	0.182201	0.09149	0.02768	7.73105e-4
30	0.276529	0.109349	0.03320	0.0011933

In Table 1, we compare the accuracy of the ETD-CN method with central difference approximation and the ETD-CN method with quartic spline approximation to the accuracy of linearly implicit and Crank-Nicolson methods [33]. The linearly implicit method loses it's theoretical order of convergence when the nonlinear term is treated explicitly, while the ETD-CN method with central difference approximation maintains it's theoretical order of convergence with much less errors as shown

in Table 1. The same $h,\ \tau$ and other parameters are used in all four cases. The ETD-CN method is more accurate and efficient as compared with Crank-Nicolson method because the nonlinear equations do not need to be solved at each time step. When ETD-CN with quartic spline approximation is used, the method reaches a high accuracy in space. This is due to the fact that the system of two NLSE generates errors in both amplitude and horizontal position due to the horizontal movement of the wave. The precision of the ETD-CN method with a quartic spline approximation makes it better suited in this situation. During the computation, we only employ the LU decomposition once and matrix multiplications for several times within the loop of updating values of $\psi(\cdot, t+1)$. These results demonstrate the satisfactory efficiency of our newly constructed ETD-CN method.

Table 2 is devoted to comparisons of the numerical results by the extrapolated ETD-CN method with quartic spline approximation, and of the results given in [32] via Richardson extrapolations. The same parameters given by [32] are used: $\alpha = 0.5,\ \varrho = 2/3,\ \upsilon = 1,\ h = 0.2,\ \tau = 0.05$.

Table 2: The ℓ_∞ error comparison of the extrapolated ETD-CN method with quartic spline approximation, and of the Richardson extrapolation.

t	Ismail and Alamri [32]	Extrapolated ETD-CN
4	0.001321	0.001126
8	0.002408	0.002168
12	0.003750	0.003545
16	0.005429	0.005112
20	0.007226	0.006955

In Case Two, we consider the birefringent situation as given in [69]. We replace

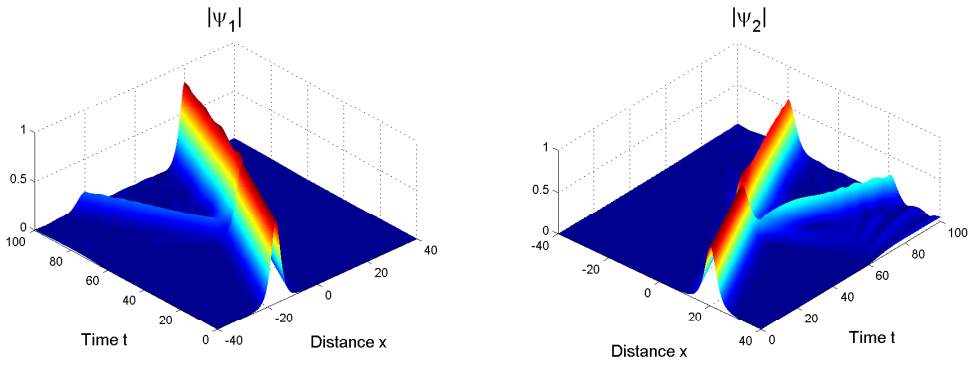

Figure 4: The propagation of solitons (27) based on (30).

the initial and boundary conditions for (27) by the following:

$$\begin{aligned} \psi_1(x,0) &= \sqrt{2}\,\alpha_1\,\mathrm{sech}(\alpha_1 x + x_0)\exp(i\,\upsilon_1 x), \\ \psi_2(x,0) &= \sqrt{2}\,\alpha_2\,\mathrm{sech}(\alpha_2 x - x_0)\exp(i\,\upsilon_2 x), \\ \psi_1(x,t)_x &= \psi_2(x,t)_x = 0, \quad \text{at} \quad x = \pm 40, \end{aligned} \tag{30}$$

where $\varrho = 2/3,\ \upsilon_1 = 0.2,\ \upsilon_2 = -0.2,\ \alpha_1 = 0.6,\ \alpha_2 = 0.5$ and $x_0 = 20$.

Table 3: Mass conservations of (27), (30) by using the ETD-CN method with a quartic spline approximation.

t	$\|\psi_1\|_2^2$	Error in mass	$\|\psi_2\|_2^2$	Error in mass
0	1.549193	0	1.414214	0
20	1.549263	0.000070	1.414228	0.000014
40	1.549331	0.000138	1.414245	0.000031
60	1.549392	0.000199	1.414247	0.000033
80	1.549475	0.000282	1.414316	0.000102
100	1.549538	0.000345	1.414317	0.000103

This initial-boundary value problem generates two optical waves propagating and interacting in a birefringent fiber. We may observe in Fig. 4 obtained via the ETD-CN method based on a quartic spline approximation ($h = 0.1,\ \tau = 0.05,\ T = [0, 100]$)

that in the situation with (30), the two solitons ψ_1 and ψ_2 start their propagation at $x = -20$ and $x = 20$ respectively. After the solitons interact at $t \approx 40$, their phase travel directions are slightly altered and there appears to be a daughter wave for each of them. The amplitude of such a daughter wave of $|\psi_2|$ is larger since the amplitude of $|\psi_1|$ is larger, because the effect of $|\psi_1|$ on $|\psi_2|$ in the interaction is larger. Table 3 gives mass profiles of the two solitons as t increases. It is found that after the collision, mass errors of the numerical solutions grow only mildly; therefore, the daughter waves are not consequences of numerical errors.

2.10.1 Two-dimensional NLSEs

In this section, we first consider the following two-dimensional NLSE:

$$\begin{aligned} i\,\psi_t + \psi_{xx} + \psi_{yy} &= |\psi|^2\psi, \quad (x,y,t) \in \Omega \times \Omega \times (0,\infty), \\ \psi &= \psi_b, \quad (x,y,t) \in \partial\Omega \times \partial\Omega \times (0,\infty), \\ \psi(x,0) &= \psi_0, \quad x,y \in \Omega, \end{aligned} \tag{31}$$

where $\Omega \subset \mathbb{R}$ is bounded,

We consider the ETD-CN algorithm (13) and *alternating direction implicit* (ADI) method [59] to solve problem (31). This indicates a split of the differential equation (31) to two sub-equations. One with the x-derivative and the other with the y-derivative.

First, we solve the following equation in the x-direction

$$\nu_t + A_1\nu = \frac{1}{2}i|\nu|^2\nu, \tag{32}$$

where matrix A_1 is the same as in (15) and ν is a $2N \times N$ matrix approximating ψ,

that is,

$$\nu = \begin{bmatrix} \nu_{11} & \nu_{12} & \nu_{13} & \cdots & \nu_{1N} \\ \nu_{21} & \nu_{22} & \nu_{23} & \cdots & \nu_{2N} \\ \nu_{31} & \nu_{32} & \nu_{33} & \cdots & \nu_{3N} \\ \vdots & \vdots & \vdots & \ddots & \vdots \\ \nu_{N1} & \nu_{N2} & \nu_{N3} & \cdots & \nu_{NN} \end{bmatrix}$$

in which

$$\nu_{ij} = \begin{bmatrix} v_{ij} \\ w_{ij} \end{bmatrix},$$

where v_{ij} and w_{ij} are the real and imaginary parts of ν_{ij} and $|\nu_{ij}|^2 = v_{ij}^2 + w_{ij}^2$. Let us denote $a_{ij} = |\nu_{ij}|^2$, then

$$|\nu|^2\nu = \begin{bmatrix} a_{11}\nu_{11} & a_{12}\nu_{12} & a_{13}\nu_{13} & \cdots & a_{1N}\nu_{1N} \\ a_{21}\nu_{21} & a_{22}\nu_{22} & a_{23}\nu_{23} & \cdots & a_{2N}\nu_{2N} \\ a_{31}\nu_{31} & a_{32}\nu_{32} & a_{33}\nu_{33} & \cdots & a_{3N}\nu_{3N} \\ \vdots & \vdots & \vdots & \ddots & \vdots \\ a_{N1}\nu_{N1} & a_{N2}\nu_{N2} & a_{N3}\nu_{N3} & \cdots & a_{NN}\nu_{NN} \end{bmatrix}.$$

By solving equation (32) using the ETD-CN method with central difference approximation, we acquire $\nu(t + \tau/2)$ as an intermediate value.

Then we repeat the procedure for (32) in the y-direction to obtain $\nu(t + \tau)$. This particular design is often referred to as the split-step finite difference (SSFD) method [64]. We implement the above mentioned strategy to solve the following two-dimensional NLSE.

We consider the two-dimensional NLSE [66]:

$$i\,\psi_t + \psi_{xx} + \psi_{yy} + |\psi|^2\psi = 0, \quad 0 < x, y < 2\pi,\ t > 0, \tag{33}$$

together with the initial and homogeneous Neumann boundary conditions

$$\psi(x, y, 0) = (1 + \sin x)(2 + \sin y), \quad 0 < x, y < 2\pi,$$

$$\psi(x, y, t)_x = \psi(x, y, t)_y = 0 \ \text{ at } x = 0,\ 2\pi;\ y = 0,\ 2\pi.$$

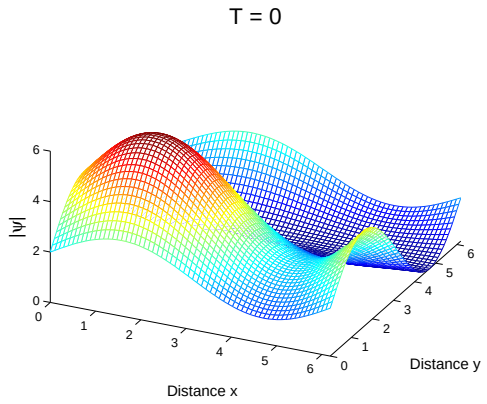

Figure 5: Modules of the initial function $(1 + \sin x)(2 + \sin y)$ in (33).

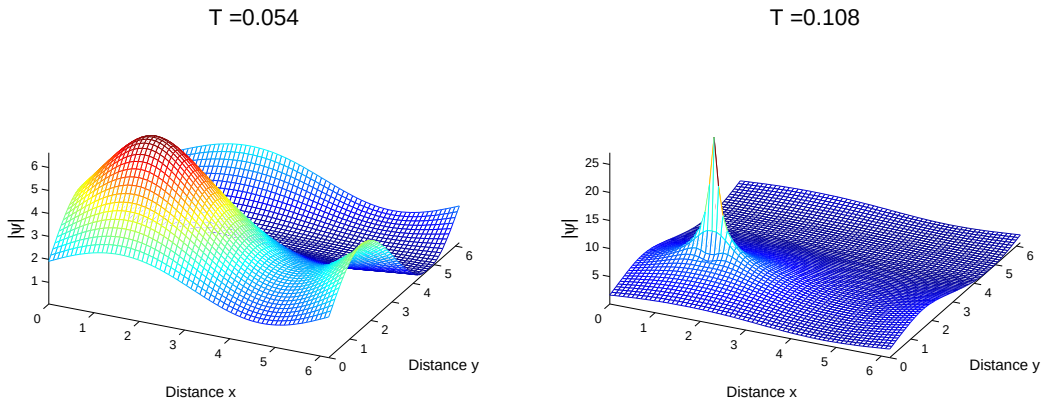

Figure 6: Solutions to Eq. (33) at $t = 0.054$ and $t = 0.108$.

Eq. (33) was considered recently by Sulem and Patera [60], and Xu and Shu [66]. The investigators reveal details of the blow-up of its solution in finite time. With our given coefficients and initial conditions, the solution of (33) also blows up in finite time. But by solving (33) using the ETD-CN with central difference approximation and blended with an ADI method ($N = 128,\ \tau = 0.001$), the solution to Eq. (33), as shown in Fig. 6, models a self-focusing laser beam as described in Section 1.2.

CHAPTER 3

THE LDG AND ETDRK4 METHODS

3.1 Introduction

In this chapter, we study the local discontinuous Galerkin (LDG) methods combined with the fourth-order exponential time differencing Runge-Kutta (ETDRK4) time discretization and combined with a fourth-order conservative method for solving the system of NLSEs:

$$i\,u_{n\,t} + \beta_n\,\nabla u_n + \delta_n\,\Delta u_n + \left(\sum_{m=1}^{\mathcal{N}} f_{nm}(|u_m|^2)\right) u_n = 0, \tag{34}$$

where $i = \sqrt{-1},\ u_n \equiv u_n(r,\ t),\ n = 1, 2, ..., \mathcal{N},\ t \geq 0,\ r \in \Omega = \mathbb{R}^d$ and $d = 1, 2$. Based on different choices of numerical fluxes, we propose both the energy-conserving and the energy-dissipative LDG methods. The stability of the numerical methods are discussed analytically. The numerical methods are proven to be highly efficient and stable for long-range soliton computations. Extensive numerical examples are provided to illustrate the accuracy, efficiency and reliability of the proposed methods.

3.2 The local discontinuous Galerkin method

3.2.1 Notations

The computational domain $I = [a, b]$ is divided into N subintervals called cells. We denote the cells by $I_j = [x_{j-1/2}, x_{j+1/2}]$ for $j = 1, \cdots, N$. $x_j = (x_{j-1/2} + x_{j+1/2})/2$ is the center of a cell, and the mesh size is $h_j = x_{j+1/2} - x_{j-1/2}$. The complex piecewise polynomial space V_h^k is defined as the space of polynomials P^k of degree at most k in

each cell I_j, that is

$$V_h^k = \{v : v \in P^k(I_j) \text{ for } x \in I_j, \quad j = 1, \cdots, N\}.$$

Functions in V_h^k could have discontinuities across the cell interfaces, and are complex valued functions since the NLSE admits complex solutions.

We denote the numerical solution by u_h, which belongs to the finite polynomial space V_h^k. $(u_h)^+_{j+1/2}$ and $(u_h)^-_{j+1/2}$ are the limit values of u_h at $x_{j+1/2}$ from the right cell I_{j+1} and from the left cell I_j, respectively. We use notations $[u_h] = u_h^+ - u_h^-$ and $\{u_h\} = (u_h^+ + u_h^-)/2$ to represent the jump and the average of the function u_h at the cell interfaces. For any complex function w, its conjugate is denoted by w^*. The inner product of two functions w and r, and the L^2 norm of w over the interval I_j are given by

$$(w, r)_{I_j} = \int_{I_j} w r^* dx, \qquad \|w\|^2_{I_j} = \int_{I_j} w w^* dx = \int_{I_j} |w|^2 dx,$$

respectively.

3.2.2 The LDG method

We define the semi-discrete LDG method for the NLSE

$$iu_t + \epsilon u_{xx} + i(g(|u|^2)u)_x + f(|u|^2)u = 0, \tag{35}$$

with an initial condition

$$u(x, 0) = u_0(x), \tag{36}$$

and periodic boundary conditions. Here $f(u)$ and $g(u)$ are smooth nonlinear functions. The periodic boundary conditions can be changed to other types of boundary conditions. Also, we remark that the extension of the proposed LDG method to the

system of NLSEs (34) is straightforward, as these equations are coupled through the last term $(\sum_{m=1}^{\mathcal{N}} \beta_{nm}|u_m|^2)u_n$ only, and that term does not include derivatives.

First, we introduce an auxiliary variable $q = u_x$, and write the wave equation into a first-order system

$$\begin{aligned} iu_t + \epsilon q_x + i(g(|u|^2)u)_x + f(|u|^2)u = 0, \\ q - u_x = 0. \end{aligned} \tag{37}$$

The LDG method for (37) is then formulated as follows: find u_h, $q_h \in V_h^k$, such that

$$\begin{aligned} & i((u_h)_t,\, v)_{I_j} - (\epsilon q_h,\, v_x)_{I_j} + \epsilon(\hat{q}_h(v^*)^-)_{j+\frac{1}{2}} - \epsilon(\hat{q}_h(v^*)^+)_{j-\frac{1}{2}} - i(g(|u_h|^2)u_h,\, v_x)_{I_j} \\ & \quad + i(\widehat{gu_h}(v^*)^-)_{j+\frac{1}{2}} - i(\widehat{gu_h}(v^*)^+)_{j-\frac{1}{2}} + (f(|u_h|^2)u_h,\, v)_{I_j} = 0, \end{aligned} \tag{38}$$

$$(q_h,\, w)_{I_j} + (u_h,\, w_x)_{I_j} - (\hat{u}_h(w^*)^-)_{j+\frac{1}{2}} + (\hat{u}_h(w^*)^+)_{j-\frac{1}{2}} = 0. \tag{39}$$

for all test functions v, $w \in V_h^k$. The hatted terms, $\hat{q}_h$, $\widehat{gu_h}$ and $\hat{u}_h$, in (38)-(39) are the cell boundary terms obtained from integration by parts, and they are the so-called numerical fluxes. For the pair of $\hat{q}_h$ and $\hat{u}_h$, we could use the simple alternating fluxes:

$$\hat{q}_h = q_h^-, \qquad \hat{u}_h = u_h^+, \tag{40}$$

Since the choice of the fluxes (40) is not unique, we can choose different numerical fluxes, such as

$$\hat{q}_h = q_h^+, \qquad \hat{u}_h = u_h^-. \tag{41}$$

For the other flux term $\widehat{gu_h}$, we could follow the approach in [66] and define

$$\widehat{gu_h} = \hat{g}(|u_h^-|^2, |u_h^+|^2)\tilde{u}_h, \tag{42}$$

where

$$\tilde{u}_h = \theta u_h^{up} + (1-\theta)\{u_h\}, \quad 0 < \theta \le 1, \quad u_h^{up} = \begin{cases} u_h^- & \text{if } \hat{g} \ge 0, \\ u_h^+ & \text{if } \hat{g} < 0, \end{cases}$$

and $\hat{g}(a,b)$ is a monotone flux, such as the Lax-Friedrichs flux,

$$\hat{g}(a,b) = \frac{1}{2}(g(a) + g(b) - \gamma(b-a)), \quad \gamma = \max_l |g'(l)|.$$

This resulting scheme is denoted as the LDG-D scheme. We could also define the flux $\widehat{gu_h}$ as

$$\widehat{gu_h} = \frac{\int_{|u_h^-|^2}^{|u_h^+|^2} g(s)ds}{[|u_h|^2]}\{u_h\} = \frac{[G(|u_h|^2)]}{[|u_h|^2]}\{u_h\}, \tag{43}$$

where

$$G(w) = \int^w g(s)ds. \tag{44}$$

This resulting scheme is called the LDG-C scheme, where the 'C' and 'D' stand for conservative and dissipative, respectively, representing the energy-conserving and energy-dissipative property of the underlying schemes.

For simplicity, we introduce the notation

$$\mathcal{T}_j(r,s;\hat{r}) = -\int_{I_j} rs_x dx + (\hat{r}s^-)_{j+\frac{1}{2}} - (\hat{r}s^+)_{j-\frac{1}{2}}, \tag{45}$$

and the LDG methods (38)-(39) become

$$i((u_h)_t,\, v)_{I_j} + \epsilon\mathcal{T}_j(q_h, v^*; \hat{q}_h) + i\mathcal{T}_j\left(g(|u_h|^2)u_h, v^*; \widehat{gu_h}\right) + (f(|u_h|^2)u_h,\, v)_{I_j} = 0, \tag{46}$$

$$(q_h,\, w)_{I_j} = \mathcal{T}_j(u_h, w^*; \hat{u}_h). \tag{47}$$

One can easily observe that

$$\sum_j \left(\mathcal{T}_j(a,b;a^-) + \mathcal{T}_j(b,a;b^+)\right) = 0, \tag{48}$$

3.2.3 Projections

We use P to denote the L^2 projection of a function $\omega(x)$ with $k+1$ continuous derivatives into space V_h^k, that is:

$$(P\omega, \phi)_\Omega = (\omega, \phi)_\Omega,$$

for any $\phi \in P^k$ on K.

A one-dimensional projection P^- for a real-valued function ω, which projects ω into the one-dimensional piecewise polynomial space of degree k while taking the values of ω at the cell interface, is defined as

$$(P^-\omega, \phi)_{I_j} = (\omega, \phi)_{I_j}, \quad \forall \phi \in P^{k-1}(I_j) \quad \text{and} \quad (P^-\omega)^-(x_{j+\frac{1}{2}}) = \omega^-(x_{j+\frac{1}{2}}). \tag{49}$$

Similarly, the one-dimensional projection $P^+\omega$ is defined as the projection of ω such that

$$(P^+\omega, \phi)_{I_j} = (\omega, \phi)_{I_j}, \quad \forall \phi \in P^{k-1}(I_j) \quad \text{and} \quad (P^+\omega)^+(x_{j-\frac{1}{2}}) = \omega^+(x_{j-\frac{1}{2}}).$$

For these projections, it is easy to show (see [10]):

$$\|\omega^e\| + h\|\omega^e\|_\infty + h^{\frac{1}{2}}\|\omega^e\|_{\Gamma_h} \le Ch^{k+1}, \tag{50}$$

where $\omega^e = \omega - P\omega$ or $\omega^e = \omega - P^\pm\omega$, and Γ_h denotes the set of boundary points of all cells. The constant C depends on the function ω, but is independent of the mesh size h.

Let us now denote the errors for the function ω by

$$e_\omega = \omega - \omega_h, \qquad \eta_\omega = \omega - P^\pm\omega, \qquad \zeta_\omega = P^\pm\omega - \omega_h, \tag{51}$$

which represent the errors between the numerical solution and the exact solution, the projection errors, and the errors between the numerical solution and the particular projection of the exact solution, respectively. The signs of the projection $P^\pm$ in (51) are consistent with the choice of the numerical fluxes in (40).

3.2.4 LDG for the two-dimensional NLSEs

Let us consider the two-dimensional NLSE

$$iu_t + u_{xx} + u_{yy} + f(|u|^2)u = 0 \tag{52}$$

with the initial condition

$$u(x, y, 0) = u_0(x, y)$$

and periodic boundary conditions at $x = 0, L$ and $y = 0, L$.

The LDG method is defined by rewriting Eq. (52) into a first-order system:

$$iu_t + p_x + q_y + f(|u|^2)u = 0,$$

$$p - u_x = 0,$$

$$q - u_y = 0.$$

Assume the domain Ω is polygonal and denote $\mathcal{T}_{\Delta x}$ as a triangulation of Ω. The finite element space is denoted as $V_{\Delta x} = \{v : v \in P^k(K) \text{ for } \forall K \in \mathcal{T}_{\Delta x}\}$. To apply the LDG method, we try to find $u, p, q \in V_{\Delta x}$, such that $\forall v, w, z \in V_{\Delta x}$,

$$\begin{aligned}
i\int_K u_t v dxdy - \int_K p v_x dxdy + \int_{\partial K} \widehat{p_{n_{x,K}}} v^{intK} ds \\
- \int_K q v_y dxdy + \int_{\partial K} \widehat{q_{n_{y,K}}} v^{intK} ds + \int_K f(|u|^2) uv dxdy = 0, \\
\int_K p w dxdy + \int_K u w_x dxdy - \int_{\partial K} \widehat{u_{n_{x,K}}} w^{intK} ds = 0, \\
\int_K q z dxdy + \int_K u z_y dxdy - \int_{\partial K} \widehat{u_{n_{y,K}}} z^{intK} ds = 0.
\end{aligned}$$

3.3 Energy conservation of the LDG method

The L^2 stability of the LDG-D method, i.e. $\frac{d}{dt}\int |u_h|^2 dx \leq 0$, has been proved in [66]. In this subsection, we will show that the LDG-C method conserves the energy exactly, which will also give us its L^2 stability.

Proposition 3.5 *The solution to the semi-discrete LDG-C method* (38)-(39) *with the choice of numerical fluxes* (40)-(43) *conserves the energy*

$$E_h(t) = \|u_h\|_I^2 = \int_I |u_h|^2 dx \tag{53}$$

exactly for all time.

Proof 3.6 *We first choose the test function* $v = u_h$ *in* (38) *and* $w = \epsilon q_h$ *in* (39). *The sum of these two equations gives*

$$\begin{aligned} & i((u_h)_t,\, u_h)_{I_j} + \epsilon \mathcal{T}_j(q_h, u_h^*; q_h^-) + i\mathcal{T}_j\left(g(|u_h|^2)u_h, u_h^*; \widehat{gu_h}\right) \\ & + (f(|u_h|^2)u_h,\, u_h)_{I_j} + \epsilon(q_h,\, q_h)_{I_j} - \epsilon \mathcal{T}_j(u_h, q_h^*; u_h^+) = 0. \end{aligned} \tag{54}$$

We take the complex conjugate for every term in Eq. (54)

$$\begin{aligned} & - i((u_h^*)_t,\, u_h^*)_{I_j} + \epsilon \mathcal{T}_j(q_h^*, u_h; (q_h^*)^-) - i\mathcal{T}_j\left(g(|u_h|^2)u_h^*, u_h; \widehat{gu_h^*}\right) \\ & + (f(|u_h|^2)u_h^*,\, u_h^*)_{I_j} + \epsilon(q_h^*,\, q_h^*)_{I_j} - \epsilon \mathcal{T}_j(u_h^*, q_h; (u_h^*)^+) = 0. \end{aligned} \tag{55}$$

By subtracting Eqs. (54) *and* (55), *summing over all cells, and using* (48), *we have*

$$i\frac{d}{dt}\|u_h\|_I^2 + i\sum_j \left(\mathcal{T}_j\left(g(|u_h|^2)u_h, u_h^*; \widehat{gu_h}\right) + \mathcal{T}_j\left(g(|u_h|^2)u_h^*, u_h; \widehat{gu_h^*}\right)\right) = 0.$$

Following the definition (43) *of the flux* $\widehat{gu_h}$, *we have*

$$\begin{aligned} & \sum_j \mathcal{T}_j\left(g(|u_h|^2)u_h, u_h^*; \widehat{gu_h}\right) + \sum_j \mathcal{T}_j\left(g(|u_h|^2)u_h^*, u_h; \widehat{gu_h^*}\right) \\ & = \sum_j \left[- \int_{I_j} g(|u_h|^2)u_h(u_h^*)_x dx + (\widehat{gu_h}(u_h^*)^-)_{j+\frac{1}{2}} - (\widehat{gu_h}(u_h^*)^+)_{j-\frac{1}{2}} \right. \\ & \qquad \left. - \int_{I_j} g(|u_h|^2)u_h^*(u_h)_x dx + (\widehat{gu_h^*}(u_h)^-)_{j+\frac{1}{2}} - (\widehat{gu_h^*}(u_h)^+)_{j-\frac{1}{2}} \right] \\ & = -\sum_j \int_{I_j} g(|u_h|^2)(|u_h|^2)_x dx - \sum_j \frac{[G(|u_h|^2)]}{[|u_h|^2]} \left(\{u_h\}[u_h^*] + \{u_h^*\}[u_h]\right)\Big|_{j+\frac{1}{2}} \\ & = \sum_j [G(|u_h|^2)]_{j+\frac{1}{2}} - \sum_j [G(|u_h|^2)]_{j+\frac{1}{2}} = 0, \end{aligned}$$

where G is the antiderivative of g, as defined in (44)*. Therefore, we have*

$$\frac{d}{dt}\|u_h\|_I^2 = 0.$$

and the quantity E_h is invariant in time.

Remark 3.1 *The above energy conservation property is proven for the single NLSE. The same results hold for the $\mathcal{N}$-coupled NLSE* (34)*, which can be proven using a similar technique.*

3.4 The ETDRK4 method

The ETDRK4 method was constructed to solve the equation of the form

$$u_t = \mathcal{L}u + \mathcal{F}(u,t), \tag{56}$$

where $\mathcal{L}$ is a linear operator and $\mathcal{F}$ is nonlinear. After being discretized in space, equation (56) can be written as a system of ODEs of the form

$$u_t + Au = F(u,t). \tag{57}$$

Considering the LDG method applied to a single one-dimensional NLSE in the system (34), the semi-discrete method can be rewritten as

$$\begin{aligned} \mathbf{M}\frac{dU}{dt} + \mathbf{S}U &= \mathbf{F}(U) \\ \Rightarrow \frac{dU}{dt} + \mathbf{M}^{-1}\mathbf{S}U &= \mathbf{M}^{-1}\mathbf{F}(U), \end{aligned} \tag{58}$$

which is in the form of (57).

In Eq. (58), U is a $kN \times 1$ vector containing coefficients of the solution $u_h \in V_h^k$ on the polynomial basis. Letting $xi = (x - x_i)/dx_i$ in the computational cell

$[x_{i-0.5}, x_{i+0.5}]$, the basis in this cell is the set: $1,\ xi,\ xi^2, ...,\ xi^k$, where k is the degree of polynomial used in the approximation. $\mathbf{M}$ is the mass matrix, which is a block tridiagonal $kN \times kN$ matrix. The basis is not orthonormal, thus the mass matrix is needed. $\mathbf{M}U$ approximates $\int_{I_j} u_h v^* dx$. $\mathbf{S}$ is the stiffness matrix, whose dimension is $kN \times kN$, and $\mathbf{S}U$ approximats the linear terms containing the numerical fluxes, as indicated in Eqs. (38) and (39). $\mathbf{F}(U)$ approximates the projection of the nonlinear terms into space V_h^k.

We integrate equation (57) over a single time step from $t = t^n$ to $t^{n+1} = t^n + \Delta t$ (see also [11, 39, 45]) and get

$$u(t^{n+1}) = e^{-\tau A} u(t^n) + e^{-\tau A} \int_0^\tau e^{sA} F(u(t^n + s), t^n + s) ds. \tag{59}$$

To be consistent with the notations in Subsection 3.2.1, we denote the numerical approximation of $u(t^n)$ by u_h^n and denote $F(u_h^n, t^n)$ by F_h^n. The time step Δt is set as τ.

Different time discretization for a particular ETD is obtained based on the formulation (59). For example, the first order ETD takes the form of

$$u_h^{n+1} = e^{-\tau A} u_h^n + A^{-1}(I - e^{-\tau A}) F_h^n. \tag{60}$$

Several different ETD approximations are listed in [67], here we consider the fourth-order ETD scheme introduced in [11, 37]. In [39], the scheme was modified so that the resulting ETDRK4 scheme does not require computation of higher powers of the matrix inverse. As explained in [39], the term e^{-z} is approximated by the fourth-order (2, 2)-Padé scheme and the ETDRK4 comes as

$$\begin{aligned} u_h^{n+1} &= R_{2,2}(\tau A) u_h^n + P_1(\tau A) F(u_h^n, t_n) \\ &\quad + P_2(\tau A)\Big(F(a^n, t_n + \tau/2) + F(b^n, t_n + \tau/2)\Big) + P_3(\tau A) F(c^n, t_n + \tau), \end{aligned} \tag{61}$$

where

$$\begin{aligned}
R_{2,2}(\tau A) &= (12I - 6\tau A + \tau^2 A^2)(12I + 6\tau A + \tau^2 A^2)^{-1}, \\
P_1(\tau A) &= \tau(2I - \tau A)(12I + 6\tau A + \tau^2 A^2)^{-1}, \\
P_2(\tau A) &= 4\tau(12I + 6\tau A + \tau^2 A^2)^{-1}, \\
P_3(\tau A) &= \tau(2I + \tau A)(12I + 6\tau A + \tau^2 A^2)^{-1}, \\
a^n &= R_{2,2}\left(\tau A/2\right) u_h^n + P(\tau A) F(u_h^n, t_n), \\
b^n &= R_{2,2}\left(\tau A/2\right) u_h^n + P(\tau A) F(a^n, t_n + \tau/2), \\
c^n &= R_{2,2}\left(\tau A/2\right) a^n + P(\tau A)\Big(2F(b^n, t_n + \tau/2) - F(u_h^n, t_n)\Big), \\
P(\tau A) &= 24\tau(48I + 12\tau A + \tau^2 A^2)^{-1}.
\end{aligned}$$

We notice that in this scheme, the matrix inverses we need are $(12I + 6\tau A + \tau^2 A^2)^{-1}$ and $(48I + 12\tau A + \tau^2 A^2)^{-1}$. We can compute and store them during the initialization process to save computational time. To avoid the high condition numbers and reduce truncation errors in computing the power of the matrices, a partial fraction decomposition is used for scheme (61), as explained in [39]. The ETDRK4 scheme is modified to the following four steps, where $Re(z)$ denotes the real part of z:

1. a^n is updated by

$$a^n = u_h^n + 2\,Re(\alpha),$$

where α is the solution of

$$(\tau A - \tilde{d}_1 I)\alpha = \tilde{w}_1 u_h^n + \tau\,\tilde{\Omega}_1 F(u_h^n,\, t_n).$$

2. b^n is updated by

$$b^n = u_h^n + 2\,Re(\beta),$$

where β is the solution of

$$(\tau A - \tilde{d}_1 I)\beta = \tilde{w}_1 u_h^n + \tau\,\tilde{\Omega}_1 F(a^n,\, t_n + \tau/2).$$

3. c^n is updated by

$$c^n = a^n + 2\,Re(\gamma),$$

where γ is the solution of

$$(\tau A - \tilde{d}_1 I)\gamma = \tilde{w}_1 a^n + \tau\,\tilde{\Omega}_1(2F(b^n,\, t_n + \tau/2) - F(u_h^n,\, t_n)).$$

4. u_h^{n+1} is updated by

$$u_h^{n+1} = u_h^n + 2\,Re(\phi),$$

where ϕ is the solution of

$$\begin{aligned}(\tau A - d_1 I)\phi \;&= w_1 u_h^n + \tau w_{11} F(u_h^n,\, t^n) + \tau w_{21} F(a^n,\, t^n + \tau/2) \\ &\quad + \tau w_{21} F(b^n,\, t^n + \tau/2) + \tau w_{31} F(c^n,\, t^n + \tau).\end{aligned}$$

Here, w and d are the coefficients used for the weights and poles:

$d_1 = -3.0 + i\,1.73205080756887729352,$

$w_1 = -6.0 - i\,10.3923048454132637611,$

$w_{11} = -0.5 - i\,1.44337567297406441127,$

$w_{21} = -i\,1.15470053837925152901,$

$w_{31} = 0.5 + i\,0.28867513459481288225,$

$\tilde{d}_1 = -6.0 + i\,3.4641016151377545870548,$

$\tilde{w}_1 = -12.0 - i\,20.78460969082652752232935,$

$\tilde{\Omega}_1 = -i\,3.46410161513775458705.$

3.5 Stability regions

The stability of the ETDRK4 can be analyzed by plotting its stability regions (see also [11] and [29]). Consider the nonlinear ODE

$$u_t = cu + F(u), \tag{62}$$

where $F(u)$ is a nonlinear function. Assume that a fixed point u_0 exists, such that $cu_0 + F(u_0) = 0$. Suppose u is a perturbation of u_0 and $\lambda = F'(u_0)$, then Eq. (62) can be linearized as

$$u_t = cu + \lambda u. \tag{63}$$

If $\mathrm{Re}(c+\lambda) < 0$, we can tell that the fixed point u_0 is stable. Let $x = \lambda\tau$ and $y = c\tau$ and apply the ETDRK4 method to (63), then we can compute the amplification factor:

$$\frac{u_{n+1}}{u_n} = r(x,\ y) = c_0 + c_1 x + c_2 x^2 + c_3 x^3 + c_4 x^4, \tag{64}$$

where

$$\begin{aligned}
c_0 &= \frac{1327104 - 331776y - 55296y^2 + 20736y^3 + 3456y^4 - 2160y^5 + 372y^6 - 30y^7 + y^8}{(48 - 12y + y^2)^3(12 - 6y + y^2)} \\
c_1 &= \frac{1327104 - 331776y - 55296y^2 + 20736y^3 - 3456y^4 + 432y^5 - 36y^6}{(48 - 12y + y^2)^3(12 - 6y + y^2)} \\
c_2 &= \frac{663552 - 165888y - 27648y^2 + 8064y^3 - 288y^4 - 48y^5}{(48 - 12y + y^2)^3(12 - 6y + y^2)} \\
c_3 &= \frac{221184 - 55296y - 9216y^2 - 1152y^3}{(48 - 12y + y^2)^3(12 - 6y + y^2)} \\
c_4 &= \frac{55296 - 27648y}{(48 - 12y + y^2)^3(12 - 6y + y^2)}.
\end{aligned}$$

We notice that when $y = 0$, the amplification factor (64) becomes

$$r(x, 0) = 1 + x + \frac{1}{2}x^2 + \frac{1}{6}x^3 + \frac{1}{24}x^4,$$

which is the amplification factor for the explicit fourth-order Runge-Kutta (RK4) method. The stability regions are shown in Fig. 7, where we plot the real and imaginary part of x with fixed y as real values 0, -5, -10, -20. It can be observed that as $|c\tau|$ increases, the stability region expands, which indicates the behavior of the nonlinear stability of the method.

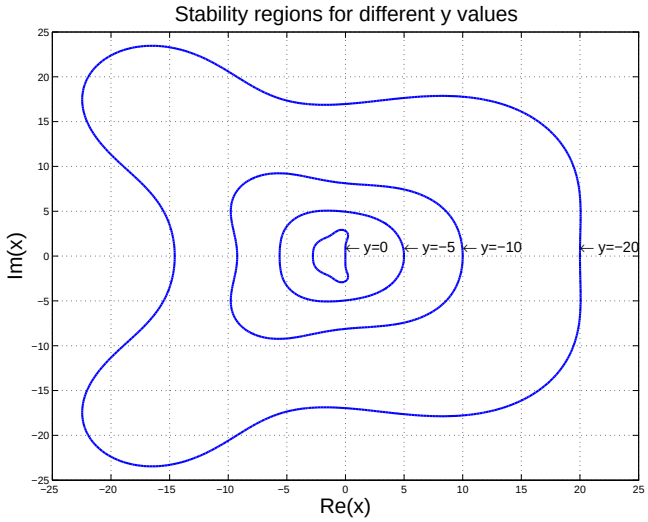

Figure 7: Stability regions of the ETDRK4 with y fixed to negative values.

3.6 An energy conserving time-stepping method

In section 3.2, we proposed both energy conserving (LDG-C) and energy dissipative (LDG-D) methods for the Schrödinger equation. In order to extend the energy conservation property of the semi-discrete LDG-C method to the fully discrete method, it is necessary to employ time stepping methods which also conserve discrete energy. A family of temporal integrators having arbitrarily high order in time and which does preserve the conservation laws up to round-off error is the implicit Runge-Kutta collocation type methods associated with the diagonal elements of the Padé table for e^z. In this section, we consider the first two members of this family of energy conserving schemes.

For the NLSE taking the form of

$$iu_t + \epsilon u_{xx} + i(au)_x + f(|u|^2)u = 0, \tag{65}$$

the fully discrete second-order in time LDG-C approximations are constructed using

the *midpoint rule* in the following manner:

$$i\left(\frac{u_h^{n+1}-u_h^n}{\tau},\, v\right)_{I_j} + \epsilon\mathcal{T}_j\left(\frac{q_h^{n+1}+q_h^n}{2}, v^*; \frac{\hat{q}_h^{n+1}+\hat{q}_h^n}{2}\right) + i\mathcal{T}_j\left(a\frac{u_h^{n+1}+u_h^n}{2}, v^*; \frac{a\hat{u}_h^{n+1}+a\hat{u}_h^n}{2}\right) + \left(\widetilde{f(|u_h|^2)}\frac{u_h^{n+1}+u_h^n}{2},\, v\right)_{I_j} = 0, \tag{66}$$

$$(q_h^n,\, w)_{I_j} = \mathcal{T}_j(u_h^n, w^*; \hat{u}_h^n), \tag{67}$$

$$(q_h^{n+1},\, w)_{I_j} = \mathcal{T}_j(u_h^{n+1}, w^*; \hat{u}_h^{n+1}). \tag{68}$$

for all test functions $v,\, w \in V_h^k$, where

$$\widetilde{f(|u_h|^2)} = \frac{F(|u^{n+1}|^2) - F(|u^n|^2)}{|u^{n+1}|^2 - |u^n|^2},$$

with $F(a) = \int f(s)ds$.

By taking $v = (u_h^{n+1}+u_h^n)/2$, $w = (q_h^{n+1}+q_h^n)/2$ in (66)-(68) and using some simple algebra, we can see that $\|u_h^{n+1}\|_I^2 = \|u_h^n\|_I^2$, which is the discrete energy conservation property. Even more, for the case when $a = 0$, the NLSE equation conserves the term $\|q\|_I^2 + F(|u|^2)$, in addition to the energy $\|u\|^2$. We can also prove that the above energy conserving method in (66)-(68) conserves the term $\|q^n\|_I^2 + F(|u_h^n|^2)$ in the discrete level as well.

A fourth order energy conserving time-stepping method based on the midpoint rule is provided in [9] to solve the nonlinear system (57). Let $u^{n+1} \in V_h^k$ be defined as

$$u^{n+1} = u^n + \sqrt{3}(u^{n,2} - u^{n,1}), \tag{69}$$

with $u^{n,1}$ and $u^{n,2}$ given as solutions of the coupled system of equations,

$$u^{n,1} - u^n + \tau(a_{11}f^{n,1} + a_{12}f^{n,2}) = 0,$$
$$u^{n,2} - u^n + \tau(a_{21}f^{n,1} + a_{22}f^{n,2}) = 0,$$

where $f^{n,i} = Au^{n,i} - F(u^{n,i}, t)$, $i = 1, 2$ and $a_{11} = a_{22} = 1/4$, $a_{12} = 1/4 - \sqrt{3}/6$, $a_{21} = 1/4 + \sqrt{3}/6$.

3.7 Numerical experiments

3.7.1 A Single NLSE

We consider the single NLSE

$$i\, u_t + u_{xx} + i\, \alpha(|u|^2 u)_x + \beta|u|^2 u + \gamma|u|^4 u = 0, \tag{70}$$

which admits an exact solution

$$u(x, t) = Z\, \exp(i(cx - \omega t)), \tag{71}$$

where $\omega = c^2 + \alpha|Z|^2 c - \beta|Z|^2 - \gamma|Z|^4$. In this numerical test, we set $\alpha = 0.5, \beta = \gamma = 1, Z = c = 1$, with periodic boundary conditions in $[0, 2\pi]$.

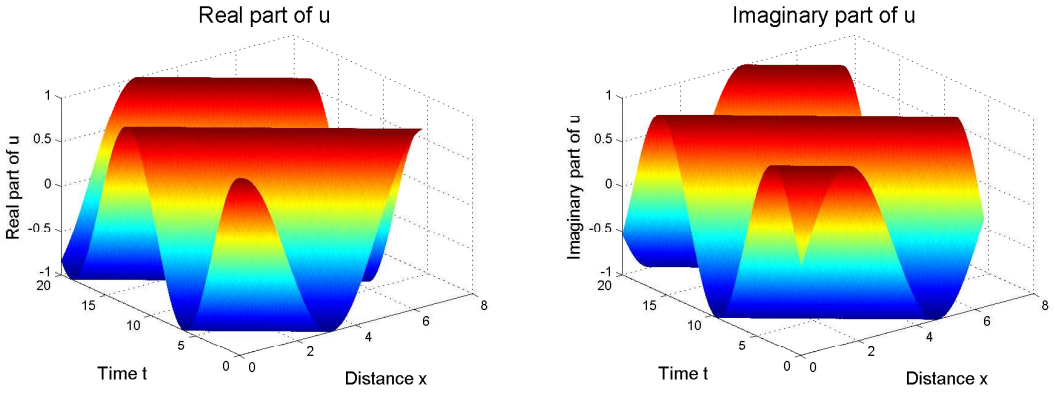

Figure 8: Surface plots of the results by the ETDRK4 solving single NLSE (70) using LDG-C in space ($N = 128$, $\tau = 0.1$ and T=[0, 20]).

The surface plots of the real and imaginary parts of the results by the ETDRK4

using LDG-C are shown in Fig. 8. It can be seen from the figures that the real and imaginary parts change periodically. The absolute value $|u| = 1$ for all the t.

Table 4: A comparison of efficiencies of Crank-Nicolson method [32], the Second-order conservative method [9], and the ETD-CN method [45] using LDG-C ($N = 128$, $\tau = 0.01$) on (70).

	Crank-Nicolson			Second-order conservative			ETD-CN		
T	CPU	L_2 error	energy	CPU	L_2 error	energy	CPU	L_2 error	energy
5	5.57e+2	0.00157	2.506628	6.12e+2	0.00125	2.506628	2.5206	6.1342e-5	2.506628
10	9.36e+2	0.00315	2.506628	1.02e+3	0.00251	2.506628	4.2736	1.2268e-4	2.506731
20	1.78e+3	0.00630	2.506628	1.93e+3	0.00503	2.506628	7.4643	2.4536e-4	2.506937
30	2.61e+3	0.00946	2.506628	2.91e+3	0.00754	2.506628	10.653	4.9072e-4	2.507143

Table 4 indicates the CPU time and L_2 errors of the Crank-Nicolson method [32], the second-order conservative method [9] and the ETD-CN method [45] on (70). These methods are second-order in time. The first two methods conserve the energy exactly, but they require an iterative nonlinear solver such as Newton's method [32]. The ETD-CN method achieves a higher efficiency considering the CPU time and accuracy with little sacrifice in energy conservation. Newton's method, used with the proposed schemes in the numerical tests, has a tolerance of error of $1e-8$ and a max number of iterations of 20.

Table 5: A comparison of efficiencies of the ETDRK4, RK4 and Fourth-order conservative methods using LDG-C ($N = 128$) on (70).

	ETDRK4 ($\tau = 0.1$)		RK4 ($\tau = 0.0001$)		Fourth-order conservative ($\tau = 0.1$)	
T	CPU time	L_2 error	CPU time	L_2 error	CPU time	L_2 error
5	3.0436	9.3566e-007	20.1372	2.5194e-006	6.88e+003	3.5463e-006
10	4.6826	5.6233e-006	33.1450	4.3198e-005	1.21e+004	7.0926e-006
20	7.7688	3.6756e-005	47.9093	9.0924e-005	2.19e+004	1.4185e-005
30	10.9177	9.6743e-005	60.2801	3.0351e-004	3.26e+004	2.1278e-005

Table 5 presents the advantage in efficiency of the ETDRK4. We can observe that the ETDRK4 achieves more accurate results than RK4 and the Fourth-order conservative method (69) with less CPU time. The CPU times are based on computations via a Matlab R2014a platform based on an Intel Core i5-2410M 2.30GHz workstation.

3.7.2 A 4-coupled NLSE

In this subsection, we consider the following 4-coupled NLSE:

$$\begin{aligned}
&i\,u_{1t} + i\,\frac{1}{v_1}u_{1x} + \frac{\beta_1}{2}u_{1xx} + \gamma_1\left(|u_1|^2 + 2|u_2|^2 + B|u_3|^2 + B|u_4|^2\right)u_1 = 0,\\
&i\,u_{2t} + i\,\frac{1}{v_2}u_{2x} + \frac{\beta_2}{2}u_{2xx} + \gamma_2\left(2|u_1|^2 + |u_2|^2 + B|u_3|^2 + B|u_4|^2\right)u_2 = 0,\\
&i\,u_{3t} + i\,\frac{1}{v_3}u_{3x} + \frac{\beta_1}{2}u_{3xx} + \gamma_1\left(B|u_1|^2 + B|u_2|^2 + |u_3|^2 + 2|u_4|^2\right)u_3 = 0,\\
&i\,u_{4t} + i\,\frac{1}{v_4}u_{4x} + \frac{\beta_2}{2}u_{4xx} + \gamma_2\left(B|u_1|^2 + B|u_2|^2 + 2|u_3|^2 + |u_4|^2\right)u_4 = 0,
\end{aligned} \tag{72}$$

with the initial conditions

$$\begin{aligned}
u_1(x,0) &= \sqrt{\frac{2a}{1+B}}\,\mathrm{sech}(\sqrt{2a}(x-x_0))\exp(i\,(c-\alpha)(x-x_0)),\\
u_2(x,0) &= \sqrt{\frac{2a}{1+B}}\,\mathrm{sech}(\sqrt{2a}(x-x_0))\exp(i\,(c+\alpha)(x-x_0)),\\
u_3(x,0) &= \sqrt{\frac{2a}{1+B}}\,\mathrm{sech}(\sqrt{2a}(x-x_0))\exp(i\,(c-\alpha)(x-x_0)),\\
u_4(x,0) &= \sqrt{\frac{2a}{1+B}}\,\mathrm{sech}(\sqrt{2a}(x-x_0))\exp(i\,(c+\alpha)(x-x_0)),
\end{aligned} \tag{73}$$

as well as periodic boundary conditions in $[-10,\ 40]$, where $v_1 = v_2 = v_3 = v_4 = 1,\ \beta_1 = \beta_2 = 2,\ \gamma_1 = \gamma_2 = 2,\ a = 1,\ c = 1,\ \alpha = 0.5,\ B = \frac{2}{3}$ and $x_0 = 0$. (See as well the system in [1].)

As explained in [1], the four-coupled NLSE equations can be used in modeling solitons in the high-birefringent fibers. The parameter $B = \frac{2}{3}$ for linearly birefringent

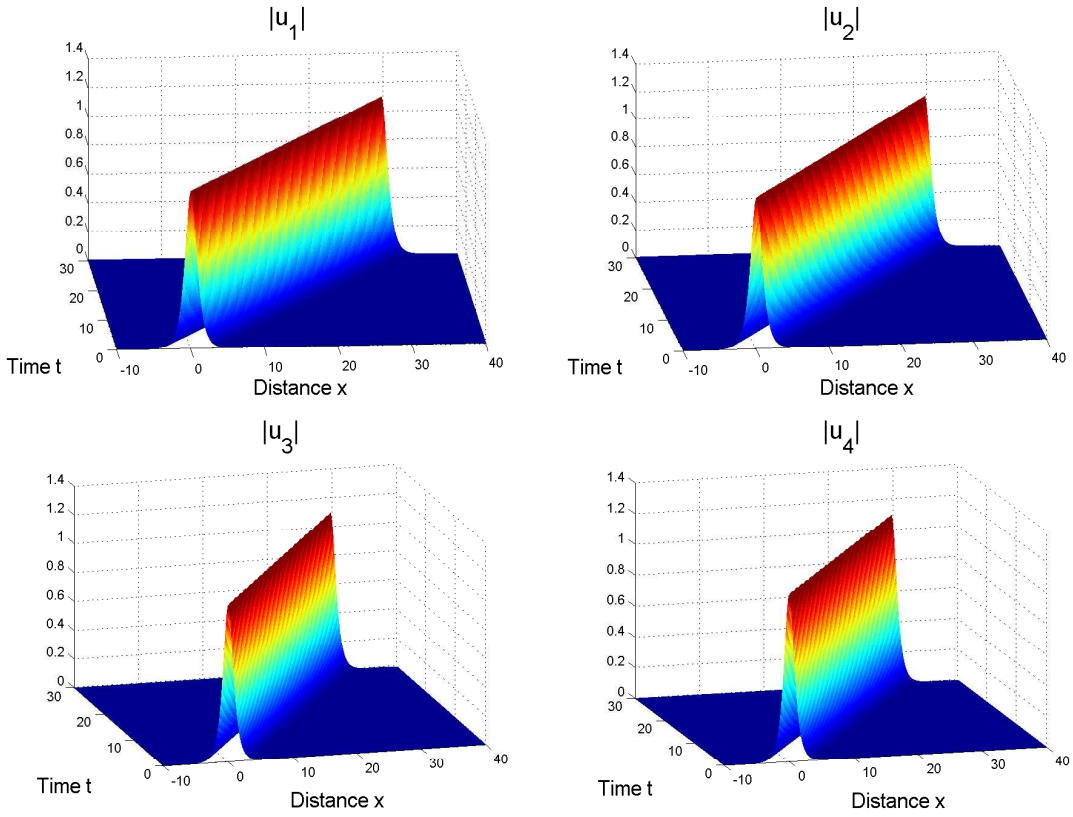

Figure 9: Solutions of the 4-coupled NLSE (72) with initial conditions (73) obtained via the ETDRK4 LDG-C method ($h = 0.1$, $\tau = 0.1$ and $T = [0, 30]$).

fibers, and β_1, β_2 are the corresponding propagation constant. Most articles do not consider the group velocity for polarization components, except for [35, 66]. In [46], we consider $\frac{1}{v_1} \neq 0$, since the convection term has significant meanings in nonlinear fiber optics. As shown in [1], even a single-mode fiber can support two degenerate modes that are polarized in two orthogonal directions. Especially, in high-birefringent fibers, the group velocity mismatch between the fast and slow components of the input pulse cannot be neglected.

We run the simulation for the coupled NLSE with the fourth order ETDRK4 LDG-C method. The numerical results are shown in Fig. 9. We observe that the numerical

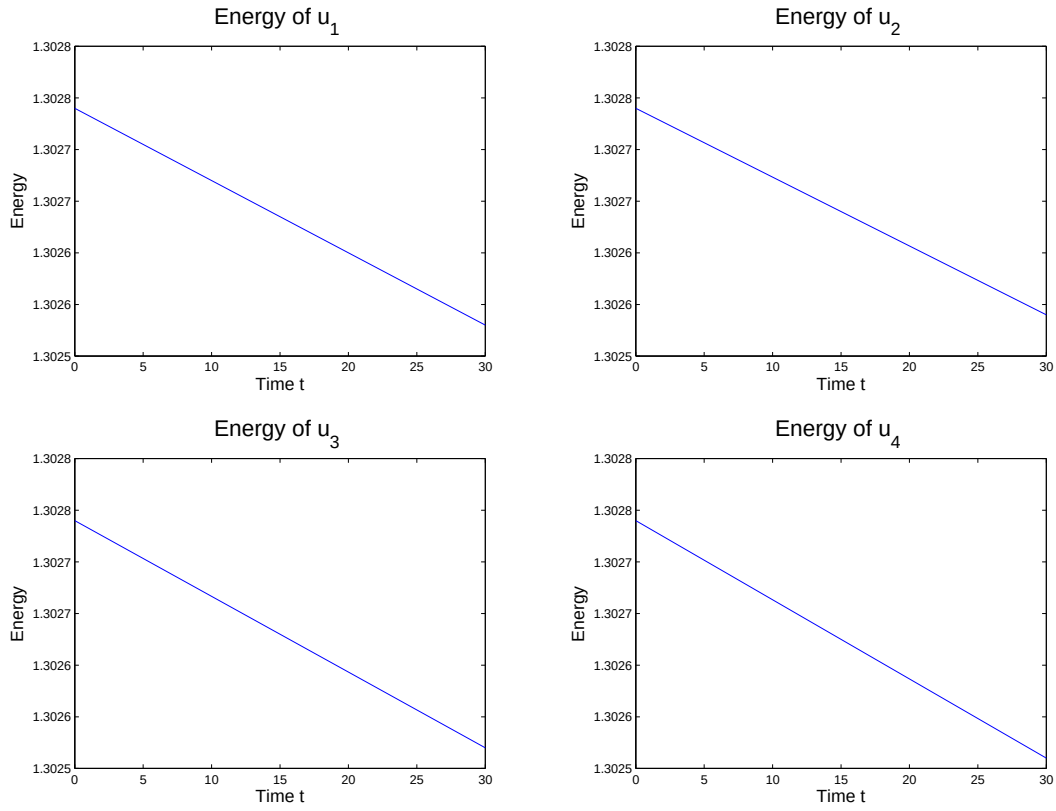

Figure 10: Time history of the energy of the 4-coupled NLSE (72) with initial conditions (73) obtained via the ETDRK4 LDG-C method ($h = 0.1$, $\tau = 0.1$ and $T = [0, 30]$).

results of (72) are soliton waves that travel along the x-direction at a speed of 1. The time history of energy, plotted in Fig. 10, indicates the energy of numerical results by ETDRK4 will decrease slightly as time goes. This numerical test demonstrates that the ETDRK4 LDG-C method works well on large systems.

3.7.3 A system of damped NLSEs

Here, we consider a standard system of two-dimensional NLSEs with group velocity dispersion terms [3]:

$$\begin{aligned} i\,u_{1t} + \beta\,\nabla u_1 + \frac{1}{2}\Delta u_1 + \varepsilon\left(|u_1|^2 + \alpha|u_2|^2\right)u_1 = 0, \\ i\,u_{2t} + \beta\,\nabla u_2 + \frac{1}{2}\Delta u_2 + \varepsilon\left(\alpha|u_1|^2 + |u_2|^2\right)u_2 = 0. \end{aligned} \tag{74}$$

In two spatial dimensions, Eq. (74) is usually associated with the following initial conditions:

$$u_1(x,y,0) = u_2(x,y,0) = \sqrt{\frac{2\alpha}{1+\pi}}\mathrm{sech}[(x-x_L)(x-x_R)(y-y_L)(y-y_R)],$$

and also the Neumann-type boundary conditions:

$$\nabla u_1(x,y,t) = \nabla u_2(x,y,t) = 0, \quad \text{for } x,\ y \in \partial\Omega.$$

The parameters are chosen as $\beta = \varepsilon = 1$, $\alpha = \frac{2}{3}$, $x_L = y_L = -1$, $x_R = y_R = 1$.

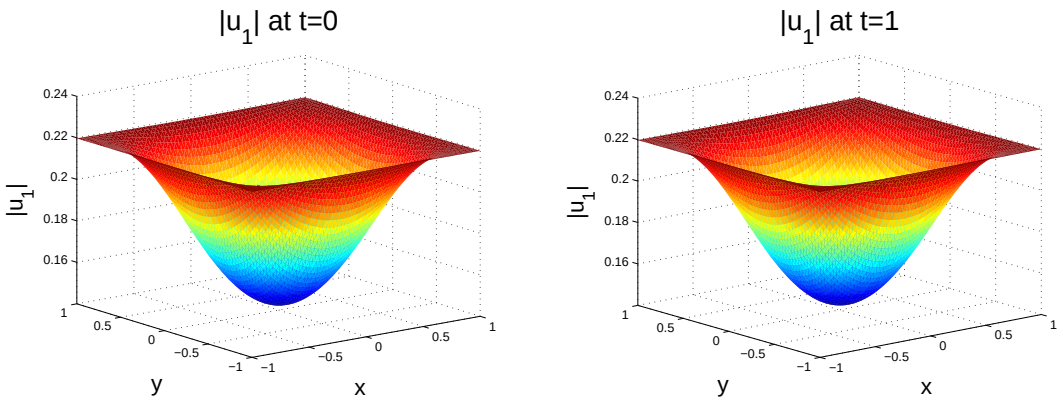

Figure 11: Surface plots of the results by the ETDRK4 solving two-dimensional system (74) using LDG in space.

The surface plots of the results of system (74) by the ETDRK4 with LDG4 method are shown in Fig. 11. From the figures we observe that system (74) models a pair of damped solitons.

Table 6: A trace of energy errors using the ETDRK4 method with LDG4 ($N = 128$) on (74).

t	Energy of u_1	Energy Error	Energy of u_2	Energy Error
0	12.516669	0	12.516669	0
0.2	12.516670	0.000001	12.516670	0.000001
0.4	12.516671	0.000002	12.516671	0.000002
0.6	12.516672	0.000003	12.516672	0.000003
0.8	12.516674	0.000005	12.516674	0.000005
1.0	12.516675	0.000006	12.516675	0.000006

Table 6 indicates how the ETDRK4 with LDG4 method performs in energy conservation solving a system of two-dimensional NLSEs.

3.7.4 Interaction of two laser beams

we consider a system of two-dimensional NLSEs [48]:

$$\begin{aligned} 2i\, u_{1t} + \nabla_{\perp}^2 u_1 + N(u)u_1 = 0, \\ 2i\, u_{2t} + \nabla_{\perp}^2 u_2 + N(u)u_2 = 0. \end{aligned} \tag{75}$$

Eq. (75) models the nonlinear interaction of two co-propagating laser beams in underdense plasmas. The nonlinear term $N(u) = (1 - \eta/\gamma)$, where $\eta = Max(0,\ 1 + \nabla_{\perp}\gamma)$ is the electron density which is normalized by unperturbed density, and $\gamma = (1 + |u_1|^2 + |u_2|^2)^{1/2}$ is the relativistic factor. u_1 and u_2 are normalized slowly varying vector potentials for the first and the second beam respectively. $\nabla_{\perp}^2 = \nabla_{yy}^2 + \nabla_{zz}^2$, where $y,\ z$ are the normalized transverse co-ordinates.

The initial conditions to (75) as given in [48] are:

$$\begin{aligned} u_1 &= u_{01}\ \exp\left(-\frac{1}{2}((y_1 - y_{01})^2 + z_1^2)\rho_{01}\right), \\ u_2 &= u_{02}\ \exp\left(-\frac{1}{2}((y_2 - y_{02})^2 + z_2^2)\rho_{02}\right), \end{aligned} \tag{76}$$

where $y = [-60,\ 60]$, $z = [-60,\ 60]$, $\rho_{01} = \rho_{02} = 8$, $u_{01} = u_{02} = 1$, $y_{01} = 10$ and $y_{02} = -10$. The boundary conditions are periodic boundary conditions.

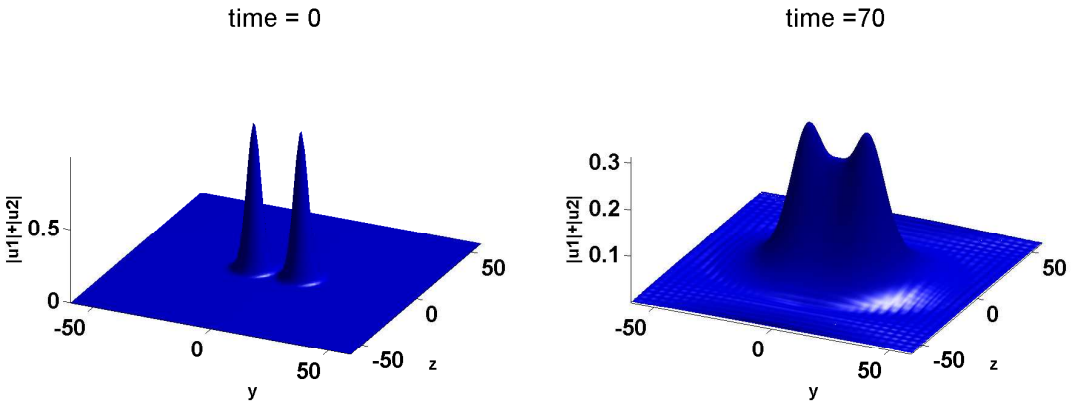

Figure 12: Solutions to Eq. (75) at $t = 0$ and $t = 70$.

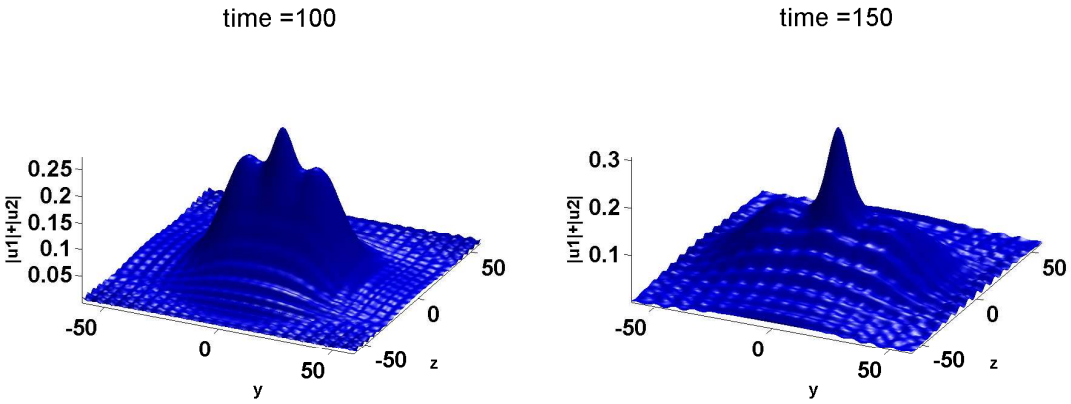

Figure 13: Solutions to Eq. (75) at $t = 100$ and $t = 150$.

Fig. 12-14 indicate how the system of NLSEs models the merging and refocusing of two self-focusing laser beams.

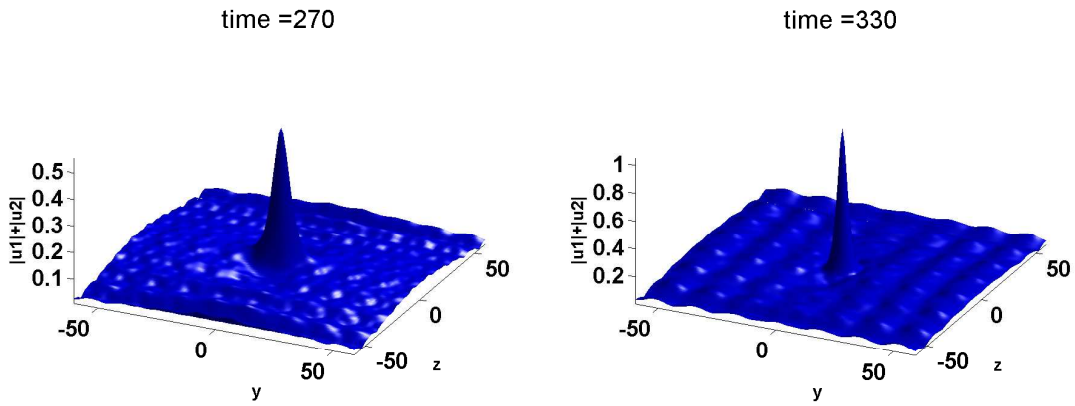

Figure 14: Solutions to Eq. (75) at $t = 270$ and $t = 330$.

CHAPTER 4

FOURTH-ORDER COMPACT SCHEMES FOR THE FNLSES

4.1 Introduction

In this chapter, the ETDRK4 scheme combined with a fourth-order compact scheme in space is proposed for space fractional coupled nonlinear Schrödinger equations (FCNLSEs). The stability and convergence of the compact scheme are discussed analytically. It is shown that the compact scheme is fourth-order convergent in space and in time. Numerical experiments are performed on systems of one, two and four fractional nonlinear Schrödinger equations (FNLSEs). The results demonstrate accuracy, efficiency, and reliability of the scheme. A linearly implicit conservative method with the fourth-order compact scheme in space is also considered and used on the system of FNLSEs.

The space fractional coupled nonlinear Schrödinger equation (FCNLSE) containing the fractional Laplacian $(-\Delta)^{\alpha/2}$ $(1 < \alpha \leq 2)$ is considered:

$$\begin{aligned} i\,u_t - \gamma\,(-\Delta)^{\alpha/2}u + \rho(|u|^2 + \beta|v|^2)u = 0, \quad x \in \mathbb{R}, \quad 0 < t \leq T \\ i\,v_t - \gamma\,(-\Delta)^{\alpha/2}v + \rho(|v|^2 + \beta|u|^2)v = 0, \quad x \in \mathbb{R}, \quad 0 < t \leq T \end{aligned} \tag{77}$$

with the initial conditions

$$\begin{aligned} u(x,\ 0) = u_0(x), \\ v(x,\ 0) = v_0(x), \end{aligned} \tag{78}$$

and homogeneous Dirichlet boundary conditions on $[x_L,\ x_R]$, where $i = \sqrt{-1}$, and the parameters γ, ρ and β are some real constants.

The fractional Laplacian can be computed as [63]

$$-(-\Delta)^{\alpha/2}u(x,\ t) = -\mathcal{F}^{-1}\left(|\xi|^{\alpha}\mathcal{F}\left(u(x,\ t)\right)\right), \tag{79}$$

where $\mathcal{F}$ is the Fourier transformation. It is also shown in [68] that the fractional Laplacian has a close relationship with the Riesz fractional derivative:

$$\frac{\partial^{\alpha}}{\partial|x|^{\alpha}}u(x,\ t) = -(-\Delta)^{\alpha/2}u(x,\ t) = -\frac{1}{2cos\frac{\pi\alpha}{2}}\left[{}_{-\infty}D_{x}^{\alpha}u(x,\ t) +_{x} D_{+\infty}^{\alpha}u(x,\ t)\right], \tag{80}$$

where $1 < \alpha < 2$. ${}_{-\infty}D_{x}^{\alpha}u(x,\ t)$ and ${}_{x}D_{+\infty}^{\alpha}u(x,\ t)$ are the left and right Riemann-Liouville derivatives:

$${}_{-\infty}D_{x}^{\alpha}u(x,\ t) = \frac{1}{\Gamma(2-\alpha)}\frac{\partial^{2}}{\partial x^{2}}\int_{-\infty}^{x}\frac{u(\xi,t)}{(x-\xi)^{\alpha-1}}d\xi,$$

and

$${}_{x}D_{+\infty}^{\alpha}u(x,\ t) = \frac{1}{\Gamma(2-\alpha)}\frac{\partial^{2}}{\partial x^{2}}\int_{x}^{+\infty}\frac{u(\xi,t)}{(\xi-x)^{\alpha-1}}d\xi,$$

Where $\Gamma(\cdot)$ is the Gamma function.

The FCNLSE (77) can be extended to a system of four equations:

$$\begin{aligned}
&i\,u_t - \gamma\,(-\Delta)^{\alpha/2}u + \rho(|u|^2 + \beta(|v|^2 + |w|^2 + |z|^2))u = 0, \quad x \in \mathbb{R}, \quad 0 < t \le T\\
&i\,v_t - \gamma\,(-\Delta)^{\alpha/2}v + \rho(|v|^2 + \beta(|u|^2 + |w|^2 + |z|^2))v = 0, \quad x \in \mathbb{R}, \quad 0 < t \le T\\
&i\,w_t - \gamma\,(-\Delta)^{\alpha/2}w + \rho(|w|^2 + \beta(|u|^2 + |v|^2 + |z|^2))w = 0, \quad x \in \mathbb{R}, \quad 0 < t \le T\\
&i\,z_t - \gamma\,(-\Delta)^{\alpha/2}z + \rho(|z|^2 + \beta(|u|^2 + |v|^2 + |w|^2))z = 0, \quad x \in \mathbb{R}, \quad 0 < t \le T
\end{aligned} \tag{81}$$

with the initial conditions taken as

$$\begin{aligned}
u(x,\ 0) = u_0(x),\ v(x,\ 0) = v_0(x),\\
w(x,\ 0) = w_0(x),\ z(x,\ 0) = z_0(x),
\end{aligned} \tag{82}$$

and homogeneous Dirichlet boundary conditions on $[x_L,\ x_R]$.

The FCNLSE (77) conserves both mass and energy [63], defined as $Q(t)$ and $E(t)$ at time t respectively:

$$\begin{aligned} Q_u(t) &= \|u(\cdot,t)\|_{L_2}^2 = \int_R |u(x,t)|^2 dx, \\ Q_v(t) &= \|v(\cdot,t)\|_{L_2}^2 = \int_R |v(x,t)|^2 dx, \end{aligned} \tag{83}$$

$$E(t) = \frac{\gamma}{2}\int_R \left(\bar{u}(-\Delta)^{\frac{\alpha}{2}}u + \bar{v}(-\Delta)^{\frac{\alpha}{2}}v\right)dx - \frac{\rho}{4}\int_R \left(|u|^4 + |v|^4 + 2\beta|u|^2|v|^2\right)dx. \tag{84}$$

The existence and uniqueness of the global solution of the FCNLSEs have been studied in [28]. To solve the FCNLSEs numerically, we need to combine a spatial discretization scheme with a time integrator. In this research, we propose the application of a fourth-order compact scheme (see [18]) to approximate the Riesz fractional derivative in space. The compact scheme in space is proved and demonstrated in numerical experiments to perform well on a space Riesz fractional diffusion equation.

The ETDRK4 scheme, which has been described in Chapter 3, is applied to solve the FNLSEs in time. A second-order linearly implicit conservative method is used in [63] for the FCNLSEs along with the second-order central difference approximation to the space fractional derivative. In this chapter, we apply this linearly implicit conservative method with the fourth-order compact scheme in space to the FCNLSEs. The efficiency and energy conservation of the conservative method are demonstrated in the numerical experiments.

4.2 Spatial discretization

As shown in [52], the left-sided Riemann-Liouville derivative ${}_{-\infty}D_x^{\alpha}v(x,\ t)$ can be approximated with an upper triangular strip matrix $B_M^{(\alpha)}$ as:

$$\begin{bmatrix} v_0^{(\alpha)} & v_1^{(\alpha)} & \cdots & v_{M-1}^{(\alpha)} & v_M^{(\alpha)} \end{bmatrix}^{\top} = B_M^{(\alpha)} \begin{bmatrix} v_M & v_{M-1} & \cdots & v_1 & v_0 \end{bmatrix}^{\top}, \tag{85}$$

where

$$B_M^{(\alpha)} = \frac{1}{h^\alpha} \begin{bmatrix} \omega_0^{(\alpha)} & \omega_1^{(\alpha)} & \ddots & \ddots & \omega_{M-1}^{(\alpha)} & \omega_M^{(\alpha)} \\ 0 & \omega_0^{(\alpha)} & \omega_1^{(\alpha)} & \ddots & \ddots & \omega_{M-1}^{(\alpha)} \\ 0 & 0 & \omega_0^{(\alpha)} & \omega_1^{(\alpha)} & \ddots & \ddots \\ \cdots & \cdots & \cdots & \ddots & \ddots & \ddots \\ 0 & \cdots & 0 & 0 & \omega_0^{(\alpha)} & \omega_1^{(\alpha)} \\ 0 & 0 & \cdots & 0 & 0 & \omega_0^{(\alpha)} \end{bmatrix}, \ \omega_j^{(\alpha)} = (-1)^j \binom{\alpha}{j}, \tag{86}$$

with the spatial discretization point $x = jh$ $(j = 0, 1, \ldots, M)$, where h is the space mesh size.

Similarly, the right-sided Riemann-Liouville derivative ${}_xD_{+\infty}^{\alpha} v(x,\ t)$ can be approximated with an lower triangular strip matrix $L_M^{(\alpha)}$ as:

$$\begin{bmatrix} v_0^{(\alpha)} & v_1^{(\alpha)} & \cdots & v_{M-1}^{(\alpha)} & v_M^{(\alpha)} \end{bmatrix}^\top = L_M^{(\alpha)} \begin{bmatrix} v_M & v_{M-1} & \cdots & v_1 & v_0 \end{bmatrix}^\top, \tag{87}$$

where

$$L_M^{(\alpha)} = \frac{1}{h^\alpha} \begin{bmatrix} \omega_0^{(\alpha)} & 0 & 0 & 0 & \cdots & 0 \\ \omega_1^{(\alpha)} & \omega_0^{(\alpha)} & 0 & 0 & \cdots & 0 \\ \omega_2^{(\alpha)} & \omega_1^{(\alpha)} & \omega_0^{(\alpha)} & 0 & \cdots & 0 \\ \ddots & \ddots & \ddots & \ddots & \cdots & \cdots \\ \omega_{M-1}^{(\alpha)} & \ddots & \omega_2^{(\alpha)} & \omega_1^{(\alpha)} & \omega_0^{(\alpha)} & 0 \\ \omega_M^{(\alpha)} & \omega_{M-1}^{(\alpha)} & \ddots & \omega_2^{(\alpha)} & \omega_1^{(\alpha)} & \omega_0^{(\alpha)} \end{bmatrix}, \ \omega_j^{(\alpha)} = (-1)^j \binom{\alpha}{j}, \tag{88}$$

The symmetric Riesz derivative of fractional order α can be approximated using the fractional centered difference formula suggested by Ortigueira [50]:

$$\begin{bmatrix} v_0^{(\alpha)} & v_1^{(\alpha)} & \cdots & v_{M-1}^{(\alpha)} & v_M^{(\alpha)} \end{bmatrix}^\top = H_M^{(\alpha)} \begin{bmatrix} v_M & v_{M-1} & \cdots & v_1 & v_0 \end{bmatrix}^\top, \tag{89}$$

where

$$H_M^{(\alpha)} = \frac{1}{h^\alpha} \begin{bmatrix} \omega_0^{(\alpha)} & \omega_1^{(\alpha)} & \omega_2^{(\alpha)} & \omega_3^{(\alpha)} & \cdots & \omega_M^{(\alpha)} \\ \omega_1^{(\alpha)} & \omega_0^{(\alpha)} & \omega_1^{(\alpha)} & \omega_2^{(\alpha)} & \cdots & \omega_{M-1}^{(\alpha)} \\ \omega_2^{(\alpha)} & \omega_1^{(\alpha)} & \omega_0^{(\alpha)} & \omega_1^{(\alpha)} & \cdots & \omega_{M-2}^{(\alpha)} \\ \ddots & \ddots & \ddots & \ddots & \cdots & \cdots \\ \omega_{M-1}^{(\alpha)} & \ddots & \omega_2^{(\alpha)} & \omega_1^{(\alpha)} & \omega_0^{(\alpha)} & \omega_1^{(\alpha)} \\ \omega_M^{(\alpha)} & \omega_{M-1}^{(\alpha)} & \ddots & \omega_2^{(\alpha)} & \omega_1^{(\alpha)} & \omega_0^{(\alpha)} \end{bmatrix}, \tag{90}$$

$$\omega_j^{(\alpha)} = \frac{(-1)^j \Gamma(\alpha+1)}{\Gamma(\alpha/2-j+1)\Gamma(\alpha/2+j+1)},\ j = 0, 1, \ldots, M.$$

While scheme (89) is second order in space, a fourth-order compact scheme is developed by Ding et al. in [18]:

$$\begin{aligned} \frac{\partial^\alpha v(x,\ t)}{\partial |x|^\alpha} &= \frac{1}{h^\alpha}\left[\frac{\alpha}{24}\Delta_h^\alpha v(x-h,\ t) - (1+\frac{\alpha}{12})\Delta_h^\alpha v(x,\ t) + \frac{\alpha}{24}\Delta_h^\alpha v(x+h,\ t)\right] + \mathcal{O}(h^4) \\ &= -\frac{1}{h^\alpha}\left(1 - \frac{\alpha}{24}\delta_x^2\right)\Delta_h^\alpha v(x,\ t) + \mathcal{O}(h^4) \\ &= -\frac{1}{h^\alpha}\left(1 + \frac{\alpha}{24}\delta_x^2\right)^{-1}\Delta_h^\alpha v(x,\ t) + \mathcal{O}(h^4), \end{aligned} \tag{91}$$

where $\delta_x^2 v(x,\ t) = v(x-h,\ t) - 2v(x,\ t) + v(x+h,\ t)$, and where $-\frac{\Delta_h^\alpha v(x,\ t)}{h^\alpha}$ is the second-order fractional centered difference approximation (89) to the Riesz derivative in space. The convergence rate of scheme (91) in space has been proved to be fourth order in Theorem 11 in [18].

We use the Neumann boundary conditions from [36], where the elements of matrix

$H_M^{(\alpha)}$ are given as:

$$\omega_{i,j}^{(\alpha)} = \begin{cases} 2g_1^{(\alpha)}, \quad 1 \le i = j \le M-1; \\ g_2^{(\alpha)} + g_0^{(\alpha)}, \quad j = i-1,\ 2 \le i \le M-1; \\ g_2^{(\alpha)} + g_0^{(\alpha)}, \quad j = i+1,\ 2 \le i \le M-1; \\ g_{i-j+1}^{(\alpha)}, \quad 1 \le j \le i-2,\ 3 \le i \le M-1; \\ g_{i-j+1}^{(\alpha)}, \quad 3 \le j \le M,\ 1 \le i \le M-2; \\ -g_{M-j}^{(\alpha-1)}, \quad 1 \le j \le M-1,\ i = M; \\ -2g_0^{(\alpha-1)}, \quad i = j = M, \end{cases}$$

where $g_k^{(\alpha)} = (-1)^k \binom{\alpha}{k}$.

4.3 Time integrators for the FCNLSE

4.3.1 Linearly implicit method

A second-order linearly implicit conservative scheme is described in [63] with the second-order fractional centered difference approximation (89) in space. It is convenient to apply this linearly implicit method with the fourth-order compact scheme (91) in space:

$$\begin{aligned} i\,\frac{u_j^{n+1}-u_j^n}{\tau} - \frac{\gamma}{h^\alpha}\left(1+\frac{\alpha}{24}\delta_x^2\right)^{-1}\Delta_h^\alpha u_j^{n+\frac{1}{2}} + \rho(|u_j^{n+\frac{1}{2}}|^2 + \beta|v_j^{n+\frac{1}{2}}|^2)u_j^{n+\frac{1}{2}} = 0, \\ i\,\frac{v_j^{n+1}-v_j^n}{\tau} - \frac{\gamma}{h^\alpha}\left(1+\frac{\alpha}{24}\delta_x^2\right)^{-1}\Delta_h^\alpha v_j^{n+\frac{1}{2}} + \rho(|v_j^{n+\frac{1}{2}}|^2 + \beta|u_j^{n+\frac{1}{2}}|^2)v_j^{n+\frac{1}{2}} = 0, \end{aligned} \tag{92}$$

where $u_j^{n+\frac{1}{2}} = (u_j^n + u_j^{n+1})/2$ and $v_j^{n+\frac{1}{2}} = (v_j^n + v_j^{n+1})/2$. The first time step is computed with a second-order iterative time integrator.

4.3.2 The ETDRK4 scheme

As described in Chapter 3, the ETDRK4 scheme (61) was constructed to solve the equation of the form

$$u_t = \mathcal{L}u + \mathcal{F}(u,t), \tag{93}$$

where $\mathcal{L}$ is a linear operator and $\mathcal{F}$ is nonlinear. After being discretized in space, equation (93) can be written as a system of ODEs of the form

$$u_t + Au = F(u,t). \tag{94}$$

Considering the fourth-order compact scheme (91) applied to a single FNLSE in the system (77), matrix $A = -i\gamma(I + \frac{\alpha}{24}D)^{-1}H_M^{(\alpha)}$, where $H_M^{(\alpha)}$ is given in Eq. (90), I is the identity matrix, and D is the matrix corresponding to the second-order central difference approximation. $F(u,t)$ is the nonlinear term which will be treated explicitly in the ETDRK4 scheme.

Algorithm (61) uses implicit solvers with the same coefficient matrices that make it highly efficient for this system of nonlinear PDEs. For the FCNLSEs, matrix $A = -i\gamma(I + \frac{\alpha}{24}D)^{-1}H_M^{(\alpha)}$ is a fully dense matrix, which means the computation of exponential terms in the ETD schemes [11] are time consuming. The algorithm (61) increases the computational efficiency by reducing the number of matrix multiplication and avoiding the computation of matrix exponential functions. The explicit treatment of the nonlinear terms decouples the FCNLSE while the scheme remains fourth-order convergent in time. The compact ETDRK4 scheme is novel and attractive for the FCNLSEs in the sense that only second-order schemes in time [63] have been applied to the FCNLSEs thus far.

4.4 Stability analysis

The stability of the ETDRK4 scheme (61) can be analyzed by plotting its stability regions as we did in Section 3.5. A similar idea is shown in [22], where the generalized ETD methods are used for fractional order problems.

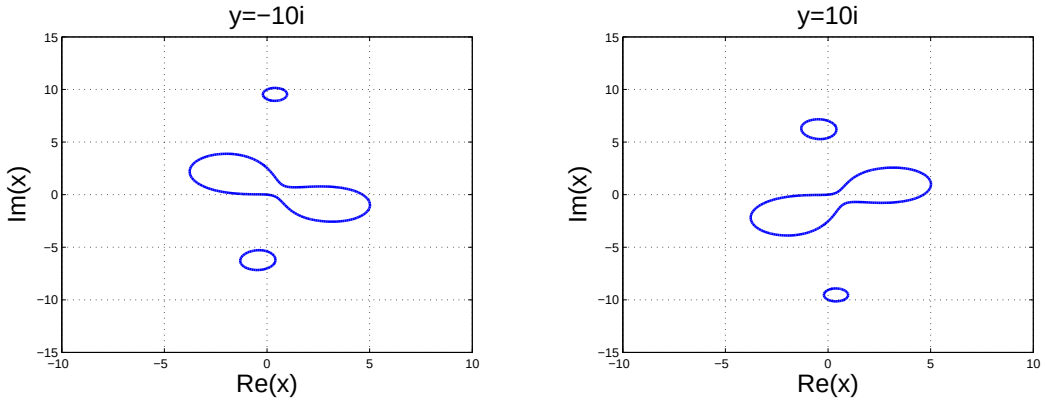

Figure 15: Stability regions for $y = -10i$ (left) and $y = 10i$ (right).

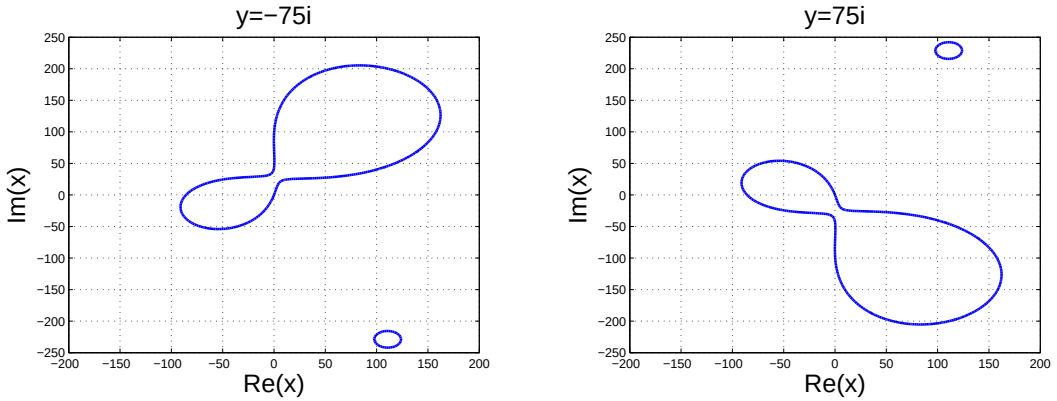

Figure 16: Stability regions for $y = -75i$ (left) and $y = 75i$ (right).

The stability regions for solving the FNLSEs are shown in Figs. 15 and 16, where we plot the real and imaginary part of x for the cases of $y = -10i$, $10i$, $-75i$, and $75i$. It has been proven in Theorem 8 in [18] that matrix $(I + \frac{\alpha}{24}D)^{-1}H_M^{(\alpha)}$ is positive

definite, which indicates that matrix $A = -i\gamma(I + \frac{\alpha}{24}D)^{-1}H_M^{(\alpha)}$ has eigenvalues of the form $-a \cdot i$, where a is some real number.

4.5 Numerical experiments

4.5.1 A single FNLSE

As shown in [63], when $\beta = 0$, then the system (77) is decoupled and becomes

$$i\, u_t - \gamma\, (-\Delta)^{\alpha/2} u + \rho|u|^2 u = 0, \tag{95}$$

subject to the initial condition

$$u(x,\ 0) = \mathrm{sech}(x) \cdot \exp(2ix), \tag{96}$$

and homogeneous Dirichlet boundary conditions on $x_L = -20$ and $x_R = 20$.

For this example, we set the parameters as $\gamma = 1,\ \rho = 2$. When $\alpha = 2$, the exact solution is given as

$$u(x,\ t) = \mathrm{sech}(x - 4t) \cdot \exp(i(2x - 3t)). \tag{97}$$

For Figs. 17 – 20, the ETDRK4 scheme (61) and the fourth-order spatial discretization (91) are used with $h = 0.05$ and $\tau = 0.005$ to solve Eq. (95) with different α values.

In Table 7, the L_2 error is computed as $e(h, \tau) = \|u - u_h\|_{L_2}$. The order of convergence in space is computed as

$$Order = \frac{log(e(h_n, \tau)/e(h_{n+1}, \tau))}{log(h_n/h_{n+1})}.$$

The time step τ is set to be a small value 0.0001, and the space mesh size h is reduced by half each time we compute the L_2 error. The orders of convergence of the numerical

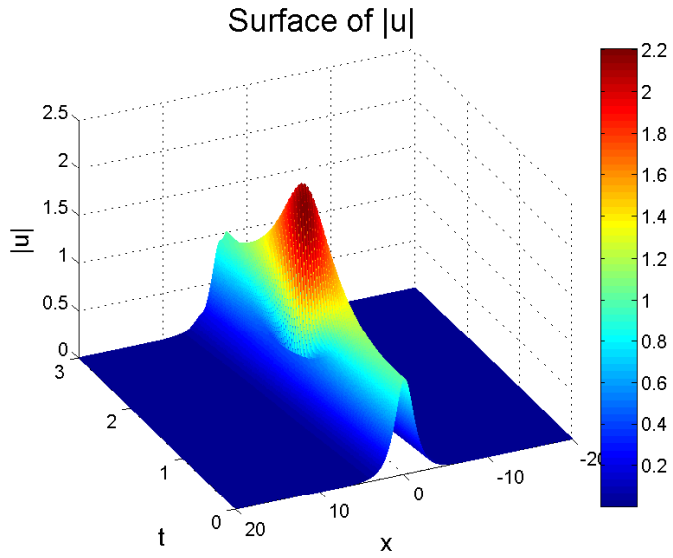

Figure 17: Numerical solution to Eq. (95) with $\alpha = 1.4$

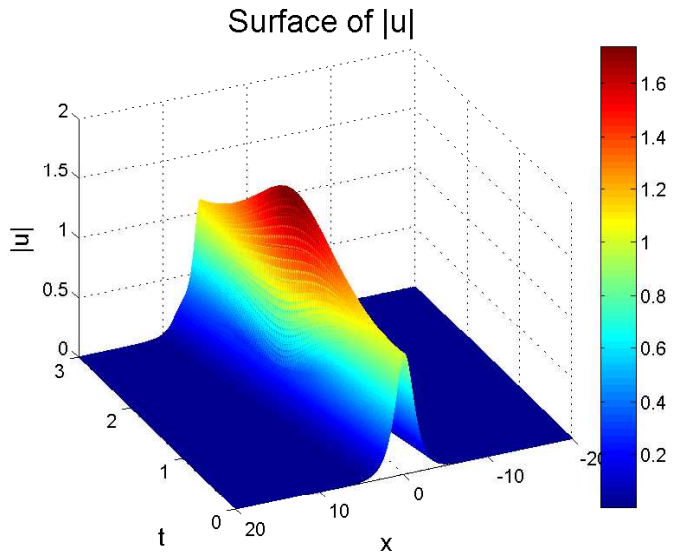

Figure 18: Numerical solution to Eq. (95) with $\alpha = 1.6$.

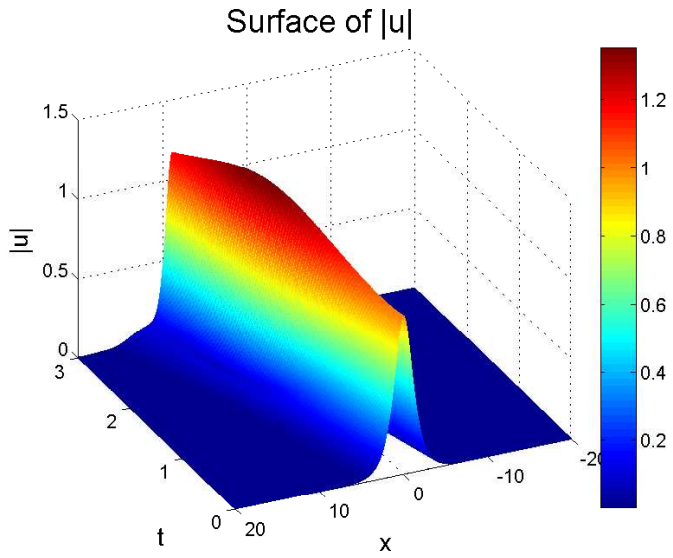

Figure 19: Numerical solution to Eq. (95) with $\alpha = 1.8$.

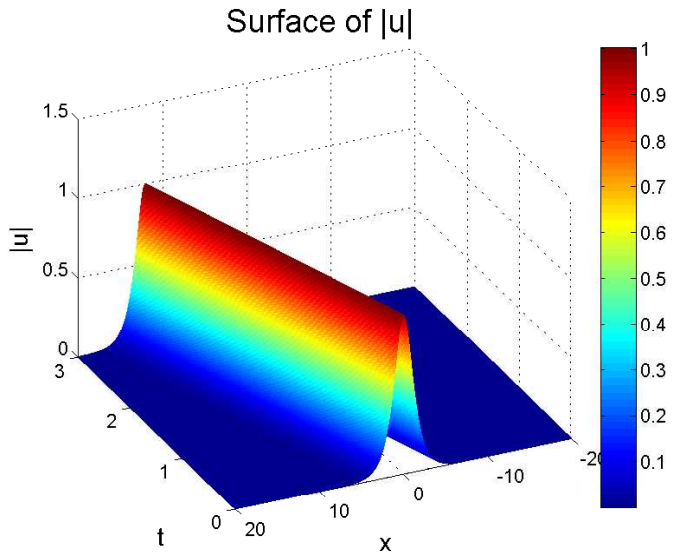

Figure 20: Numerical solution to Eq. (95) with $\alpha = 1.999$.

Table 7: Order of convergence in space solving (95) with $\tau = 0.0001$ and $\alpha = 2$.

h	L_2 error of scheme (90)	Order	L_2 error of scheme (91)	Order
0.4	1.33908	-	0.42178	-
0.2	0.33075	2.017	0.01978	4.414
0.1	0.05823	2.506	0.00125	3.984
0.05	0.01107	2.395	7.15e-05	4.128

results satisfy the analytic orders of convergence.

Table 8: Order of convergence in time solving (95) for different α values.

α	$\tau = 0.02$	$\tau = 0.01$	Order
1.4	0.18150	0.01327	3.775
1.6	0.22254	0.01691	3.718
1.8	0.33677	0.02286	3.881
1.99	0.35833	0.02656	3.754

Table 8 indicates how the ETDRK4 scheme (61) performs for different α values. The exact solution u is obtained by the linearly implicit method (92) with a very fine space mesh and a small time step ($h = 0.025$ and $\tau = 0.0001$). The order of convergence in time is computed as

$$Order = \frac{log(e(h, \tau_n)/e(h, \tau_{n+1}))}{log(\tau_n/\tau_{n+1})}.$$

The space mesh size h is set to be a small value of 0.025.

Fig. 21 indicates graphically that both the ETDRK4 scheme (61) and the fourth-order fractional compact scheme (91) have fourth-order convergence when solving Eq. (95) with $\alpha = 2$, where the exact solution exists. This can be seen by looking at the slopes of the regression lines in Fig. 21.

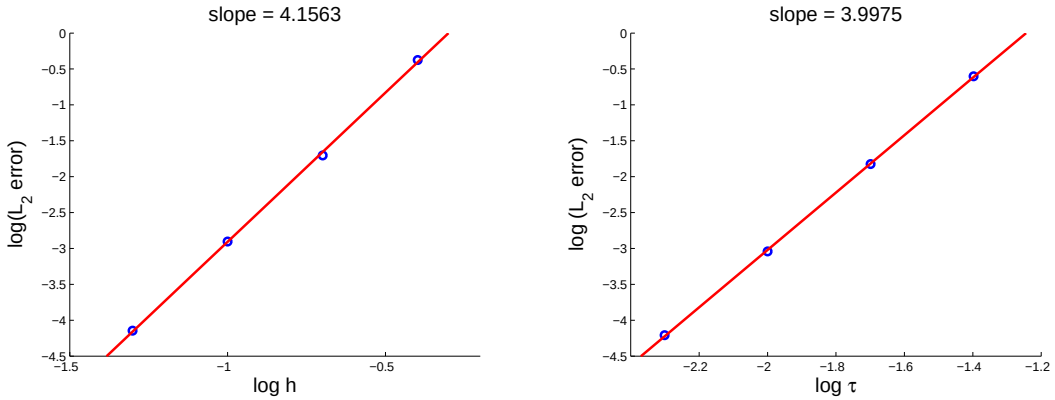

Figure 21: Orders of convergence in space (left) and time (right) using the ETDRK4 scheme (61) and the compact scheme (91).

Table 9: The errors of mass solving (95) by the ETDRK4 scheme with $h = 0.1$, $\tau = 0.01$.

α	$t = 1$	$t = 2$	$t = 3$	$t = 4$
1.4	1.007e-10	3.769e-07	3.896e-07	3.906e-07
1.7	1.470e-08	8.280e-08	8.275e-08	8.469e-08
1.9	9.790e-09	2.123e-08	2.298e-08	7.560e-09
2.0	1.532e-09	3.060e-09	4.581e-09	6.097e-09

In Table 9, the mass error is computed as $|(Q^{t_n} - Q^{t_0})/Q^{t_0}|$. Table 9 indicates the behavior of mass conservation using the ETDRK4 scheme for different α values.

Table 10: Comparison of CPU time (seconds) with $h = 0.1$, $\tau = 0.01$ and $T = 3$.

α	ETDRK4	Linearly implicit
1.4	0.952965	7.505991
1.8	0.959274	7.276130
1.99	0.959053	7.259525
2.0	0.988483	6.570149

In Table 10, we compare the time consumption of the ETDRK4 scheme and the linearly implicit method with the same mesh size and time step. It can be observed that the linearly implicit method consumes more CPU time, because it needs to invert matrices inside the time update loop, while the ETDRK4 scheme inverts matrices and stores the result outside the time update loop.

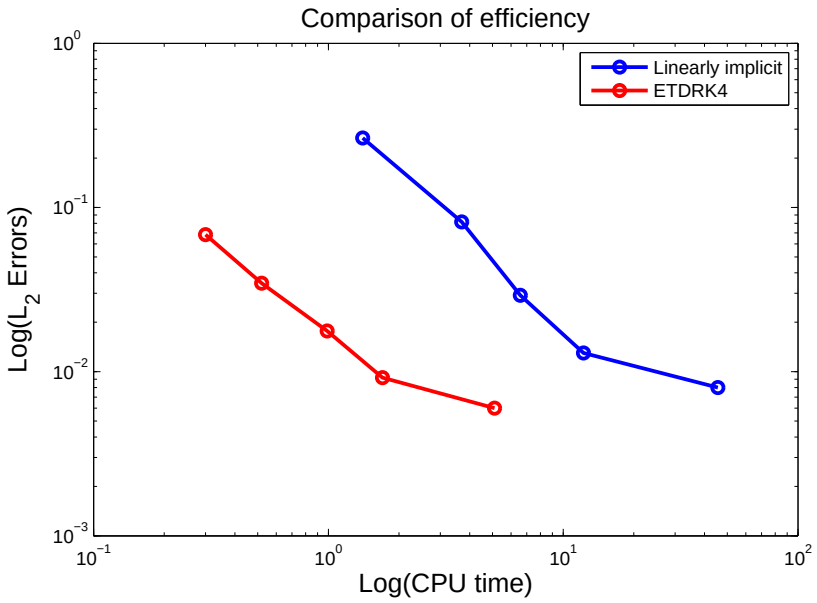

Figure 22: A comparison of L_2 errors vs CPU time.

In Fig. 22, we compare the efficiency of the ETDRK4 scheme with that of the linearly implicit method using the Log-Log plot of CPU time and L_2 errors. It can be seen from Fig. 22 that using the same CPU time, the ETDRK4 scheme gives a smaller error, which indicates better efficiency. The CPU times are based on computations via a Matlab R2014a platform based on an Intel Core i5-2410M 2.30GHz workstation.

4.5.2 Coupled FNLSEs

Consider the system of two equations with $\beta \neq 0$,

$$\begin{aligned} i\,u_t - \gamma\,(-\Delta)^{\alpha/2}u + \rho(|u|^2 + \beta|v|^2)u = 0, \\ i\,v_t - \gamma\,(-\Delta)^{\alpha/2}v + \rho(|v|^2 + \beta|u|^2)v = 0, \end{aligned} \tag{98}$$

with the initial conditions taken as

$$\begin{aligned} u(x,\ 0) = \mathrm{sech}(x + D_0)\cdot\exp(iV_0x), \\ v(x,\ 0) = \mathrm{sech}(x - D_0)\cdot\exp(-iV_0x), \end{aligned} \tag{99}$$

and homogeneous Dirichlet boundary conditions on $x_L = -20$ and $x_R = 20$. For this example, we set the parameters as $D_0 = 5,\ V_0 = 3, \gamma = 1,\ \rho = 2$.

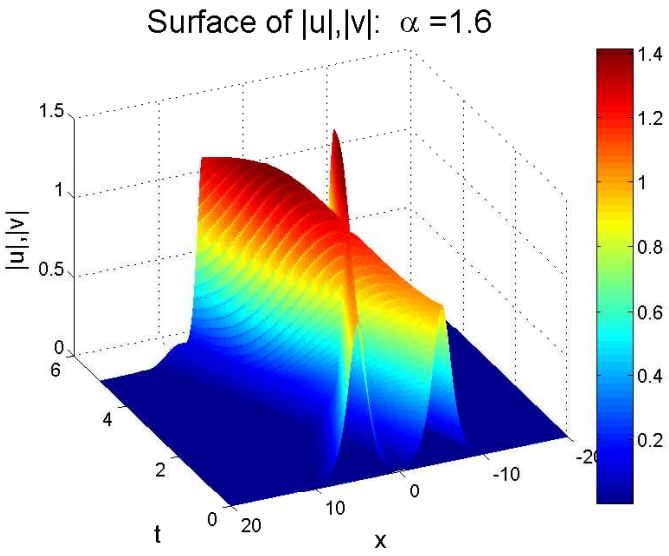

Figure 23: Numerical solution to Eq. (98) with $\alpha = 1.6$, $\beta = 1$

For Figs. 23 – 25, the results of the ETDRK4 scheme (61) and the fourth-order compact spatial discretization (91) are shown when $h = 0.05$ and $\tau = 0.005$ are used to solve Eq. (98) with different α and β values on $t \in (0,\ 5]$.

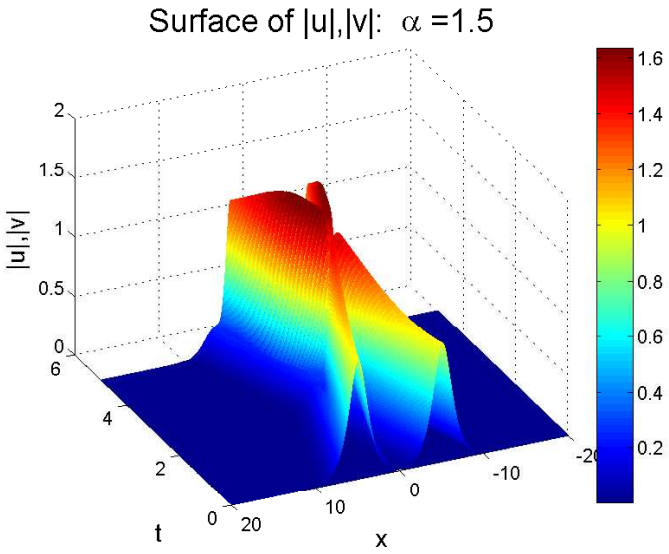

Figure 24: Numerical solution to Eq. (98) with $\alpha = 1.5$, $\beta = 2$.

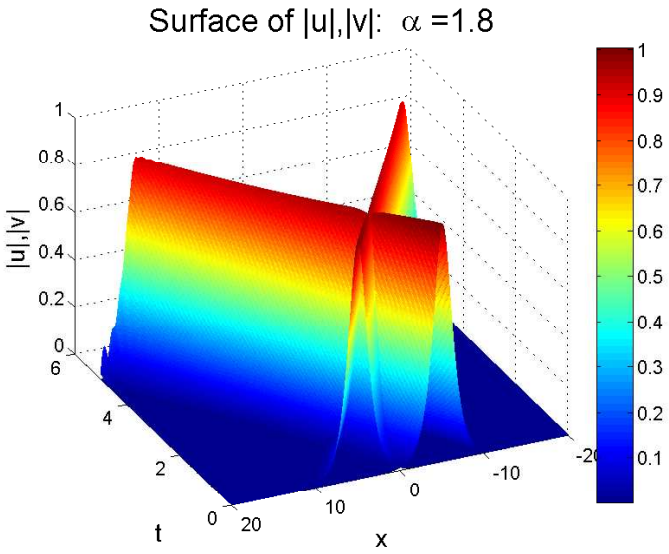

Figure 25: Numerical solution to Eq. (98) with $\alpha = 1.8$, $\beta = 2$.

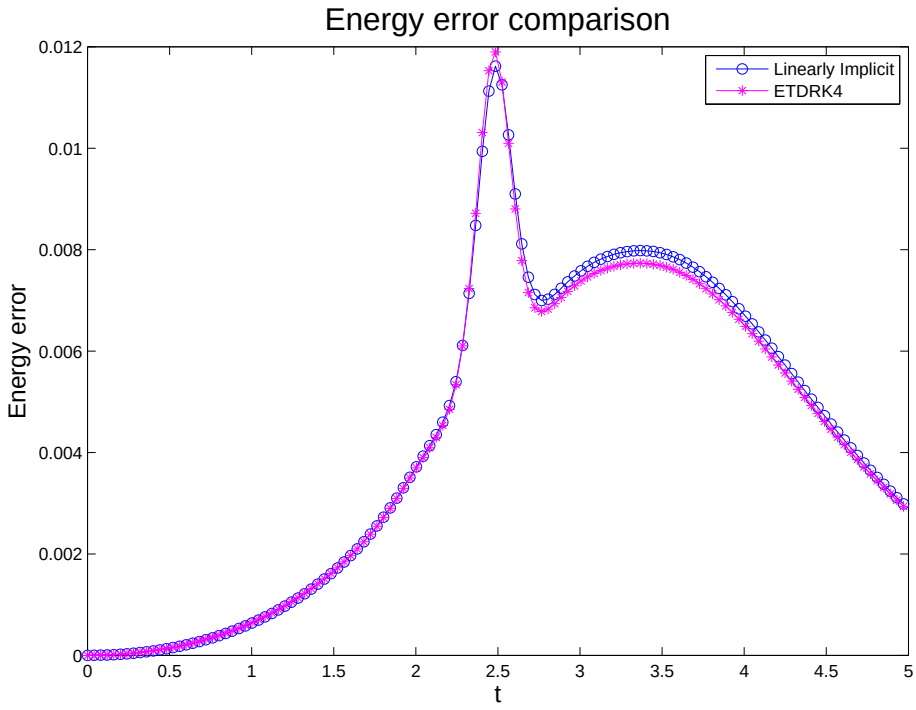

Figure 26: The errors of discrete energy $|(E^n - E^0)/E^0|$ comparison of the time integrators.

Fig. 26 gives a comparison of energy errors of numerical results using the ETDRK4 scheme (61) and the linearly implicit method (92). It can be seen that both time integrators for this problem have similar conservation of energy.

4.5.3 A system of four FNLSEs

We can extend the FCNLSE to a system of four equations with $\beta \neq 0$:

$$\begin{aligned}
i\,u_t - \gamma\,(-\Delta)^{\alpha/2}u + \rho(|u|^2 + \beta(|v|^2 + |w|^2 + |z|^2))u = 0,\\
i\,v_t - \gamma\,(-\Delta)^{\alpha/2}v + \rho(|v|^2 + \beta(|u|^2 + |w|^2 + |z|^2))v = 0,\\
i\,w_t - \gamma\,(-\Delta)^{\alpha/2}w + \rho(|w|^2 + \beta(|u|^2 + |v|^2 + |z|^2))w = 0,\\
i\,z_t - \gamma\,(-\Delta)^{\alpha/2}z + \rho(|z|^2 + \beta(|u|^2 + |v|^2 + |w|^2))z = 0,
\end{aligned} \tag{100}$$

with the initial conditions taken as

$$\begin{aligned}
u(x,\ 0) = \mathrm{sech}(x + D_0)\cdot\exp(iV_0x),\\
v(x,\ 0) = \mathrm{sech}(x - D_0)\cdot\exp(-iV_0x),\\
w(x,\ 0) = \mathrm{sech}(x + D_1)\cdot\exp(iV_1x),\\
z(x,\ 0) = \mathrm{sech}(x - D_1)\cdot\exp(-iV_1x),
\end{aligned} \tag{101}$$

and homogeneous Dirichlet boundary conditions on $x_L = -20$ and $x_R = 20$. In this example, we set the parameters as $D_0 = 10,\ D_1 = 3,\ V_0 = 5,\ V_1 = 2,\ \gamma = 1,\ \rho = 1$.

Fig. 27 gives the surface plot of the numerical solution using the ETDRK4 scheme (61) and the fourth-order spatial discretization (91) with $h = 0.05$ and $\tau = 0.005$. To better illustrate the solution to the system of four equations, we give the plot of solutions at $t = 0,\ 2.5,\ 5$ in Figs. 28 – 30. From the 2D plots, we observe clearly how the four waves travel and interact with each other. Fig. 31 indicates how the numerical methods conserve mass for the system of four equations. Fig. 32 gives the

trace of discrete energy errors computed by $|(E^0 - E^0)/E^0|$, where

$$E(t) = \frac{\gamma}{2}\int_R \left(\bar{u}(-\Delta)^{\frac{\alpha}{2}}u + \bar{v}(-\Delta)^{\frac{\alpha}{2}}v + \bar{w}(-\Delta)^{\frac{\alpha}{2}}w + \bar{z}(-\Delta)^{\frac{\alpha}{2}}z\right)dx$$
$$-\frac{\rho}{4}\int_R \left(|u|^4 + |v|^4 + |w|^4 + |z|^4 + 2\beta|u|^2|v|^2 + 2\beta|w|^2|z|^2\right)dx.$$

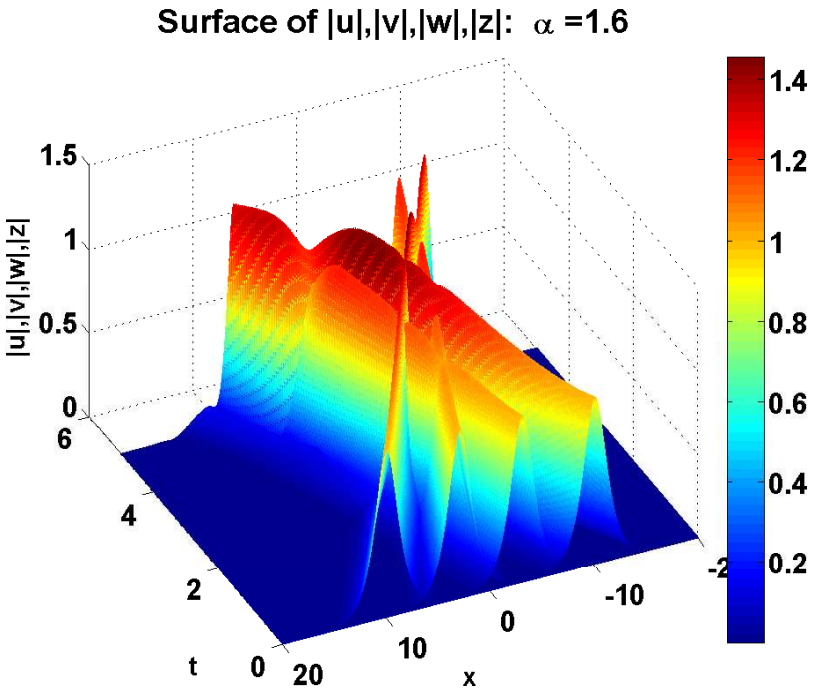

Figure 27: Numerical solution to Eq. (100) with $\alpha = 1.6$, $\beta = 2$.

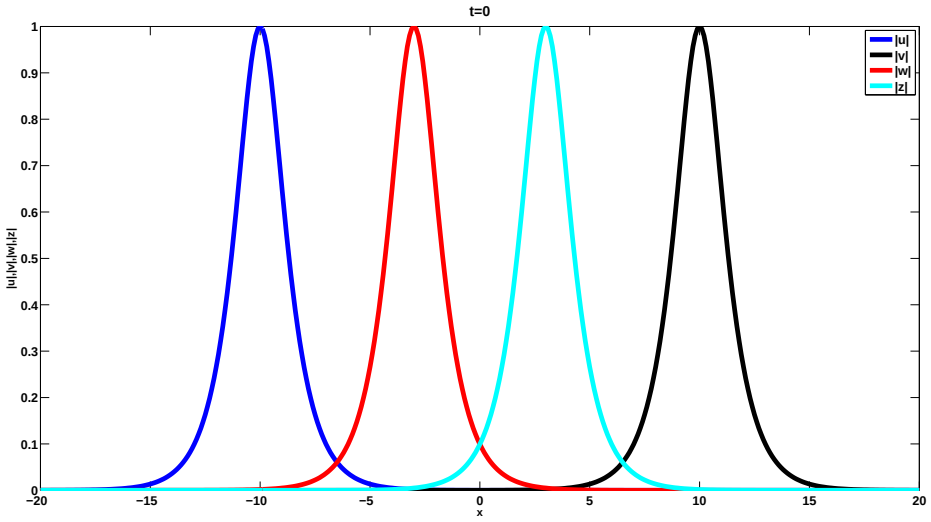

Figure 28: Initial condition of Eq. (98) at $t = 0$ with $\alpha = 1.6$, $\beta = 2$.

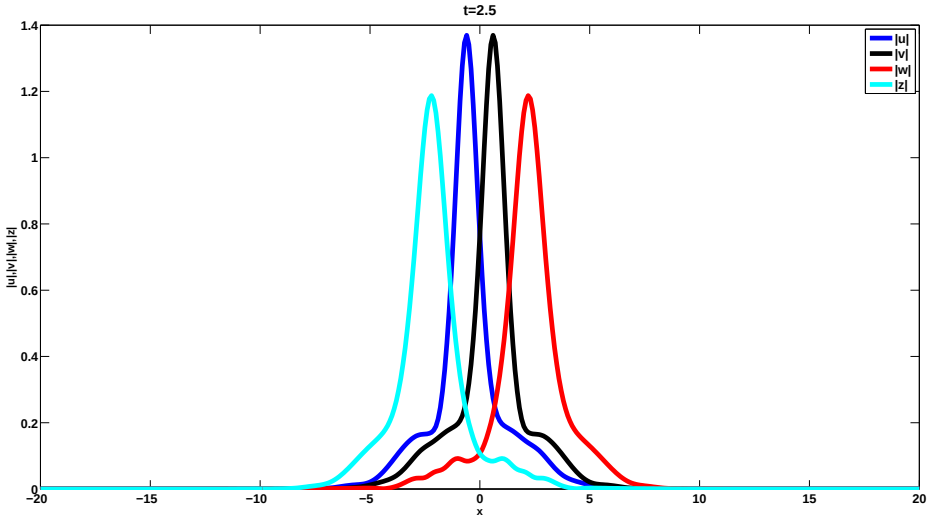

Figure 29: Numerical solution to Eq. (98) at $t = 2.5$ with $\alpha = 1.6$, $\beta = 2$.

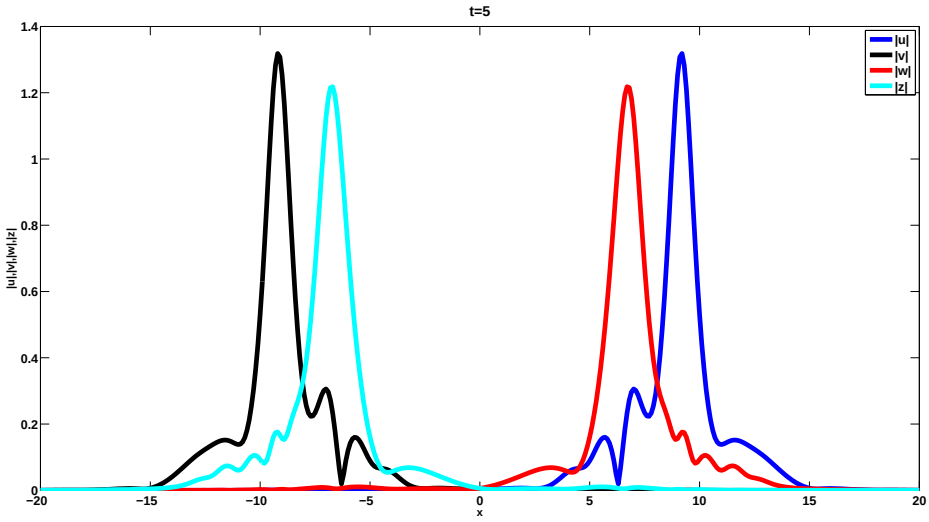

Figure 30: Numerical solution to Eq. (98) at $t = 5$ with $\alpha = 1.6$, $\beta = 2$.

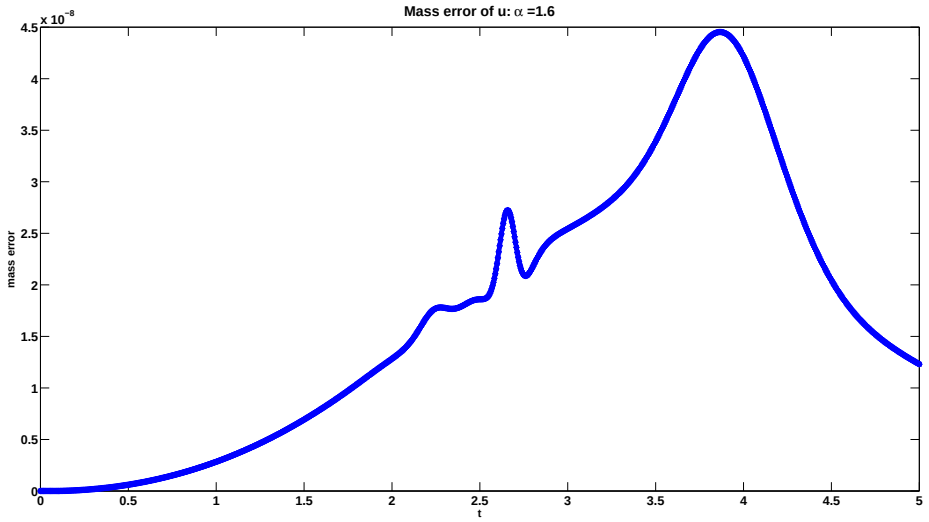

Figure 31: Trace of discrete mass errors.

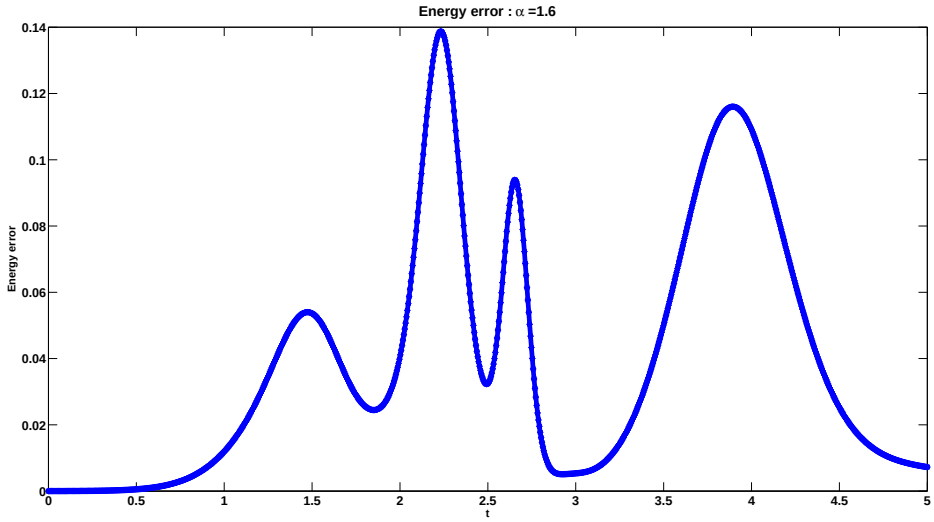

Figure 32: Trace of discrete energy errors.

CHAPTER 5

THE LOCALLY EXTRAPOLATED EXPONENTIAL OPERATOR SPLITTING SCHEME FOR MULTI-DIMENSIONAL FNLSES

5.1 Introduction

Recently, numerical solutions of the FNLSEs are being discussed more and more. The Crank-Nicolson (CN) scheme is used for time discretization in [4]. A compact ADI scheme is used to solve the two-dimensional FNLSE in [72]. We adopt a locally extrapolated exponential operator splitting (LE-EOS) scheme to achieve second-order convergence in both space and time. The numerical method we use can be conveniently applied to systems of two-dimensional and three-dimensional PDEs. The method is more widely applicable than the ADI scheme in [72] in the sense that it treats the nonlinear terms explicitly, which makes the large systems solvable, and it is not limited to the dimensions in space.

In this chapter, the two-dimensional space fractional coupled nonlinear Schrödinger equations (FCNLSEs) involving the Riesz fractional derivatives are considered:

$$\begin{aligned} iu_t + \gamma(\frac{\partial^{\alpha_1}}{\partial|x|^{\alpha_1}} + \frac{\partial^{\alpha_2}}{\partial|y|^{\alpha_2}})u + \rho(|u|^2 + \beta|v|^2)u = 0, \quad (x,y) \in \mathbb{R}^2, \quad 0 < t \leq T \\ iv_t + \gamma(\frac{\partial^{\alpha_1}}{\partial|x|^{\alpha_1}} + \frac{\partial^{\alpha_2}}{\partial|y|^{\alpha_2}})v + \rho(|v|^2 + \beta|u|^2)v = 0, \quad (x,y) \in \mathbb{R}^2, \quad 0 < t \leq T \end{aligned} \tag{102}$$

with the initial conditions

$$\begin{aligned} u(x,y,0) = u_0(x,y), \\ v(x,y,0) = v_0(x,y), \end{aligned} \tag{103}$$

and homogeneous Dirichlet boundary conditions on $\partial\Omega$, where $i = \sqrt{-1}$, and the

parameters γ, ρ and β are some real constants. Eq. (102) can be used to model optical solitons, whose propagation is governed by fractional quantum mechanics.

We also consider the three-dimensional FNLSE

$$\begin{aligned} iu_t + \gamma(\frac{\partial^{\alpha_1}}{\partial|x|^{\alpha_1}} + \frac{\partial^{\alpha_2}}{\partial|y|^{\alpha_2}})u + \eta\frac{\partial^{\alpha_3}}{\partial|z|^{\alpha_3}}u + f(u) = 0,\ (x,y,z) \in \mathbb{R}^3,\ t \in (0,\ T], \\ u(x,y,z,t) = 0,\ (x,y,z) \in \partial\Omega,\ t \in [0,\ T], \\ u(x,y,z,0) = u_0(x,y,z),\ (x,y,z) \in \Omega \cup \partial\Omega, \end{aligned} \tag{104}$$

Eq. (104) is derived from a modification of the three-dimensional Gross-Pitaevskii equation [51], which is a special case of the FNLSE used to model solitons in a graded-index multi-mode fiber. In fiber optics, a multi-mode fiber has a larger core size than a single-mode fiber. A graded-index fiber has a refractive index that decreases while the core size increases. Solitons in graded-index (GRIN) fibres can improve data transmission rates to ensure low-cost in telecommunications [53].

5.2 Numerical methods

5.2.1 The exponential operator splitting scheme

Consider the three-dimensional FNLSE:

$$iu_t + \gamma(\frac{\partial^{\alpha_1}}{\partial|x|^{\alpha_1}} + \frac{\partial^{\alpha_2}}{\partial|y|^{\alpha_2}})u + \eta\frac{\partial^{\alpha_3}}{\partial|z|^{\alpha_3}}u + f(u) = 0, \quad (x,y,z) \in \mathbb{R}^3. \tag{105}$$

We multiply the equation by $-i$ and have

$$u_t - i\gamma(\frac{\partial^{\alpha_1}}{\partial|x|^{\alpha_1}} + \frac{\partial^{\alpha_2}}{\partial|y|^{\alpha_2}})u - i\eta\frac{\partial^{\alpha_3}}{\partial|z|^{\alpha_3}}u - if(u) = 0. \tag{106}$$

To solve Eq. (106) we apply the matrix approximation in space as

$$\mathrm{U}_t + A\mathrm{U} = \mathcal{F}(\mathrm{U}), \tag{107}$$

where U is the vector containing the approximation to u, AU approximates the space fractional derivatives, and $\mathcal{F}(\mathrm{U})$ approximates the nonlinear part $f(u)$.

The exponential operator splitting is achieved by decomposing matrix A into three block matrices containing the components in x, y, z directions, such that $A = A_{x,M^3} + A_{y,M^3} + A_{z,M^3}$, where A_{x,M^3}, A_{y,M^3} and A_{z,M^3} are block-diagonal matrices of order M^3, where the diagonal blocks A_{x,M^2}, A_{y,M^2} and A_{z,M^2} are block-diagonal matrices of order M^2, whose composing blocks are $A_x^{\alpha_1}$, $A_y^{\alpha_2}$ and $A_z^{\alpha_3}$ respectively. As described in Chapter 4, the fractional centered difference approximation operators $A_x^{\alpha_1}$, $A_y^{\alpha_2}$ and $A_z^{\alpha_3}$ are defined as

$$\begin{aligned} A_x^{\alpha_1} &= -i\gamma H_M^{(\alpha_1)}, \\ A_y^{\alpha_2} &= -i\gamma H_M^{(\alpha_2)}, \\ A_z^{\alpha_3} &= -i\eta H_M^{(\alpha_3)}, \end{aligned} \tag{108}$$

where $H_M^{(\alpha_1)}$, $H_M^{(\alpha_2)}$, $H_M^{(\alpha_3)}$ are derived from (90).

To integrate (107) in time, we write the solution at t^{n+1} as

$$\mathrm{U}^{n+1} = \exp(-\tau(A_x^{\alpha_1} + A_y^{\alpha_2} + A_z^{\alpha_3}))(\mathrm{U}^n + \tau\mathcal{F}(\mathrm{U}^n)),$$

which can be approximated by

$$\mathrm{U}^{n+1} = \exp(-\tau A_z^{\alpha_3}) \exp(-\tau A_y^{\alpha_2}) \exp(-\tau A_x^{\alpha_1})(\mathrm{U}^n + \tau\mathcal{F}(\mathrm{U}^n)), \tag{109}$$

which incurs an error of $\mathcal{O}(\tau^2)$ [40, 54], since $A_x^{\alpha_1}$, $A_y^{\alpha_2}$ and $A_z^{\alpha_3}$ do not commute, in general.

If we use Padé (0,1) approximation to the exponential functions for the exponential terms, scheme (109) becomes:

$$\mathrm{U}^{n+1} = (I + \tau A_z^{\alpha_3})^{-1}(I + \tau A_y^{\alpha_2})^{-1}(I + \tau A_x^{\alpha_1})^{-1}(\mathrm{U}^n + \tau\mathcal{F}(\mathrm{U}^n)). \tag{110}$$

The exponential operator splitting (EOS) scheme can be formulated as the split form of scheme (110)

$$\begin{aligned} \mathrm{U}^{*} &= (I + \tau A_x^{\alpha_1})^{-1}(\mathrm{U}^{n} + \tau \mathcal{F}(\mathrm{U}^{n})), \\ \mathrm{U}^{**} &= (I + \tau A_y^{\alpha_2})^{-1}\mathrm{U}^{*}, \\ \mathrm{U}^{n+1} &= (I + \tau A_z^{\alpha_3})^{-1}\mathrm{U}^{**}. \end{aligned} \tag{111}$$

The EOS scheme (111) is first-order convergent in time (see also [40, 62]). For the two-dimensional problem, we use a similar technique with one intermediate vector and operators in the x and y directions.

5.2.2 The locally extrapolated exponential operator splitting scheme

It is shown in [44] that the EOS scheme (111) can be locally extrapolated to achieve second-order accuracy with the following procedure.

Firstly, we write scheme (111) over two single time steps:

$$\begin{aligned} \mathrm{U}^{*} &= (I + \tau A_x^{\alpha_1})^{-1}(\mathrm{U}^{n} + \tau \mathcal{F}(\mathrm{U}^{n})), \\ \mathrm{U}^{**} &= (I + \tau A_y^{\alpha_2})^{-1}\mathrm{U}^{*}, \\ \mathrm{U}^{n+1} &= (I + \tau A_z^{\alpha_3})^{-1}\mathrm{U}^{**}. \\ \mathrm{U}^{\sharp} &= (I + \tau A_z^{\alpha_3})^{-1}(\mathrm{U}^{n+1} + \tau \mathcal{F}(\mathrm{U}^{n+1})), \\ \mathrm{U}^{\sharp\sharp} &= (I + \tau A_y^{\alpha_2})^{-1}\mathrm{U}^{\sharp}, \\ \mathrm{U}^{n+2} &= (I + \tau A_x^{\alpha_1})^{-1}\mathrm{U}^{\sharp\sharp}, \end{aligned} \tag{112}$$

and we represent the solution U^{n+2} from (112) as $\mathrm{U}^{(0)}$.

Secondly, we compute scheme (111) over a double time step 2τ:

$$\begin{aligned} \mathrm{U}^{*} &= (I + 2\tau A_x^{\alpha_1})^{-1}(\mathrm{U}^{n} + 2\tau \mathcal{F}(\mathrm{U}^{n})), \\ \mathrm{U}^{**} &= (I + 2\tau A_y^{\alpha_2})^{-1}\mathrm{U}^{*}, \\ \mathrm{U}^{n+2} &= (I + 2\tau A_z^{\alpha_3})^{-1}\mathrm{U}^{**}, \end{aligned} \tag{113}$$

and we represent the solution U^{n+2} from (113) as $\mathrm{U}^{(1)}$.

Thirdly, we compute scheme (111) over a double time step 2τ again but in different directions:

$$\begin{aligned} \mathrm{U}^{*} &= (I + 2\tau A_z^{\alpha_3})^{-1}(\mathrm{U}^{n} + 2\tau \mathcal{F}(\mathrm{U}^{n})), \\ \mathrm{U}^{**} &= (I + 2\tau A_y^{\alpha_2})^{-1}\mathrm{U}^{*}, \\ \mathrm{U}^{n+2} &= (I + 2\tau A_x^{\alpha_1})^{-1}\mathrm{U}^{**}. \end{aligned} \tag{114}$$

and we represent the solution U^{n+2} from (114) as $\mathrm{U}^{(2)}$.

Finally, we write the local extrapolation of scheme (111) as:

$$\mathrm{U}^{n+2} = 2\mathrm{U}^{(0)} - \frac{1}{2}\left(\mathrm{U}^{(1)} + \mathrm{U}^{(2)}\right). \tag{115}$$

Since $(I + \tau A_x^{\alpha_1})^{-1}$ is a fully dense matrix of size $M \times M$, scheme (115) has a computational complexity of $O(M^2)$ per time step. Without splitting the operator, a matrix approximating the space derivatives has a computational cost of $O(M^6)$ per time step, an incredibly burdensome complexity by most standards. The locally extrapolated EOS scheme has been applied to multi-dimensional reaction-diffusion systems in [6] and achieves second-order convergence in time.

5.2.3 Stability regions

Using the same technique as shown in Section 2.7, we denote $x = \lambda\tau$ and $y = c\tau$, and apply scheme (115) to solve (22) in one spatial dimension. The amplification factor can be computed as

$$\frac{u^{n+2}}{u^n} = r(x,\ y) = c_0 + c_1 x + c_2 x^2, \tag{116}$$

where

$$\begin{aligned} c_0 &= 1 + 2y + 2y^2 + \mathcal{O}(y^3), \\ c_1 &= 2 + 4y + 4y^2 + \mathcal{O}(y^3), \\ c_2 &= 2 + 4y + 6y^2 + \mathcal{O}(y^3). \end{aligned} \tag{117}$$

To obtain stability regions, we assume that $r(x,\ y) < \exp(i\theta),\ \theta \in [0,\ 2\pi]$. For complex values of x, we fix y to various complex values and plot the stability regions in Fig. 33.

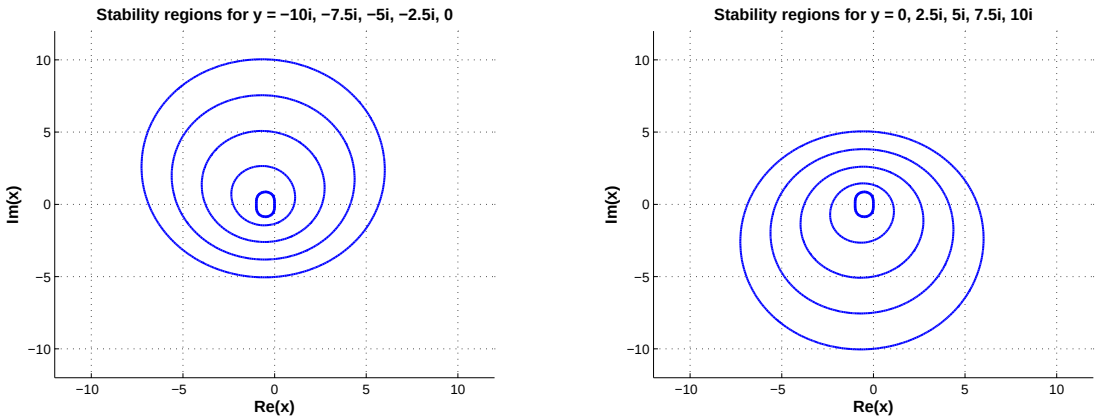

Figure 33: Stability regions of the EOS scheme with local extrapolation (115).

It can be seen from the stability regions in Fig. 33 that the innermost region corresponds to $y = 0$ and the stability region expands as $|y|$ increases from 0 to

10, which indicates the stability of the extrapolation (115). Since $H_M^{(\alpha)}$ in (90) is symmetric, its eigenvalues are real. $A_x^{\alpha_1}$, $A_y^{\alpha_2}$ and $A_z^{\alpha_3}$ have eigenvalues of the form $-i \cdot a$, where a is some real number. Therefore, y is chosen to be $-10i$, $-7.5i$, $-5i$, $-2.5i$, 0, $2.5i$, $5i$, $7.5i$, $10i$.

5.3 Numerical experiments

5.3.1 A two-dimensional FNLSE

We solve the following two-dimensional problem [72]

$$\begin{aligned} iu_t + \gamma(\partial_x^\alpha u + \partial_y^\beta u) + \rho|u|^2 u = 0, \quad (x,y) \in \Omega, \quad t \in (0,\ T], \\ u(x,y,t) = 0, \quad (x,y) \in \partial\Omega, \quad t \in [0,\ T], \\ u(x,y,0) = \operatorname{sech}(x)\operatorname{sech}(y)\exp(i(x+y)), \quad (x,y) \in \overline{\Omega} = \Omega \cup \partial\Omega, \end{aligned} \tag{118}$$

where $\Omega = [-10,\ 10]^2$, $\gamma = 1$, $\rho = 2$, and $T = 1$.

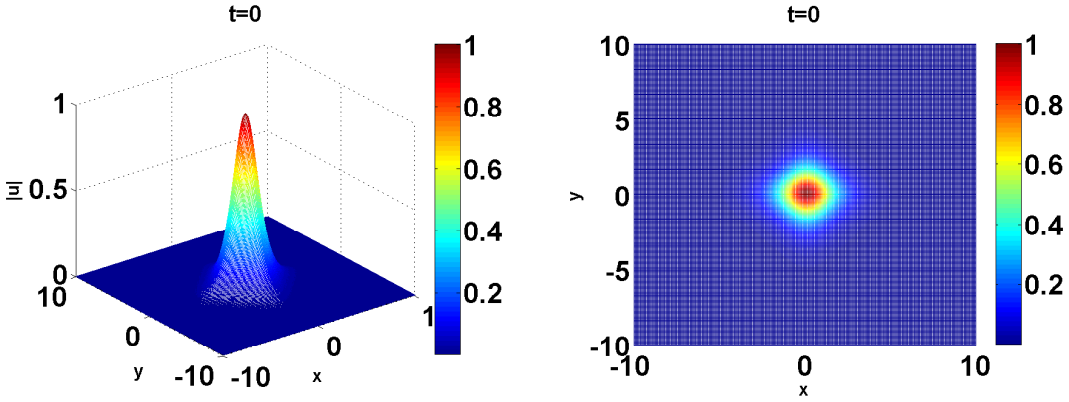

Figure 34: Initial condition of Eq. (118).

In this section, we use ∂_x^α to denote $\frac{\partial^\alpha}{\partial|x|^\alpha}$ for simplicity. Fig. 34 shows the initial condition of Eq. (118) from two different view points. We notice that the peak of

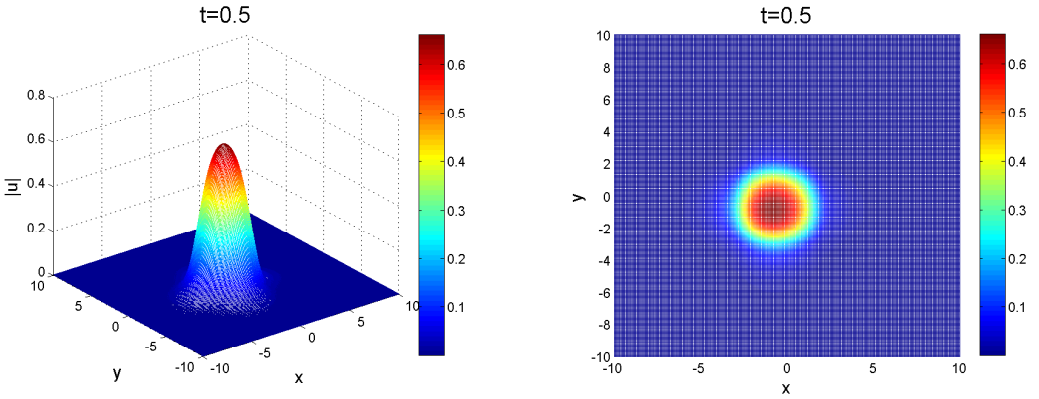

Figure 35: Solution to Eq. (118) with $\alpha = \beta = 1.8$ at $t = 0.5$.

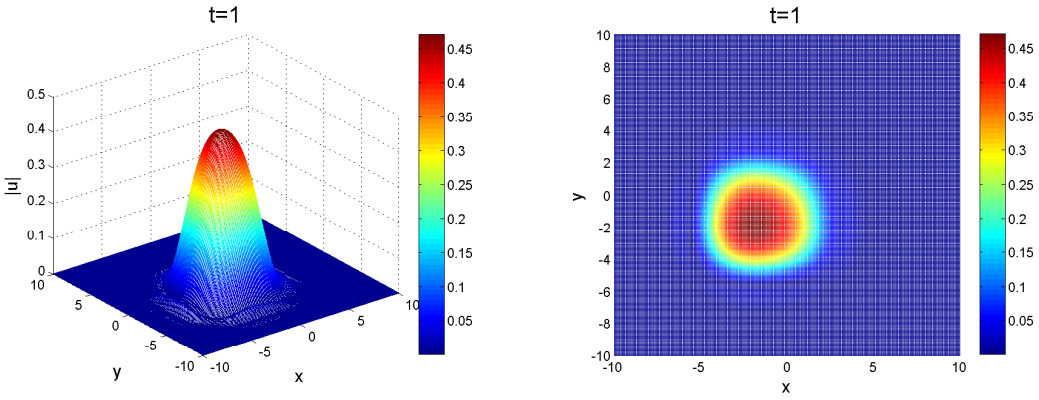

Figure 36: Solution to Eq. (118) with $\alpha = \beta = 1.8$ at $t = 1$.

the wave lies at the origin of the coordinate plane and the amplitude of the wave is 1. The numerical solutions of Eq. (118) at $t = 0.5$ and $t = 1$ are shown in Fig. 35 and Fig. 36, respectively. The results are achieved using the LE-EOS scheme (115), and the mesh steps used are $h = 0.05$ and $\tau = 0.01$. It can be seen that the wave is moving in the $(-x, -y)$ direction and the amplitude of the wave decreases as the wave defocuses.

Table 11 is obtained using the EOS scheme (111) for different α and β values. The order of convergence in time is computed using a very fine spatial mesh ($h = 0.05$).

Table 11: Order of convergence in time without local extrapolation.

	$(\alpha,\beta)=(1.2,1.2)$		$(\alpha,\beta)=(1.4,1.6)$		$(\alpha,\beta)=(1.8,1.8)$		
τ	$e(\tau)$	p	$e(\tau)$	p	$e(\tau)$	p	Avg. CPU
1/100	1.7285e-3	0.999	1.6338e-3	1.006	1.7926e-3	1.008	1.3839
1/200	8.6493e-4	1.020	8.1360e-4	1.005	8.9162e-4	1.028	2.6552
1/400	4.2657e-4	1.001	4.0523e-4	1.053	4.3726e-4	1.015	5.0132
1/800	2.1182e-4	−−	1.9532e-4	−−	2.1643e-4	−−	10.0620
1/1600	−−−−	−−	−−−−	−−	−−−−	−−	20.3490

Table 12: Order of convergence in time with local extrapolation.

	$(\alpha,\beta)=(1.2,1.2)$		$(\alpha,\beta)=(1.4,1.6)$		$(\alpha,\beta)=(1.8,1.8)$		
τ	$e(\tau)$	p	$e(\tau)$	p	$e(\tau)$	p	Avg. CPU
1/100	7.4388e-4	1.952	8.5339e-4	1.852	8.2256e-4	1.939	2.4601
1/200	1.9223e-4	1.976	2.3641e-4	1.985	2.1459e-4	1.944	4.9875
1/400	4.8872e-5	1.875	5.9003e-5	1.893	5.5772e-5	1.931	10.2160
1/800	1.3328e-5	−−	1.5883e-5	−−	1.4629e-5	−−	20.3865
1/1600	−−−−	−−	−−−−	−−	−−−−	−−	40.7285

The L_∞ error is computed as

$$e(\tau) = \|\mathrm{U}(\tau,h) - \mathrm{U}(\tau/2,h)\|_\infty.$$

The Order of convergence in time is computed as

$$p = \frac{log(e(\tau_n)/e(\tau_{n+1}))}{log(\tau_n/\tau_{n+1})}.$$

The spatial mesh size h is set sufficiently small to 0.05. It can be observed from Table 11 that the EOS scheme (111) is first order in time since the order of convergence p is around 1 for all the (α,β) chosen. Table 12 indicates that the the LE-EOS scheme (115) is second-order in time. The CPU times are based on computations via Matlab R2014a platforms based on an Intel Core i5-2410M 2.30GHz workstation.

5.3.2 A system of two-dimensional FNLSEs

We consider the following initial-boundary value problem:

$$\begin{aligned} i\,u_{1t} + \gamma\left(\partial_x^{\alpha} u_1 + \partial_y^{\beta} u_1\right) + \left(|u_1|^2 + \rho|u_2|^2\right) u_1 = 0, \\ i\,u_{2t} + \gamma\left(\partial_x^{\alpha} u_2 + \partial_y^{\beta} u_2\right) + \left(\rho|u_1|^2 + |u_2|^2\right) u_2 = 0, \end{aligned} \tag{119}$$

where $(x, y, t) \in \Omega_T = \Omega \times [0, T]$, with initial conditions:

$$\begin{aligned} u_1(x, y, 0) = B_1 \exp(-(x-d)^2 - y^2) \exp(-i \ln(\cosh(x^2 + y^2))), \\ u_2(x, y, 0) = B_2 \exp(-(x+d)^2 - y^2) \exp(-i \ln(\cosh(x^2 + y^2))), \end{aligned} \tag{120}$$

with $\gamma = 1,\ \rho = 2,\ d = 5,\ B_1 = 1,\ B_2 = 0.8$, and homogeneous Dirichlet boundary conditions on $\partial\Omega$.

Eq. (119) could model the interaction of two soliton in an optical fiber. The system of FNLSEs is derived from the system of NLSEs given in [34] Fig. 37 and

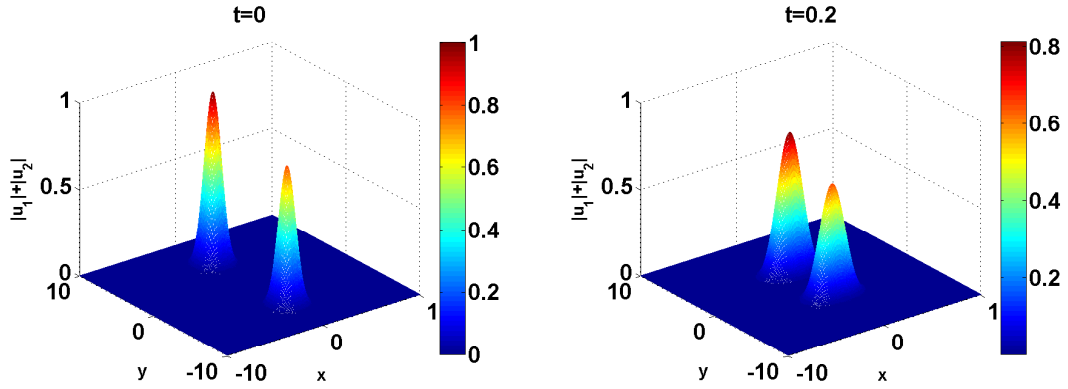

Figure 37: Solutions to Eq. (119) at $t = 0$ and $t = 0.2$.

38 are solutions to Eq. (119) with $\alpha = \beta = 1.8$. The results are achieved using the LE-EOS scheme (115) and the mesh sizes used are $h = 0.05$ and $\tau = 0.01$. It can be observed from the figures that the two waves move towards each other before they

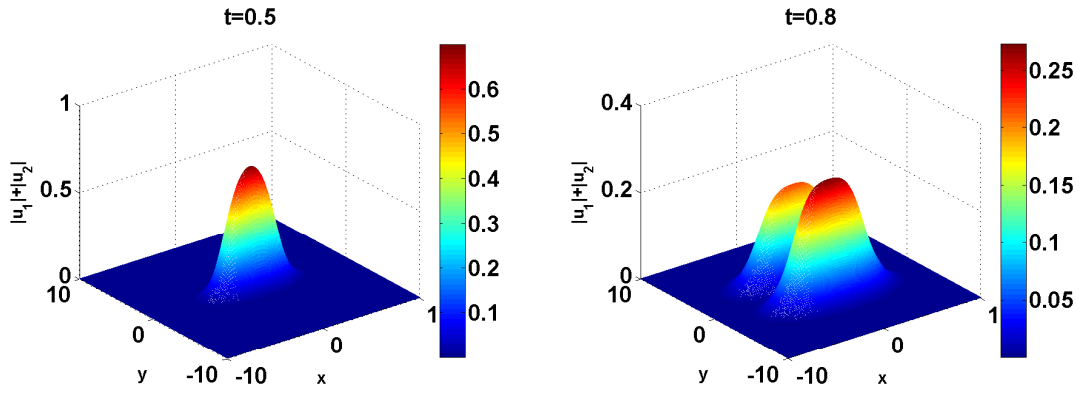

Figure 38: Solutions to Eq. (119) at $t = 0.5$ and $t = 0.8$.

interact and merge into one wave at $t = 0.5$. Then the two waves separate and move away from each other. Notice that during the movement, the waves defocus and the amplitudes decrease. The shape of the solitons differs slightly from the solution to the equation with $\alpha = \beta = 2$, which is given in [34].

5.3.3 A three-dimensional FNLSE

We consider the following three-dimensional problem

$$\begin{aligned} iu_t + \gamma(\partial_x^{\alpha_1} u + \partial_y^{\alpha_2} u + \partial_z^{\alpha_3} u) + \rho|u|^2 u = 0, \quad (x, y, z) \in \Omega, \quad t \in (0,\ T], \\ u(x, y, z, t) = 0, \quad (x, y, z) \in \partial\Omega, \quad t \in [0,\ T], \\ u(x, y, z, 0) = \operatorname{sech}(x)\operatorname{sech}(y)\operatorname{sech}(z)\exp(i(x + y + z)), \quad (x, y, z) \in \Omega \cup \partial\Omega, \end{aligned} \tag{121}$$

where $\Omega = [-10,\ 10]^3$, $\gamma = 1$, $\rho = 2$, and $T = 0.4$.

Fig. 39 demonstrates the initial condition of Eq. (121). Since the equation is three dimensional in space, the solution of $|u|$ on the left is represented using different colors on the color bar. To better illustrate the results, the solution of $|u|$ with $z = 0$ is shown on the right. Fig. 40 shows the solution of $|u|$ at $t = 0.4$. It can be seen from

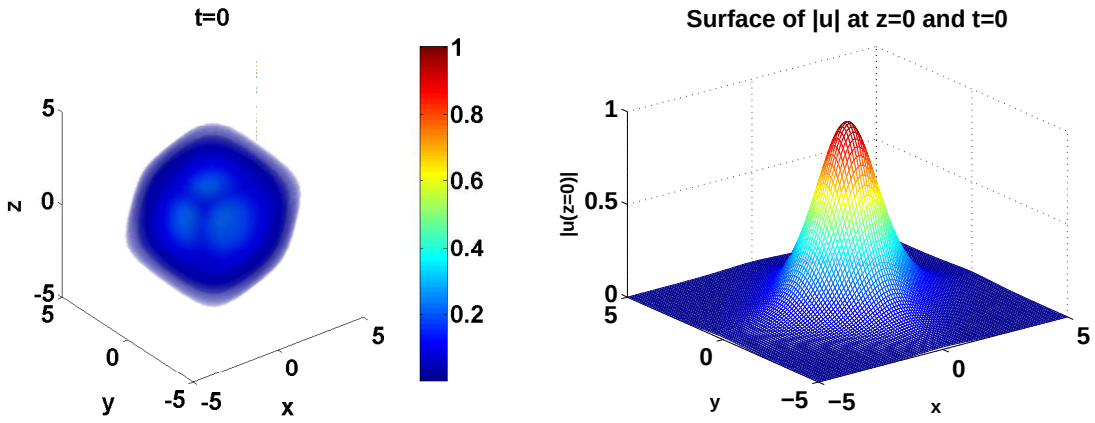

Figure 39: Initial condition of Eq. (121).

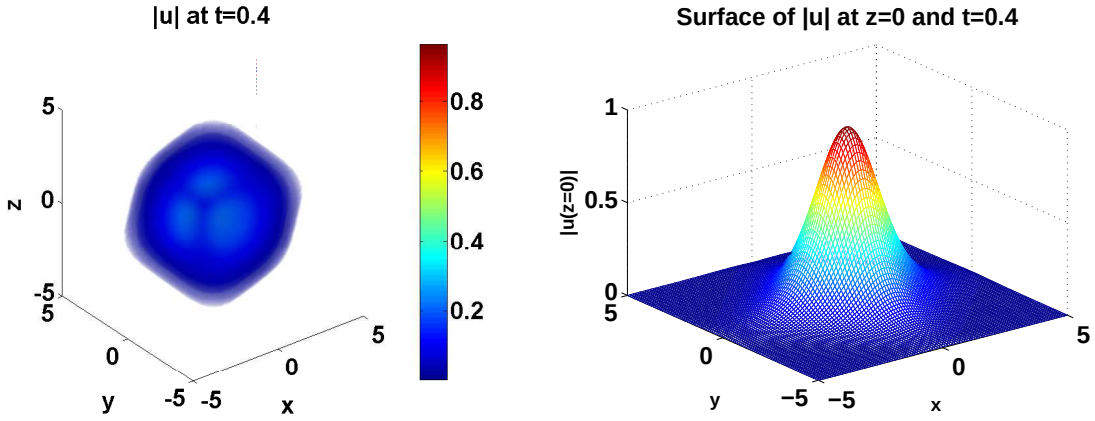

Figure 40: Solution to Eq. (121) with $\alpha_1 = 1.2,\ \alpha_2 = 1.5,\ \alpha_3 = 1.8$.

the figure that the amplitude at $t = 0.4$ is a little different from the initial condition.

Table 13 is obtained by the LE-EOS scheme (115). The spatial step is also chosen to be relatively small ($h = 0.05$). The results from Table 13 indicate that the LE-EOS scheme (115) is second-order in time, solving the three-dimensional problem.

Table 13: Order of convergence in time with local extrapolation.

	$\alpha_1 = \alpha_2 = \alpha_3 = 1.2$		$\alpha_1 = 1.2,\ \alpha_2 = 1.5,\ \alpha_3 = 1.8$		$\alpha_1 = \alpha_2 = \alpha_3 = 1.8$	
τ	$e(\tau)$	p	$e(\tau)$	p	$e(\tau)$	p
1/100	3.1256e-3	1.895	2.6483e-3	1.875	2.5659e-3	1.906
1/200	8.3722e-4	1.925	7.0365e-4	1.912	7.8231e-4	1.927
1/400	2.1802e-4	1.936	1.8933e-4	1.893	1.8716e-4	1.912
1/800	5.3671e-5	−−	4.9529e-5	−−	5.6502e-5	−−
1/1600	−−−−	−−	−−−−	−−	−−−−	−−

5.3.4 The Gross-Pitaevskii equation

A special form of three-dimensional NLSE, the Gross-Pitaevskii equation, can be utilized to model soliton propagation in a GRIN fiber [53]. We consider the Gross-Pitaevskii equation with space fractional derivatives:

$$u_t = \frac{i}{2k_0}(\partial_x^{\alpha_1} u + \partial_y^{\alpha_2} u) - i\frac{\beta}{2}\partial_z^{\alpha_3} u - ik_0(x^2+y^2)u + i\gamma|u|^2 u. \tag{122}$$

When $\alpha_1 = \alpha_2 = \alpha_3 = 2$, an approximate analytic solution exists [53]:

$$u(x,y,z,t) = A_0 \exp(i\frac{t}{\varsigma}) \exp(\frac{-(x^2+y^2)}{w_0^2} + i(\theta z^2 + \rho(x^2+y^2) + \phi)), \tag{123}$$

where ς is the pulse duration, w_0 is the beam width, θ and ρ are chirp parameters, and ϕ is an arbitrary phase. The parameters are chosen as $A_0 = k_0 = \beta = \gamma = 1$, $\varsigma = w_0 = \theta = \rho = 1$, $\phi = 0$. The initial condition generated from the analytic solution is:

$$u(x,y,z,0) = \exp(-(x^2+y^2) + i(z^2+x^2+y^2)), \tag{124}$$

Fig. 41 demonstrates the numerical results by the centered difference scheme (89) with the LE-EOS scheme (115) compared to the analytic solution (123). The mesh sizes are chosen as $h = 0.02,\ \tau = 0.001$. To better illustrate the differences, two

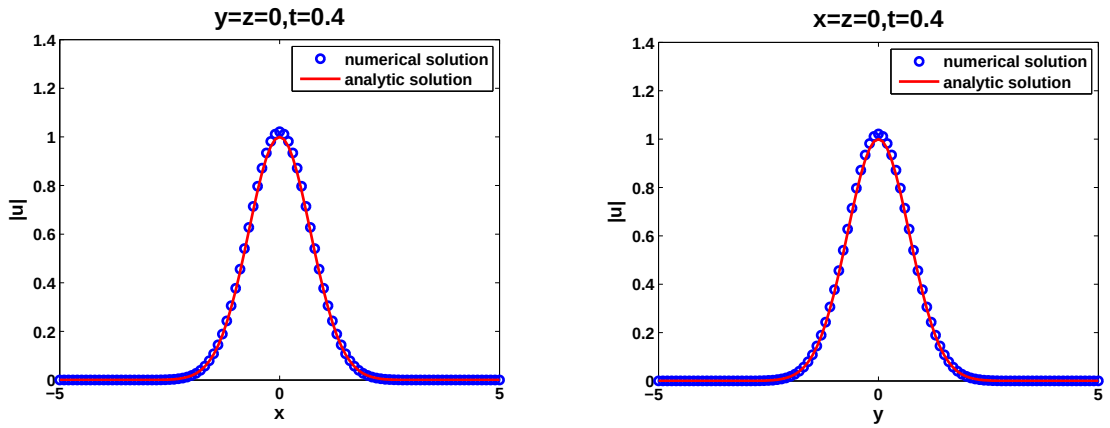

Figure 41: Comparison with analytic solutions to Eq. (122) with $\alpha_1 = \alpha_2 = \alpha_3 = 2$.

spatial variables are fixed in each figure. In [53], the solution generated by the Gross-Pitaevskii equation is compared to the real physical experimental data to illustrate how the equation models the soliton in the GRIN fiber.

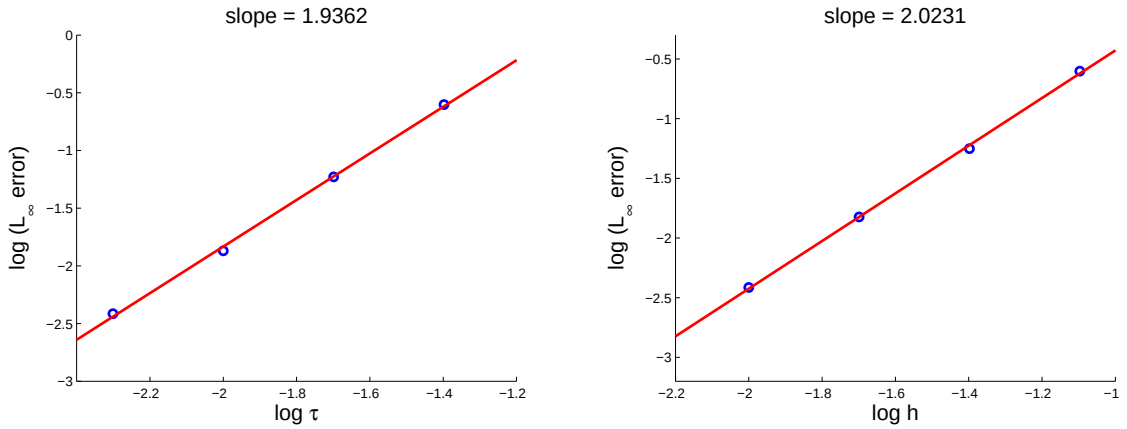

Figure 42: Order of convergence of solutions to Eq. (122) with $\alpha_1 = \alpha_2 = \alpha_3 = 2$.

From Fig. 42 we observe the order of convergence in time and in space using the second-order centered difference scheme (89) with the LE-EOS scheme (115). For convergence in time, we fix the spatial step as $h = 0.01$, and for convergence in space, we fix the time step as $\tau = 0.0001$. We notice from the log-log plot that the numerical

scheme is second-order in time and in space for solving the three-dimensional NLSE (122).

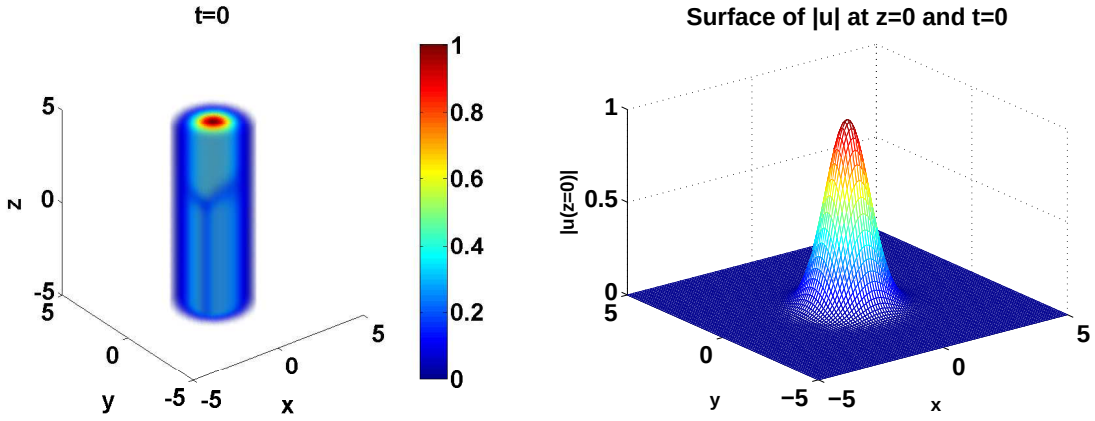

Figure 43: Initial condition of Eq. (122).

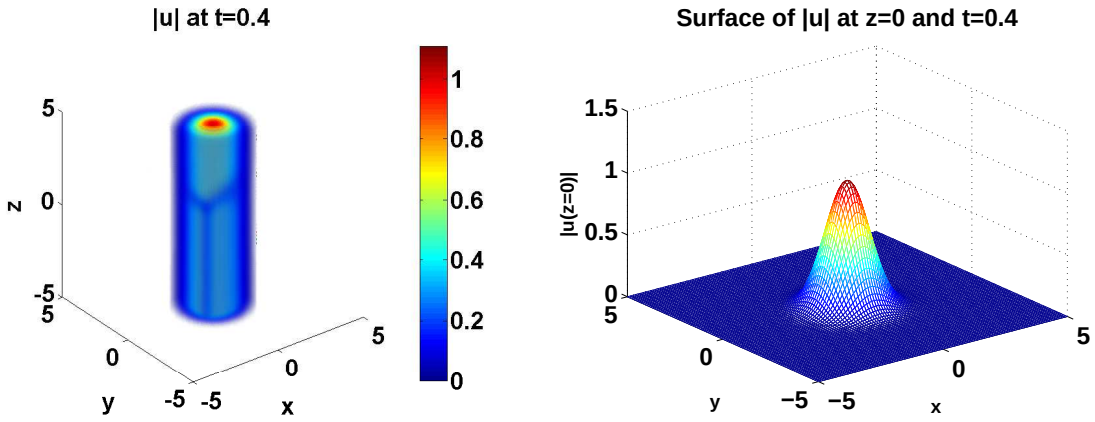

Figure 44: Solutions to Eq. (122) with $\alpha_1 = 1.2,\ \alpha_2 = 1.5,\ \alpha_3 = 1.8$.

The results shown in Figs. 43 and 44 model the propagation of a soliton in a GRIN fiber with a fractional refraction effect. It can be seen from the solution that the peak of the soliton moves slightly due to the fractional effect.

CHAPTER 6

CONCLUSIONS AND FUTURE WORK

We have developed and analyzed a central difference and quartic spline approximation based exponential time differencing Crank-Nicolson method, and a local discontinuous Galerkin approximation based time-stepping methods for solving systems of one-dimensional nonlinear Schrödinger equations and two-dimensional nonlinear Schrödinger equations. A fourth-order compact spatial approximation based fourth-order exponential time differencing Runge-Kutta scheme has been applied to solve the coupled fractional nonlinear Schrödinger equations. A locally extrapolated exponential operator splitting scheme is introduced for solving the multi-dimensional nonlinear fractional Schrödinger equations. The accuracy, efficiency, and stability of the numerical methods are investigated. It is evident from the analysis and numerical experiments that the numerical methods we adopt, compared to other numerical methods, are highly efficient and reliable.

Our continuing explorations include the development of highly accurate exponential time differencing schemes for nonlinear wave propagation simulations, numerical methods for time-space fractional partial differential equations, semi and full mesh adaptations, and priori, posterior error analysis of the underlying numerical methods.

REFERENCES

[1] G.P. Agrawal, Nonlinear Fiber Optics, 5th edition, Optics and Photonics (2013).

[2] X. Antoine, W. Bao, C. Besse, Computational methods for the dynamics of the nonlinear Schrödinger/Gross-Pitaevskii equations, Comput. Phys. Comm. 184 (2013) 2621-2633.

[3] M. Asadzadeh, D. Rostamy, F. Zabihi, Discontinuous Galerkin and multiscale variational schemes for a coupled damped nonlinear system of Schrödinger equations, Numer. Meth. Part. D. E. 29 (2013) 1912-1945.

[4] A. Atangana, A.H. Cloot, Stability and convergence of the space fractional variable-order Schrödinger equation, Adv. Differ. Equ. (2013) 1-10.

[5] W. Bao, D. Jaksch, P.A. Markowich, Numerical solution of the Gross-Pitaevskii equation for Bose-Einstein condensation, J. Comput. Phys. 187 (2003) 318-342.

[6] H. Bhatt, A.Q.M. Khaliq, The locally extrapolated exponential time differencing LOD scheme for multidimensional reaction-diffusion systems, J. Comput. Appl. Math. 285 (2015) 256-278.

[7] D.J. Benney, A.C. Newll, The propagation of nonlinear wave envelops, J. Math. Phys. 46 (1967) 133-139.

[8] H. Berland, A.L. Islas, C.M. Schober, Solving the nonlinear Schrödinger equation using exponential integrators, J. Comput. Phys. 255 (2007) 284-299.

[9] J.L. Bona, H. Chen, O. Karakashian, Y. Xing, Conservative discontinuous Galerkin methods for the Generalized Korteweg-de Vries equation, Math. Comput. 82 (2013) 1401-1432.

[10] P.G. Ciarlet, The Finite Element Method for Elliptic Problems, North-Holland, Amsterdam (1978).

[11] S.M. Cox, P.C. Matthews, Exponential time differencing for stiff systems, J. Comput. Phys. 176 (2002) 430-455.

[12] B. Cockburn, C.-W. Shu, TVB Runge-Kutta local projection discontinuous Galerkin finite element method for conservation laws II: general framework, Math. Comput. 52 (1989) 411-435.

[13] B. Cockburn, C.-W. Shu, The local discontinuous Galerkin method for time-dependent convection-diffusion systems, SIAM J. Numer. Anal. 35 (1998) 2440-2463.

[14] B. Cockburn, C.-W. Shu, The Runge-Kutta Discontinuous Galerkin Method for Conservation Laws, J. Comput. Phys. 141 (1998) 199-224.

[15] B. Cockburn, C.-W. Shu, Runge-Kutta discontinuous Galerkin methods for convection-dominated problems, J. Sci. Comput. 16 (2001) 173-261.

[16] C. Dai, Y. Wang, J. Zhang, Analytical spatiotemporal localizations for the generalized (3+1)-dimensional nonlinear Schrödinger equation, Opt. Lett. 35 (2010) 1437-1439.

[17] M. Dehghan, A. Taleei, Numerical solution of nonlinear Schrödinger equation by using time-space pseudo-spectral method, Numer. Meth. Part. D. E. 26 (2010) 979-992.

[18] H.F. Ding, C.P. Li, Y.Q. Chen, High-order algorithms for Riesz derivative and their applications (I), Abstr. Appl. Anal. (2014) Article ID 653797.

[19] Z.E.A. Fellah, C. Depollier, Application of fractional calculus to the sound waves propagation in rigid porous materials: Validation via ultrasonic measurement, Acta. Acustica. 88 (2002) 34-39.

[20] G.E. Forsythe, W.R. Wasow, Finite Difference Methods for Partial Differential Equations, Wiley, New York (1960).

[21] Z. Gao, S. Xie, Fourth-order alternating direction implicit compact finite difference schemes for two-dimensional Schrödinger equations, Appl. Numer. Math. 61 (2011) 593-614.

[22] R. Garrappa, M. Popolizio, Generalized exponential time differencing methods for fractional order problems, Comput. Math. Appl. 62 (2011) 876-890.

[23] B. Guo, Y. Han, J. Xin, Existence of the global smooth solution to the period boundary value problem of fractional nonlinear Schrödinger equation, Appl. Math. Comput. 204 (2008) 468-477.

[24] M. Hederi, A.L. Islas, K. Reger, C.M. Schober, Efficiency of exponential time differencing schemes for nonlinear Schrödinger equations, Math. Comput. Simulat. (2013) http://dx.doi.org/10.1016/j.matcom.2013.05.013.

[25] E.M. Hilal et al., Wavelet based spectral analysis of optical solitons, Optik, 125 (2014) 4589-4594.

[26] R. Hilfer, Applications of Fractional Calculus in Physics, World Scientific, Singapore (1999).

[27] M. Hochbruck, A. Ostermann, Exponential integrators, Acta. Numerica. (2010) 209-286.

[28] J. Hu, J. Xin, H. Lu, The global solution for a class of systems of fractional nonlinear Schrödinger equations with periodic boundary condition, Comput. Math. Appl. 62 (2011) 1510-1521.

[29] F.D. Hoz, F. Vadillo, An exponential time differencing method for the nonlinear Schrödinger equation, Comput. Phys. Commun. 179 (2008) 449-456.

[30] F.D. Hoz, F. Vadillo, Numerical simulations of time-dependent partial differential equations, J. Comput. Appl. Math. (2014) doi:10.1016/j.cam.2014.10.006.

[31] A.D. Ionescu, F. Pusateri, Nonlinear fractional Schrödinger equations in one dimension, arXiv:1209.4943 [math.AP].

[32] M.S. Ismail, S.Z. Alamri, Highly accurate finite difference method for coupled nonlinear Schrödinger equation, Intern. J. Computer Math. 81 (2004) 335-351.

[33] M.S. Ismail, T.R. Taha, A linearly implicit conservative scheme for the coupled nonlinear Schrödinger equation, Math. Computers Simula. 74 (2007) 302-311.

[34] M.S. Ismail, T.R. Taha, Parallel Methods and Higher Dimensional NLS Equations, Abst. Appl. Anal. (2013) http://dx.doi.org/10.1155/2013/497439.

[35] M.S. Ismail, T.R. Taha, Numerical simulation of coupled nonlinear Schrödinger equation, Math. Comput. Simulat. 56 (2001) 547-562.

[36] J. Jia, H. Wang, Fast finite difference methods for space-fractional diffusion equations with fractional derivative boundary conditions, J. Comput. Phys. 293 (2015) 359-369.

[37] A-K. Kassam, L.N. Trefethen, Fourth-order time-stepping for stiff PDEs, SIAM J. Sci. Comput. 26 (2005) 1214-1233.

[38] B. Kleefeld, A.Q.M. Khaliq, B.A. Wade, An ETD Crank-Nicolson method for reaction-diffusion systems, Numer. Meth. PDEs. 28 (2012) 1309-1335.

[39] A.Q.M. Khaliq, J. Martin-Vaquero, B.A. Wade, M. Yousuf, Smoothing schemes for reaction-diffusion systems with non-smooth data, J. Comput. Appl. Math. 223 (2009) 374-386.

[40] A.Q.M. Khaliq, D.A. Voss, K. Kazmi, Adaptive θ-methods for pricing American options, J. Comput. Appl. Math. 222 (2008) 210-227.

[41] L. Kong etc, Spectral-like resolution compact ADI finite difference method for the multi-dimensional Schrödinger equations, Math. Comput. Model. 55 (2012) 1798-1812.

[42] A.J. Laub, Matrix Analysis for Scientists and Engineers, SIAM, Philadelphia (2004).

[43] N. Laskin, Fractional Schrödinger equation, Phys. Rev. E. 66 (2002) 056108.

[44] J.D. Lawson, J.LI. Morris, The extrapolation of first order methods for parabolic partial differential equations, SIAM J. Numer. Anal. 15 (1978) 1212-1224.

[45] X. Liang, A.Q.M. Khaliq, Q. Sheng, Exponential time differencing Crank-Nicolson method with a quartic spline approximation for nonlinear Schrödinger equations, Appl. Math. Comp. 235 (2014) 235-252.

[46] X. Liang, A.Q.M. Khaliq, Y. Xing, Fourth Order Exponential Time Differencing Method with Local Discontinuous Galerkin Approximation for Coupled Nonlinear Schrödinger Equations, Commun. Comput. Phys. 17 (2015) 510-541.

[47] B. Lindberg, On smoothing and extrapolation for the trapezoidal rule, BIT Numer. Math. 11 (1971) 29-52.

[48] A.I. Mahdy, Interactions of two co-propagating laser beams in underdense plasmas using a generalized Peaceman-Rachford ADI form, Comp. Phys. Comm. 178 (2008) 249-271.

[49] R. Metzler, J. Klafter, The random walk's guide to anomalous diffusion: a fractional dynamics approach, Phys. Rep. 339 (2000) 1-77.

[50] M.D. Ortigueira, Riesz potential operators and inverses via fractional centred derivatives, Int. J. Math. Math. Sci. (2006) 1-12.

[51] L. Pitaevskii, S. Stringari, Bose-Einstein Condensation, Oxford University Press, Oxford (2003).

[52] I. Podlubny, A. Chechkin, T. Skovranek, Y. Chen, B.M.V. Jara, Matrix approach to discrete fractional calculus II: Partial fractional differential equations, J. Comput. Phys. 228 (2009) 3137-3153.

[53] W.H. Renninger, F.W. Wise, Optical solitons in graded-index multimode fiber, Nature Communications 4 (2013), Article number: 1719 doi:10.1038/ncomms2739.

[54] Q. Sheng, Global error estimates for exponential splitting, IMA J. Numer. Anal. 14 (1993) 27-56.

[55] J. Sun, M. Qin, Multi-symplectic methods for the coupled 1D nonlinear Schrödinger system, Comput. Phys. Commun. 155 (2003) 221-235.

[56] C. Sun, C. Barsi, J.W. Fleischer, Peakon profiles and collapse-bounce cycles in self-focusing spatial beams, Opt. Exp. 16 (2008).

[57] Q. Sheng, A.Q.M. Khaliq, E.A. Al-Said, Solving the generalized nonlinear Schrödinger equation via quartic spline approximation, J. Comput. Phys. 166 (2001) 400-417.

[58] Q. Sheng, A.Q.M. Khaliq, A revisit of the semi-adaptive method for singular degenerate reaction-diffusion equations, East Asia J. Appl. Math 2 (2012) 185-203.

[59] Q. Sheng, H.W. Sun, On the stability of an oscillation-free ADI method for highly oscillatory wave equations, Comm. Comput. Phys. 12 (2012) 1275-1292.

[60] P.L. Sulem, C. Sulem, A. Patera, Numerical simulation of singular solutions to the two-dimensional cubic Schrödinger equation, Pure Appl. Math. 37 (1984) 755-778.

[61] V.E. Tarasov, Fractional Dynamics: Application of Fractional Calculus to Dynamics of Particles, Fields and Media, Higher Education Press and Springer (2010).

[62] H. Wang, N. Du, Fast alternating-direction finite difference methods for three-dimensional space-fractional diffusion equations, J. Comput. Phys. 258 (2014) 305-318.

[63] D. Wang, A. Xiao, W. Yang, A linearly implicit conservative difference scheme for the space fractional coupled nonlinear Schrödinger equations, J. Comput. Phys. 272 (2014) 644-655.

[64] H. Wang, Numerical studies on the split-step finite difference method for nonlinear Schrödinger equations, Appl. Math. Comput. 170 (2005) 17-35.

[65] Wikipedia, https://en.wikipedia.org/wiki/Soliton_(optics).

[66] Y. Xu, C.-W. Shu, Local discontinuous Galerkin methods for nonlinear Schrödinger equations, J. Comput. Phys. 205 (2005) 72-97.

[67] Y. Xia, Y. Xu, C.-W. Shu, Efficient time discretization for local discontinuous Galerkin methods, Discret. Contin. Dyn. S. – Series B 8 (2007) 677-693.

[68] Q. Yang, F. Liu, I. Turner, Numerical methods for fractional partial differential equations with Riesz space fractional derivatives, Appl. Math. Model. 34 (2010) 200-218.

[69] J. Yang, Multisoliton perturbation theory for the Manakov equations and its applications to nonlinear optics, Phys. Rev. E. 59 (1999) 2393-2405.

[70] M. Yousuf, A.Q.M. Khaliq, B. Kleefeld, The numerical approximation of nonlinear Black-Scholes model for exotic path-dependent American options with transaction cost, Intern. J. Comput. Math. 89 (2012) 1239-1254.

[71] V.E. Zakharov, V.S. Synakh, The nature of self-focusing singularity, Sov. Phys. JETP. 41 (1975) 465-468.

[72] X. Zhao, Z. Sun, Z. Hao, A fourth-order compact ADI scheme for two-dimensional nonlinear space fractional Schrödinger equation, SIAM J. SCI. Comput. 36 (2014) A2865-A2886.